

Efficient Control of Series Elastic Actuators Through the Exploitation of Resonant Modes

by

Kevin B. Albert

Submitted to the Department of Mechanical Engineering
in partial fulfillment of the requirements for the degree of

Master of Science in Mechanical Engineering

at the

MASSACHUSETTS INSTITUTE OF TECHNOLOGY

June 2007

© Massachusetts Institute of Technology 2007. All rights reserved.

Author

Department of Mechanical Engineering
May 22, 2007

Certified by

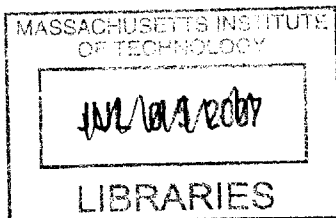
Hani Sallum
Member Technical Staff, Charles Stark Draper Laboratory
Thesis Supervisor

Certified by

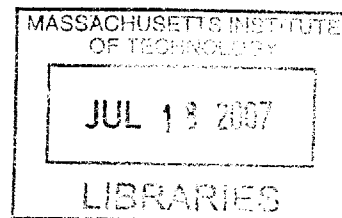
David Trumper
Professor, Mechanical Engineering
Thesis Reader

Accepted by

Lallit Anand
Chairman, Department Committee on Graduate Students



BARKER



Efficient Control of Series Elastic Actuators Through the Exploitation of Resonant Modes

by

Kevin B. Albert

Submitted to the Department of Mechanical Engineering
on May 22, 2007, in partial fulfillment of the
requirements for the degree of
Master of Science in Mechanical Engineering

Abstract

This thesis explores the efficiency potential inherent to series elastic actuators during oscillatory tasks. Series elastic actuators have a spring intentionally placed at the actuator output that provides good force resolution and filters out high frequency disturbances from the environment. These properties are essential for robotic applications in which interactions with the environment are unknown, because they allow the actuators to maintain stable force control while protecting the drive train from harmful loadings. The spring can also be used to store energy similar to the way animals use their tendons during locomotory tasks. This thesis shows that by operating the actuators at the appropriate frequency, the storage of energy by the springs can be translated into large efficiency gains for the actuator.

To show the efficiency gains of the actuator, a control scheme was developed that is capable of operating the actuators at and above their resonant frequency. The control scheme was based on spring force control allowing it to provide protection to the drive train while being robust to changes in link inertia due to manipulator configuration or environmental interactions. The control scheme was designed to be sufficient for use in real world applications so as to provide experimental results that are representative of operation on a robot vehicle.

The control scheme was implemented on a single-link benchtop teststand which was used to demonstrate the performance of the actuators. Experimental results are presented that demonstrate the conditions under which efficient actuation is possible. By comparing the experimental data to models of the hardware, the mechanisms through which power was lost were determined. The results indicate that at resonance there is the potential to achieve up to twice the efficiency obtained by a rigid actuator, however, in order to do so extra attention is needed in both hardware design and control.

Thesis Supervisor: Hani Sallum

Title: Member Technical Staff, Charles Stark Draper Laboratory

Thesis Reader: David Trumper

Title: Professor, Mechanical Engineering

[THIS PAGE INTENTIONALLY LEFT BLANK]

Acknowledgments

May 22, 2007

This thesis was prepared at The Charles Stark Draper Laboratory, Inc., under IR&D.

Publication of this thesis does not constitute approval by Draper of the findings or conclusions contained herein. It is published for the exchange and stimulation of ideas.

Kevin Albert

Acknowledgments

May 22, 2007

This thesis was prepared at The Charles Stark Draper Laboratory, Inc., under IR&D.

Publication of this thesis does not constitute approval by Draper of the findings or conclusions contained herein. It is published for the exchange and stimulation of ideas.

Kevin Albert

[THIS PAGE INTENTIONALLY LEFT BLANK]

Contents

1	Introduction	15
1.1	Motivation	15
1.1.1	Hardware	16
1.2	Thesis Highlights	17
1.2.1	Control	17
1.2.2	Efficiency	20
1.2.3	Power Loss	23
1.3	Thesis Outline	24
2	Background	26
2.1	System Causality, the Environment and Force Control	26
2.2	Series Elastic Actuators	28
2.3	Biological Locomotion	29
2.4	Series Elastic Actuators as Muscles	30
3	Experimental Hardware and Modeling	32
3.1	Hardware	32
3.1.1	Motor	32
3.1.2	Harmonic Geardrive and Belt	34
3.1.3	Compliance	34
3.1.4	Sensors	36
3.1.5	Electronics	38
3.1.6	Computer	41
3.2	Motor Commutation	42
3.2.1	Motor Electrical Model	42
3.2.2	Commutation Law	43
3.2.3	Implementation	45
3.3	Motor Model	48

- 3.4 Nonlinearity Compensation 49
 - 3.4.1 Cogging torque 50
 - 3.4.2 Stiction 51
- 3.5 System Model 54
 - 3.5.1 Series Elastic Actuator Model 54
 - 3.5.2 General Robotic Loading 56
 - 3.5.3 Frequency Response 58
- 4 Control 61**
 - 4.1 Motor Position Control 61
 - 4.2 Force Control 63
 - 4.2.1 Spring Compensation Law 63
 - 4.2.2 Closed Loop Force Control 65
 - 4.3 Load Position Control 69
 - 4.3.1 Shock Protection 71
 - 4.4 Control Issues 72
 - 4.4.1 Sensor Noise 72
 - 4.4.2 Vibration 74
 - 4.4.3 Stability 74
 - 4.5 Adaptive Feedforward Cancellation 76
 - 4.5.1 Resonator Tuning 78
 - 4.5.2 Force Limit Violation 81
 - 4.6 Controller Performance 81
- 5 Power Delivery and Efficiency 86**
 - 5.1 Open Loop 86
 - 5.1.1 Linear Model 86
 - 5.1.2 Hardware Response 90
 - 5.2 Controlled Response 101
 - 5.3 Non-Linear Loading 106
- 6 Conclusions 110**
 - 6.1 Suggestions for Improvement 111
 - 6.1.1 Sensors 111
 - 6.1.2 Mounting and Support 112
 - 6.2 Future Work 113
 - 6.2.1 Comparison to a Rigid Actuator 113

6.2.2	Control	113
6.2.3	Exploration of the Multi-Link Case	113
6.2.4	Application to a Robotic Vehicle	114

List of Figures

1-1	Time domain response showing the effect of nonlinear compensation.	18
1-2	Bode plot of the system under closed loop force control.	19
1-3	Plots demonstrating the improved tracking error achieved when the AFC loop is active.	19
1-4	Response to a Disturbance while not in resonant mode.	21
1-5	System Response to a sinusoidal load position command with the AFC loop closed.	21
1-6	Ideal efficiency response of the entire system.	22
1-7	Open loop efficiency response of the entire system	22
1-8	Closed loop efficiency response of the entire system.	23
3-1	Teststand Picture	33
3-2	Spring Shaft Pictures	35
3-3	Picture of the Harmonic Drive/Spring Shaft interface.	35
3-4	Pictures of the Ouput Encoder Placement	37
3-5	Ouput Encoder Magnetization Error	37
3-6	Integral Encoder Error	38
3-7	FFT of the encoder noise.	39
3-8	Encoder Differential Noise	39
3-9	Driver Circuit Schematic	40
3-10	Electronics Operational Block Diagram	41
3-11	Motor Electrical Model.	43
3-12	Current Loop Block Diagram	46
3-13	Current Loop Bode Plots	46
3-14	Phase A Commutation Current.	47
3-15	Commutation Current Delay	48
3-16	Motor Mechanical Model	49
3-17	Motor response plots without compensation.	49
3-18	Plot of the Cogging Torque	50
3-19	Plot of position error due to cogging torque.	51

3-20	Proportional control representation of the linearized LuGre Model	53
3-21	Plot of friction torque vs motor velocity	53
3-22	Plots of motor response with compensation	54
3-23	Series Elastic Actuator Model	55
3-24	Plot of Spring Stiffness	56
3-25	Frequency response of motor velocity from motor torque.	59
3-26	Frequency response of load velocity from motor torque.	59
3-27	Frequency response of spring torque from motor torque.	60
4-1	Motor Position Control	62
4-2	Bode plot of motor position rigid response	63
4-3	Frequency Response of Closed Loop Motor Position Control.	64
4-4	Bode Plot of closed loop force control	67
4-5	PID position control transient response.	68
4-6	FFT of PID position control command torque	68
4-7	Frequency Response from desired spring torque to load velocity.	69
4-8	Load Position Control	70
4-9	Frequency Response of Closed Loop load Position Control.	71
4-10	Load Position stability margins	72
4-11	Motor Chatter due to noise under load position control.	73
4-12	Motor Position Control stability with changing load inertia	75
4-13	Non-Dimensional Motor Saturation Characteristic	77
4-14	Load Position Control Tracking Error	77
4-15	Block Diagram of the AFC Loop.	78
4-16	Frequency Content of Load Position Tracking Error	79
4-17	Frequency Response of the AFC Resonators.	80
4-18	Tracking Error with the AFC Loop Closed	81
4-19	Open Loop Frequency Response of the AFC Loop	82
4-20	Closed Loop Frequency Response of the entire system	83
4-21	Step Response of the system under load position control	83
4-22	System Response to a sinusoidal load position command with the AFC loop closed.	84
4-23	Response to a Disturbance while not in resonant mode.	84
4-24	Response to a disturbance with the AFC loop closed.	85
5-1	Power flow diagram of the actuator and load.	87
5-2	Ideal Electrical Efficiency Response	88
5-3	Ideal Mechanical Efficiency Response.	89

5-4	Ideal Efficiency Response of the entire Series Elastic Actuator.	89
5-5	Representative Waveforms of the Electrical Input Power Calculation	92
5-6	Representative Waveforms of the Electrical Output Power Calculation	92
5-7	Representative Waveforms of the Mechanical Output Power	93
5-8	Picture of the damping mechanism used on the load.	93
5-9	Oscillation test waveforms	94
5-11	Open Loop Efficiency Response under low loading	96
5-12	Open Loop Efficiency Response under medium loading	97
5-13	Open Loop Efficiency Response under high loading	98
5-14	Controlled Efficiency Response under low loading	103
5-15	Controlled Efficiency Response under medium loading	104
5-16	Controlled Efficiency Response under high loading	105
5-17	Controlled Efficiency Response under Nonlinear Loading with $\tau_{f,E} = 46mNm$	107
5-18	Controlled Efficiency Response under Nonlinear Loading with $\tau_{f,E} = 85mNm$	108
5-19	Controlled Efficiency Response under Nonlinear Loading with $\tau_{f,E} = 125mNm$	109

List of Tables

- 3.1 Motor Parameters 34
- 3.2 Current Loop Parameters 47
- 3.3 Stiction Parameters 52
- 3.4 Series Elastic Actuator Parameters 55

- 4.1 Motor Position Controller Parameters 63
- 4.2 Load Position Controller Parameters 70

- 5.1 Open Loop Efficiency Values. 95
- 5.2 Controlled Efficiency Values. 102
- 5.3 Estimated controlled efficiency vales. 106

Chapter 1

Introduction

In robotics applications where unknown interactions with the environment take place, the use of series elastic actuators is advantageous because they provide good force control while exhibiting shock protection to high frequency disturbances. Akin to animal muscles, series elastic actuators have an elastic element placed between their power source and their output. In addition to using the elasticity of their muscles for force control and shock tolerance, animals exploit it to gain efficiency during locomotory gaits. In this thesis, the potential for exploiting series elastic actuators to gain efficiency is explored. Through model and experiment the conditions under which efficiency can be gained are determined and the mechanisms through which power is lost and system performance is limited are identified.

1.1 Motivation

Historically rigid actuators have been used in the design of manipulators in order to take advantage of their superior position control capabilities. Compliance in these systems is minimized, yielding lower order systems that respond well to high controller gains. Unfortunately, in certain applications a manipulator's environment is rigid and explicitly controls position as well. In these cases rigid actuators are incompatible with their environment and interactions result in high contact forces and often damage to either the environment or the robot. In light of this, it has been widely argued that in order to interact safely with the environment, robot manipulators must be capable of controlling the forces of interaction instead of blindly defining position [Hogan, 1985a,b,c], [Kazerooni et al., 1986], [Raibert and Craig, 1981]. This train of thought is referred to as force control. Unfortunately, rigid actuators are constrained by the bandwidth of their controller and are susceptible to high frequency disturbances. Also, poor force resolution is inherent to rigid actuators, and causes instability during force control.

The shortcomings exhibited by rigid actuators were remedied by the conception of series elastic

actuators where an elastic element is intentionally placed between the actuator and its load [Pratt and Williamson, 1995]. The elastic element filters out high frequency disturbances while adding force resolution to the system. This provides an actuator that is shock tolerant and has the capability to provide stable force control.

Series elastic actuators are the robotic dual of animal muscles/tendons. The elastic properties of animal muscles/tendons are essential for controlling force during movement as well as protecting the animal from harmful shockloads. Animals have also learned to exploit the elasticity of their muscles/tendons to gain efficiency during locomotory gaits by storing energy in their muscles/tendons during one phase of their stride in order to release it at a more advantageous point. In this thesis it is shown that series elastic actuators, like animal muscles, can be exploited to gain efficiency during oscillatory tasks.

1.1.1 Hardware

The motivation behind this project comes from the HISS project at Charles Stark Draper Laboratory. The HISS vehicle is a Hyper-Redundant Intelligent Sensing Snake that was built with the goal of being able to autonomously navigate unknown environments. HISS was constructed using redundant two degree of freedom modules connected in series. Each DOF included an actuator that consisted of a motor, harmonic gear drive and output shaft. The motor drove the harmonic gear drive which in turn drove the output shaft. The output shaft interfaced the actuator with its load, which in the case of HISS was by connecting the present module to the next module through a link.

When HISS was run with rigid output shafts, it exemplified all of the shortcomings that provide the motivation behind series elastic actuators. All of the gearboxes on the vehicle were constantly stressed which caused them to jump teeth and ultimately led to deterioration in their performance. In a short period of time all of the gearboxes were destroyed and needed replacement.

Replacing the solid shafts with spring shafts alleviated a large portion of the stresses endured by the gearboxes, however, due to the truncated time table of the project force control was never achieved. Other hardware issues including sensing, motor commutation and nonlinearities never allowed for a stable force control scheme to be implemented and ultimately the system had to be run with a low bandwidth position controller.

Although force control was never achieved initial results from the system indicated that the addition of the spring provided efficiency gains under certain operating conditions. During largely oscillatory gaits such as sidewinding, the HISS vehicle demonstrated large efficiency gains in modules closer to the center of the snake. Due to their location, these modules had higher inertial loads than the outer modules. This effectively lowered the resonant frequency of the actuator/load bringing it closer to the operating frequency of the snake. Unfortunately, due to some of the hardware issues the data obtained from the HISS vehicle is not reliable thus creating the need for the work done

here.

The work in this thesis uses pieces from the HISS project in order to illustrate the performance capabilities of series elastic actuators. Extensive time is spent dealing with the issues encountered during the HISS project in order to understand and effectively implement the series elastic actuators. Additions or alterations to the hardware were made and control was developed so that the performance of the actuators could be documented. After the hardware issues and controls were addressed the HISS hardware was used to show that series elastic actuators yield significant gains in efficiency when operated under the appropriate conditions.

1.2 Thesis Highlights

There were two major goals that were set out for the work in this thesis:

- Develop a control scheme that takes advantage of the force control properties of the actuators to protect the hardware, while being able to operate with significant bandwidth to illustrate efficient actuation.
- Using experimental data, show that efficiency gains can be achieved and demonstrate the conditions under which efficient operation is feasible.

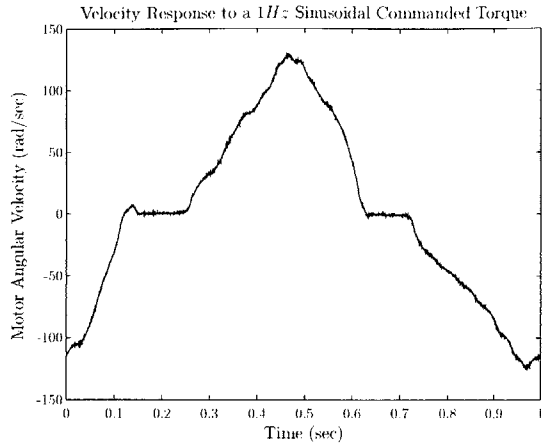
This section gives details on each of these goals and shows the important results achieved by this thesis.

1.2.1 Control

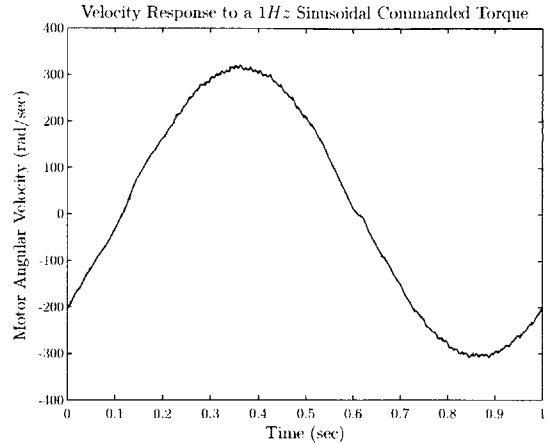
In order to show that series elastic actuators can be exploited to gain efficiency in real systems, it is essential that tests are performed under realistic conditions. In light of this, the control system developed to run the actuators was subject to the requirements of a real vehicle. This meant that the control system must maintain accurate force control to protect the actuator under adverse loading conditions. It must be robust to changes in load inertia that may be present on a real vehicle due to changes in the vehicle's configuration. And of course, it must be able to operate with high enough bandwidth to investigate the performance of the actuators. Some of the important issues that were encountered in the development of the control scheme are given here, as well as some experimental results demonstrating the controller performance.

Nonlinear Compensation

For the most part, linear control techniques were used in the control scheme that was developed. In order to make this possible, however, feedforward terms were used to compensate for nonlinear effects such as cogging torque and stiction. These feedforward terms were essential to linearizing



(a) Time domain response of the motor without nonlinearity compensation.



(b) Time domain response of the motor with nonlinearity compensation.

Figure 1-1: Time domain response showing the effect of nonlinear compensation. The plots are the velocity response of the motor/gearbox to a $1Hz$ sinusoidal commanded current. (a) This plot shows that without compensation the response is nonlinear due to phenomenon such as stiction and cogging torque. (b) This plot shows that when the feedforward terms are added to the commanded current the system behaves linearly.

the system so standard control techniques could be used. A plot of the motor velocity response to a $1Hz$ sinusoid is given in Figure 1-1, it shows the effectiveness of the compensation scheme.

Force Control

A motor position loop is used as the foundation for force control. It is found that the motor position loop provides the high frequency bandwidth limitation on force control while load motion and sensor delay provide limitations at low frequencies. A Bode plot of the system under closed loop force control is given in Figure 1-2. The low frequency force control limitations are acceptable because they are the result of load movement, which is ultimately the purpose of force control when the load is unconstrained.

Adaptive Feedforward Cancellation

A PID controller was used to determine the force in the spring required for load movements. Due to control issues including sensor noise and inadequate load plate mounting, however, the load position loop yielded significant errors at the efficient frequencies. Adaptive Feedforward Cancellation (AFC) was used to compensate for the shortcomings in the load position loop. Figure 1-3 shows the resulting load position error signal when operated with and without AFC at a frequency of $16.9rad/s$. It shows that when AFC is activated good load position tracking is achieved.

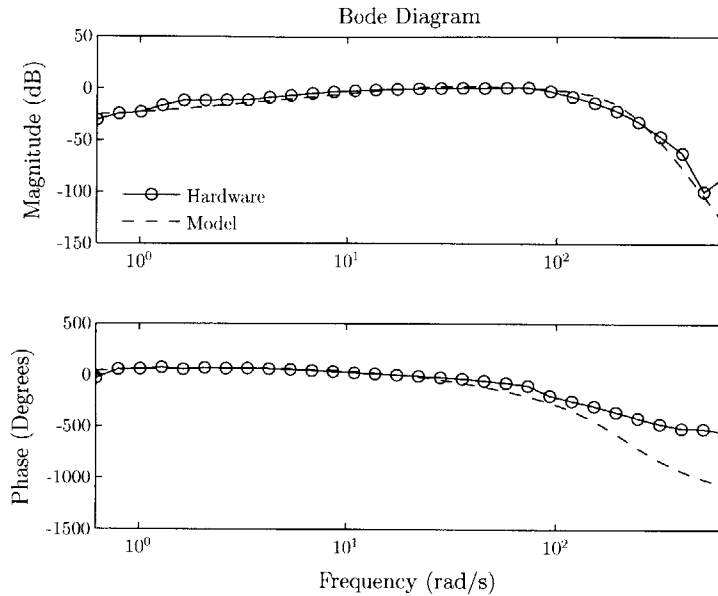
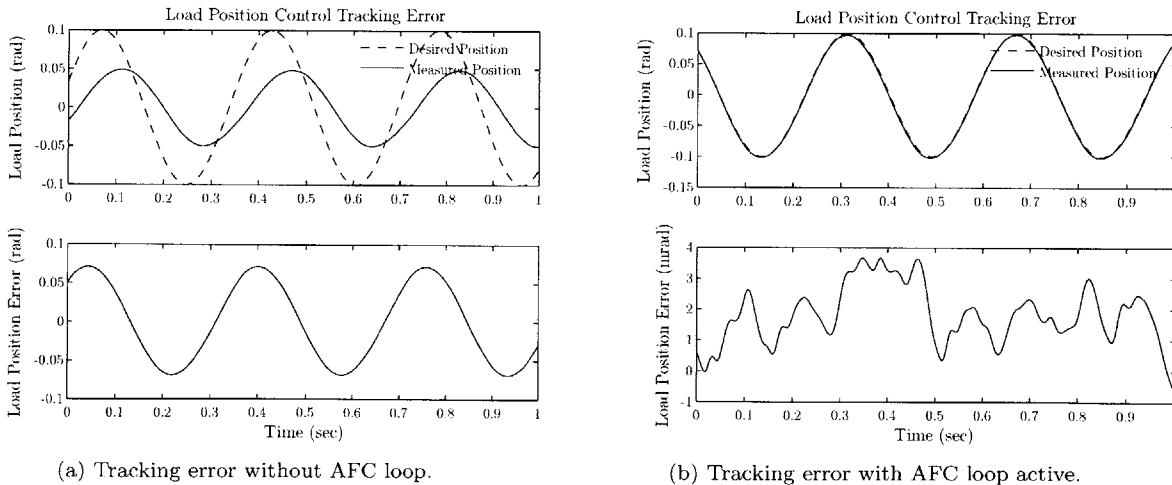


Figure 1-2: Bode plot of the system under closed loop force control. This plot gives the response from desired spring torque to measured spring torque.



(a) Tracking error without AFC loop.

(b) Tracking error with AFC loop active.

Figure 1-3: These plots demonstrate the superior tracking error achieved by the AFC loop. (a) This plot shows the tracking error under load position control when the AFC loop is not active. The tracking error is very large due to the limited bandwidth of the control loop. (b) This plot shows the tracking error under load position control with the AFC loop active. The tracking error has been reduced to less than 10% of the original error.

Stability

System stability is largely affected by the size of the load inertia. Decreases in the load inertia cause the force control loop to go unstable. In general, this is because a decrease in load inertia equates to an increase in the resonant frequency of the system. As the system resonance approaches the limitations of the motor position loop stability can no longer be maintained. It was found that for the current hardware, the major limitations of the motor position loop were due to controller bandwidth and motor current saturation.

Controller Performance

The controller performance is illustrated here through two representative experiments. Figure 1-4 shows the response of the system to a large load disturbance while commanded to hold a position. This plot shows how the control scheme protects the system during adverse loading and that the load position control responds nicely to correct the error once that loading has subsided. Figure 1-5 shows the response of the system to a nonlinear load suddenly placed on the system during resonant control. Good tracking is achieved at the system's resonant frequency. When the nonlinear load is placed on the system, the control system suppresses the error and achieves good tracking with the nonlinear load. These plots show that the control system goals have been achieved in that the system is protected against harmful disturbances, is robust to changes in inertia and can operate effectively at the resonant frequency of the system.

1.2.2 Efficiency

Through model and experiment, it is demonstrated that series elastic actuators can provide significant efficiency gains when operated at the appropriate frequency. The efficiency gain is due to the resonance between the load inertia and the elastic element in the actuator. At the resonant frequency, very little movement is needed at the spring input (i.e. the motor) to produce large movements on the output. This lowers the input power required by the actuator to produce the same output power, therefore efficiency is gained. The amount of efficiency that can be gained is directly related to the load damping. Low damping values, where the resonant peak is large, yield large efficiency gains if the actuators are operated at the resonant frequency. High damping values, yield lower gains in efficiency but result in better overall system efficiency. The results indicate that given the choice it is desirable to operate the actuators at higher damping values as is done in impedance matching. However, when lightly damped movements are required, such as a human running gait where the direction of movement is parallel with the environmental interface, the experimental results show it is advantageous to operate at resonance.

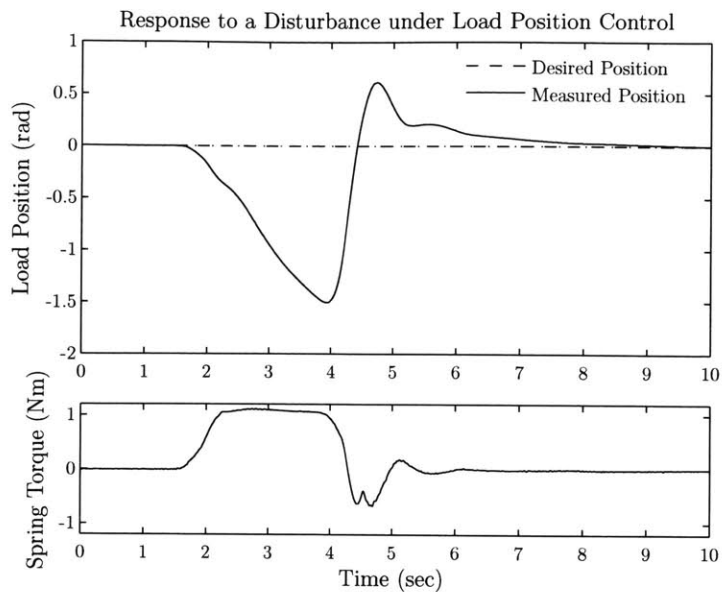


Figure 1-4: Response of the system to a disturbance while not in resonant mode. Initially the load is being held at the desired load position of zero radians. At 1.5 seconds the load plate is pulled by hand to demonstrate the system's response to extreme disturbances. When the spring torque reaches 1Nm the load position control command saturates and the force control loop attempts to hold the spring torque at 1Nm. The load is then release at 4 seconds and once the load position controller asks for a spring torque below the 1Nm limit the load position loop resumes control.

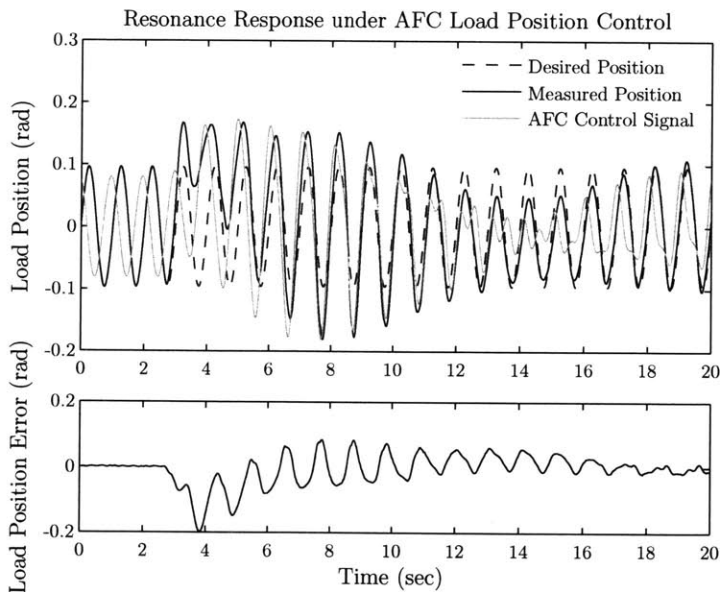


Figure 1-5: System response to a sinusoidal load position command with the AFC loop closed. Initially the system is operating at steady state with the control loop active resulting in negligible position error. At 2.7 seconds the nonlinear loading is added (a bucket with intermittent ground contacts) and the AFC loop reacts and suppresses the disturbance.

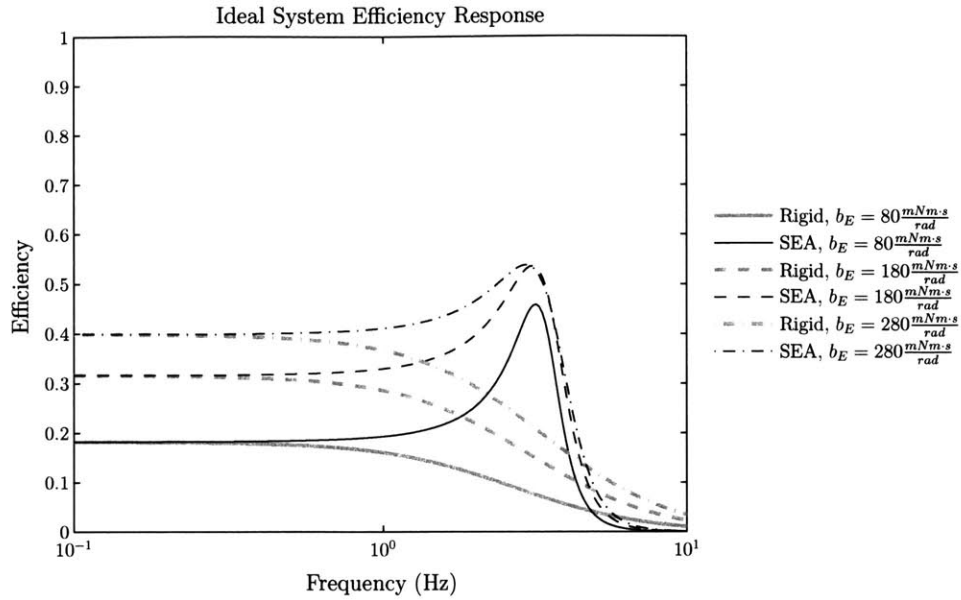


Figure 1-6: Ideal Efficiency Response of the entire system. An efficiency peak occurs between the load resonance frequency and the system resonance frequency indicating that efficiency can be scavenged by series elastic actuators if operated at the optimal frequency

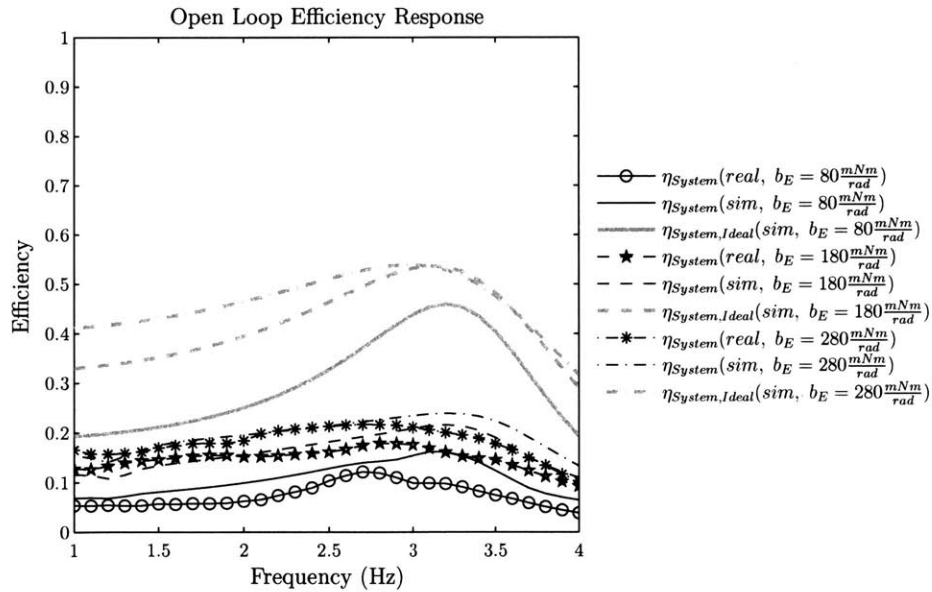


Figure 1-7: Open loop efficiency response of the entire system. The plot shows that there is a large decrease in efficiency from the ideal system to the actual system. This drop in efficiency is largely due to motor/gearbox stiction that is not part of the ideal model. Despite the decrease in overall system efficiency, however, the system still has an efficiency peak.

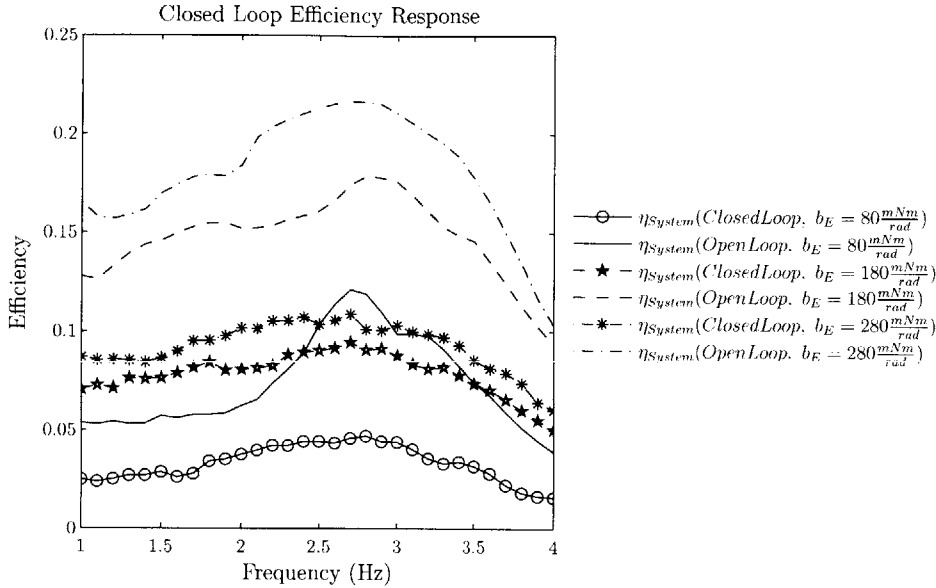


Figure 1-8: Closed loop efficiency response of the entire system. The plot shows that there is a large drop in efficiency from the open loop response to the controlled response. One of the drawbacks of series elastic actuators is that, due to the compliance, large motor movements are required to maintain force control which draws extra power. In the current system, these movements are amplified by false sensor readings and mechanical vibrations causing an excessive drop in efficiency when the system is under control.

1.2.3 Power Loss

The series elastic actuators used in this thesis suffered primarily from two major forms of power loss; stiction losses and losses due to control. Figure 1-6 gives the ideal efficiency of the system at three different values of load damping and compares it with the ideal rigid actuator efficiency. Figure 1-7 gives the experimental results of the open loop system efficiency compared to the ideal model and a non-ideal model that includes stiction. Figure 1-8 shows the experimental results of the system with the control system active. The results show that a large drop in efficiency is experienced with each iteration of testing.

Stiction Losses

Figure 1-7 shows a large drop in efficiency from the levels predicted by the ideal model. This drop in efficiency is primarily due to the presence of stiction in the real system. Stiction affects the system in two ways. Motor stiction creates a mechanical power loss in phase with the motor velocity. In order to compensate for the motor stiction, extra current is drawn creating higher resistive losses in the motor electronics. The resistive losses make up the larger portion of stiction losses due to the fact that they are proportional to the square of the motor current while the mechanical losses are proportional to just the motor current.

Control Losses

Figure 1-8 shows that there is a significant drop in efficiency from the open loop system to the closed loop system. This drop in efficiency is primarily due to the extra power necessary to control the system. The benefits of series elastic actuators are that the addition of compliance in the system filters out high frequency disturbance and increases force resolution. This is possible because more compliant systems require larger deflections to produce large forces. From a control standpoint, however, this translates to larger motor movements to correct for force control errors. Even small force errors can cause large movements of the motor and require large power draws. Although some force errors are due to disturbances or load movements in which case the power draw due to control is reasonable, force errors can also be due to measurement errors in which case power draw due to control is excessive.

System Design

In most cases the power lost in the system is due to inadequacies in design. In any real system there will always be power lost due to electrical resistance, friction and sensor error. The magnitude of these inadequacies, however, plays a large roll in the overall system efficiency. Although running series elastic actuators at their resonant frequency does allow the system to gain efficiency, the first step in any design concerning efficient operation must be to address non-idealities such as stiction, sensor noise, vibrations and system mounting among others. Only then can series elastic actuators be exploited to their full potential.

1.3 Thesis Outline

Chapter 2 presents the background work, explaining the reasoning behind force control, the motivation for and benefits of using series elastic actuators, as well as a short survey of applicable work done on biological locomotion and a summary of related work.

Chapter 3 gives a detailed description of the hardware, documents the work done on motor commutation and nonlinearity compensation to linearize the system, and develops a linear model of the hardware.

Chapter 4 describes the control scheme developed to run the series elastic actuators and demonstrates the capabilities of the control system through a few representative experiments.

Chapter 5 shows the experimental results and explains the efficient capabilities of the system as well as the major sources of power loss that limit system efficiency.

Chapter 6 reviews the work done in this thesis and draws conclusions on the results obtained. Also suggestions for improvement and possible topics for future research are given here.

Chapter 2

Background

2.1 System Causality, the Environment and Force Control

Most robotic systems that have been able to effectively make the jump from laboratory study to uses in real world applications have been rigid systems, where compliance has been minimized in both the actuators and the robot's structure. Rigid systems are desirable in many applications because they are for the most part superior at trajectory control. Undesired vibrations that may cause errors are isolated to high frequencies in stiff systems allowing high controller bandwidth and in turn excellent position tracking. Using the structure of the system to minimize the vibrations as opposed to using the controller also decreases the energy demand resulting in a more efficient system. Systems, however, that are successful in this respect are subject to the restriction that they are conceived with the full knowledge of both their task and their environment.

In practice, most position controlled robots are designed to interact mainly with their task because they deliver energy in a way that is incompatible with most environments [Robinson, 2000]. The interaction between two systems can be described by the dynamics of the power transfer at their interface. Each system in a workspace is defined by a control surface through which power can be transferred to other systems via shared ports (i.e. a motor shaft). The power entering a system and therefore leaving another system (or vice versa) at a specific port is defined as the product of the two conjugate variables effort and flow, where effort is the symmetric variable and flow is the anti-symmetric variable when viewed from different sides of the interface [Brown, 2001]. Incidentally, due to the causal nature of real systems, only one of the variables can be defined by a given system. The other variable is then left as a dependent variable to be defined by the connected system. In the case of a DC motor (System 1) connected by a shaft to some load (System 2), the motor can only define the effort (i.e. shaft torque). The flow (i.e. shaft angular velocity) is then determined by the load's response to the input torque. A rigid robot is a system explicitly designed to control motion

or flow by overcoming the torque or effort reflected back by its load or task. This means for rigid actuation to be suitable, the task must be able to accept flow, or in other words the task must be an impedance as defined by Hogan. Most environments, however, are admittances not impedances. They are kinematically constrained inertial objects that define flow and accept only effort [Hogan, 1985a]. Therefore for a robot to effectively interact with its environment it must control effort, this is defined in the literature as “force control.”

To address the problem of dealing with a constrained environment a number of force control strategies have been developed. These methods generally follow one of two trains of thought. One is that force is explicitly controlled along degrees of freedom that are constrained by the environment while simultaneously position is controlled in directions orthogonal to the system/environment interface. This line of thought is called hybrid control which was developed by [Raibert and Craig, 1981] based on the work done by [Mason, 1981]. The second train of thought follows the premise that the robot should control position in all directions while accommodating disturbances instead of merely rejecting them. In this scheme the environment is accommodated by choosing the appropriate output dynamics the robot is to exhibit to ensure energetic compatibility at the interface. This line of thought has been presented in a number of forms including; Stiffness Control [Salisbury, 1980], Impedance Control [Hogan, 1985a,b,c], Compliance Control [Kazerooni et al., 1986] and Parallel Force/Position Control [Chiaverini and Sciavicco, 1993].

These control techniques on their own, however, only solve the force control problem at frequencies within the controller’s bandwidth. Unfortunately, irregularities in the environment and force sensor noise ensure that high frequency disturbances exist. These disturbances, in turn, can cause large contact forces or even instability when a robot is in contact with the environment [An and Hollerbach, 1987]. A solution to this problem was the application of passive compliance at the interface that acts as a low pass filter for disturbances and adds resolution to the force sensing [Roberts et al., 1984, Hirai et al., 1998]. This strategy is successful when only the tip of a robot interfaces with the environment, however, it is insufficient if the entire robot may have to. Adding compliance to the joints gives the overall system a compliant dynamics that is desirable but causes instability due to the non-collocated modes created. In order to stabilize the system damping can be added to the joint compliance to suppress the collocated modes [Eppinger and Seering, 1992] or force sensing can be added to the joints to control them. Adding damping slows the response of the system which is undesirable, whereas, adding joint force sensing makes design and control more complicated but produces an effective result. This solution is the foundation on which Series Elastic Actuators were developed.

2.2 Series Elastic Actuators

Over the past two decades a new class of robotics has arisen where environmental interactions and in some cases specific tasks are unknown upon the robot's conception and so the robot must be designed to deal with these disturbances. Types of robots in this class include teaching and skill acquisition, telerobotics, haptics and biomimetic robots [Robinson, 2000]. Due to the uncertainty of their interactions these robots need compliant actuators to implement stable force control. In addition, the size of motor that is necessary to drive these systems has low power density at low speeds and therefore must be geared to operate in an efficient range. The motor inertia seen by the environment reflected through the $N : 1$ gear ratio is scaled by N^2 requiring high forces to backdrive the motor. These forces put large stresses on the gear teeth and will often damage the transmission, thus the actuator must be able to exhibit good shock protection as well. Series Elastic Actuators accomplish this by intentionally placing a spring after the transmission and sensing the force in the spring to ensure stable control of the actuator [Pratt and Williamson, 1995].

The use of series elastic actuators, however, does not come without its drawbacks. By placing a compliant element in the joint the overall gain of the system is lowered which leads to "looser" control when operating in high admittance environments. Also due to the spring's interaction with arm or link inertias the resonant modes of the system are lowered limiting control bandwidth. Thus the use of series elastic actuators presents a number of engineering tradeoffs that must be addressed during the robot design. An in depth study of these tradeoffs and how to address them is provided by [Robinson, 2000]. In general, bandwidth and system gain are traded for dynamic range and low output impedance.

The benefits attained by the use of series elastic actuators are directly related to the stiffness of the elastic element in the actuator. The source of these benefits will be briefly discussed while a more in depth exploration will be left to the literature. Dynamic range is the ratio of the maximum force to the minimum difference in force or force resolution that can be delivered by the actuator. The maximum force does not change due to the addition of the compliance; at frequencies below resonance it is still directly related to the maximum force produced by a standard rigid actuator (i.e. the motor). The force measurement, which defines the attainable force resolution, is proportional to the differential position across the elastic element. If the elasticity is increased, a wider positional range is achieved, thus the resolution is improved. Consequently, the dynamic range of the actuator is increased which improves force control. The output stiffness, as seen from the environment, is the ratio of the output force to the difference in output position required to produce that force. Under perfect force control the output stiffness would be zero and movements of the output would not change the force from its controlled value. In real systems the output stiffness is related to the tightness of the force control loop and it increases with frequency until the bandwidth of the controller is reached where the output stiffness equals the stiffness of the physical system. For a series

elastic actuator the high frequency output stiffness is equal to the stiffness of the elastic element, therefore, the softer the spring the better the shock protection from high frequency disturbances. When using series elastic actuators the designer must decide on the stiffness of the elastic element by weighing the tradeoffs discussed above.

Series elastic actuators have been successfully implemented in a number of robots. At the MIT Leg Lab, where the actuators were conceived, they were used in “spring turkey” and “spring flamingo” two planar biped robots, in “M2” and “Troody” two autonomous bipedal robots and in the arms of “COG” a humanoid robot among others [LegLab, Pratt, 2000]. Outside of the Leg Lab series elastic actuators were used in LOPES, an exoskeleton-type rehab robot [Veneman et al., 2006], “Big Dog” an autonomous quadruped robot [BDI], an unnamed power autonomous monopedal robot [Krupp and Pratt, 2006] and HISS, a Hyper-Redundant Intelligent Sensing Snake among others.

2.3 Biological Locomotion

The conception of series elastic actuators was largely aided by insights obtained from the study of biological locomotion. A great deal of research has been done on the movement of multi-legged animals both for the purpose of better understanding ourselves and to try to imitate them to develop more mobile and functional robotics. It has been found that the gaits that animals use are highly efficient and versatile for their terrain. [Cavagna et al., 1976, 1977] showed that bipeds such as humans and birds and quadrupeds such as dogs, monkeys and rams moved in highly efficient ways by using an exchange between potential and kinetic energy to minimize wasted work during motion. He showed that during slower gaits, such as walking, animals exchange the kinetic energy associated with the forward motion of their center of mass with potential energy due to gravity. When efficiency was maximized in a walking gait the magnitude of these two quantities were 180 degrees out of phase. For faster gaits such as running, however, the fluctuation in potential energy due to gravity is much smaller and the two quantities became more in phase without a significant drop in efficiency. Cavagna suggested that at higher speeds the exchange of potential and kinetic energy is maintained through another mechanism identified as the storage of potential energy by the elastic nature of muscles and tendons.

Later studies showed that Cavagna’s hypothesis was correct and that animals do store energy in elastic muscles and tendons during locomotion. [Alexander, 1984] surveyed experimental work on tendon, bone and muscle elasticity and showed through the analysis of film and force records that animals store elastic energy primarily in their tendons. Work was also done to create a simple model of an animal’s leg that could accurately represent the gait motions observed during locomotion [Blickhan, 1989, McMahon and Cheng, 1990]. These models were used to understand the properties that define an individual gait and it was shown that the model is sufficiently generic to be used to

describe many forms of locomotion across a large number of skeletal configurations [Blickhan and Full, 1993]. This model has become known as the spring loaded inverted pendulum (SLIP) model for terrestrial locomotion.

2.4 Series Elastic Actuators as Muscles

According to the models of biological locomotion the musculatory system can be represented as an array of spring-actuator combinations that are used to regulate body movement. In animals the elastic component of the muscle-tendon combination is used for shock protection and force application as well as energy conservation during appropriate tasks. In order to gain efficiency through energy storage, the task must be oscillatory in nature suggesting that the efficiency is a result of a resonance between two energy storing elements. In the robotic world, series elastic actuators are then the dual of biological muscles. They were originally created for their shock tolerance and force control properties but like biological actuators they too could be exploited for efficiency.

A few researchers have done work on trying to exploit the natural dynamics of series elastic actuators for oscillatory robotic tasks but the work done is limited and the results seem to be hindered by progress in control. Still there are a few noteworthy works that have surfaced. Williamson showed that neural oscillators could be used to control series elastic actuators, and that due to the adaptive nature of the oscillators only the mechanical coupling between multiple degrees of freedom were needed to produce coordinated behavior. This produced a simple yet robust control paradigm [Williamson, 1999]. Unfortunately, no correlation between the natural motion produced and the system efficiency was made. Buchli et al. are studying adaptive oscillators along the same line of thought. They show that when feedback is provided, the oscillators converge to the most efficient operating point [Buchli et al., 2005]. At this point their efficiency results are shown only in simulation, as experimental hardware results are yet to be reported. Hollander et al. have designed a human ankle walking assistance device that utilizes a series elastic actuator controlled by a human's walking gait that they call a robotic tendon. The work shows that using a series elastic device results in less energy consumption than a direct drive actuator [Hollander et al., 2006]. Paluska and Herr show that more energy can be output per stroke by using series elastic actuators instead of a direct-drive motor and that an instantaneous power amplification can be gained by tuning the spring stiffness to the load [Paluska and Herr, 2006]. Along a similar line of thought Scarfogliero et al. have designed the jumping robot "Grillo" to use a low power motor in a series elastic configuration to build up energy in the springs during its aerial phase. By releasing the energy in the springs upon landing the robot produces much higher power delivery than its motors are capable of alone [Scarfogliero et al., 2006]. The humanoid robot "Lucy" developed by Vanderborght et al. uses

pneumatic actuators similar to series elastic, called McKibben Muscles. They show on a one link test stand that energy consumption is reduced when the link is actuated at an optimal frequency [Vanderborght et al., 2006].

This thesis investigates the idea that the elastic element inherent to series elastic actuators can be exploited for efficiency if the system is operated at the optimal frequency. The subsequent chapters aim to add to the pool of work given here, by demonstrating through model and experiment, that at resonance, energy is stored in the elastic element of the actuator increasing efficiency.

Chapter 3

Experimental Hardware and Modeling

In this chapter the physical hardware used for the work in this thesis is described and a system model is developed. Section 3.1 describes the individual components that make up the system including the motor, gearing, compliance, sensors, electronics and computer as well as discusses some of the improvements made on the HISS hardware. Section 3.2 presents a model of the motor electronics and derives the commutation law used to run it. Section 3.3 gives the mechanical motor model and investigates nonlinearities in the model. Section 3.4 describes the compensation scheme used to counteract the motor's nonlinearities and linearize the model. Section 3.5 discusses the loading conditions that will be used, derives a linear model of the entire system and compares it with experimental data.

3.1 Hardware

A large portion of the mechanical hardware is made up of components from the HISS project at Charles Stark Draper Laboratory. These parts include the motor, gearing, series compliance and encoders. Aside from the encoders, no physical alterations were made to these pieces as part of the work related to this thesis. The remaining parts were created or programmed specifically for this thesis. The work in this thesis is done on a single link benchtop setup that replicates the hardware configuration on the HISS vehicle. The benchtop setup is shown in Figure 3-1.

3.1.1 Motor

The motor used on the experimental setup is a Torcman TM200-5-18 three phase brushless DC motor. The motor is an external rotor design with twelve permanent magnets on the rotor and nine

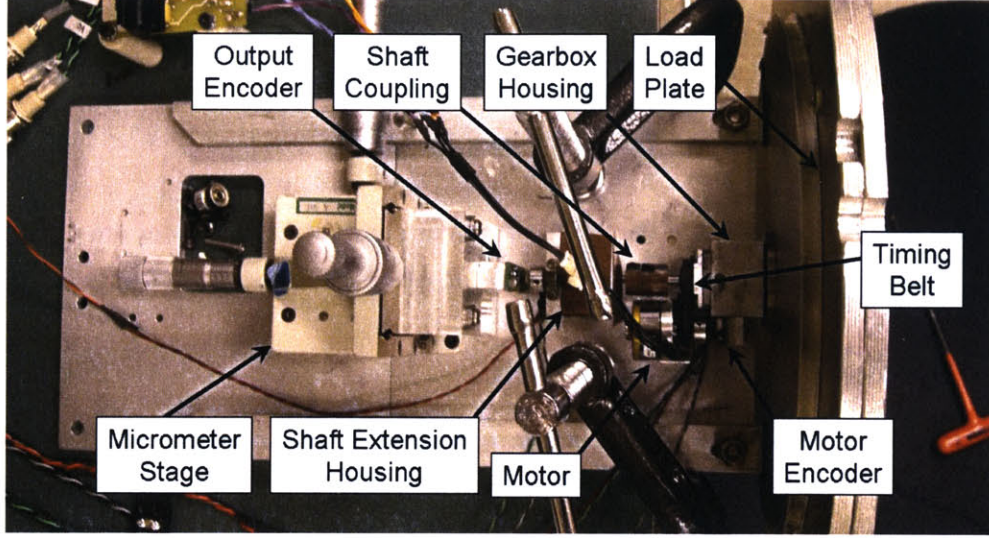


Figure 3-1: Picture of the Benchtop Teststand used for the work in this thesis.

coils (three for each phase) located on the stator connected in a Y configuration. The stator coils have been rewound from the original 18 winds per coil to 42 winds per coil to increase the motor's torque constant. This effectively tuned the peak motor efficiency to 5000RPM, the desired operating velocity for the snake's sidewinding gait.

The torque constant ($k_{t,p}$) was measured by running the motor at various speeds and measuring the voltage produced on each phase, also known as the back EMF. Assuming that the rotor magnets produce a sinusoidal magnetic field with reference to position the per phase voltage (V_i) is given by:

$$V_i(\phi_e, \dot{\phi}_m) = k_{t,p} \sin(\phi_e + \psi_i) \dot{\phi}_m \quad i = A, B, C \quad (3.1)$$

Where ϕ_m is the motor position and $\dot{\phi}_m$ is the motor velocity. $\phi_e = \frac{P_r}{2} \phi_m$ is the motor electrical position, P_r is the number of rotor magnets and ψ_i is the phase offset. The voltage measured between two phases (V_{i-j}) at a given angular velocity ($\dot{\phi}_m$) is then given by taking the difference of the two phase voltages.

$$V_{i-j}(\phi_e, \dot{\phi}_m) = V_i(\phi_e, \dot{\phi}_m) - V_j(\phi_e, \dot{\phi}_m) = \sqrt{3} k_{t,p} \cos(\phi_e + \frac{\psi_i + \psi_j}{2}) \dot{\phi}_m \quad (3.2)$$

It turns out that because the phases are all 120 degrees apart, the amplitude of the voltage across two phases is equal to the amplitude of the phase voltage scaled by the square root of three. The per phase torque constant can then be found in terms of the amplitude of the back EMF measured between two phases.

$$k_{t,p} = \frac{V_{i-j, Amplitude}}{\sqrt{3} \dot{\phi}_m} \quad (3.3)$$

$k_{t,p}(Nm/Amps)$	$R_c(\Omega)$	$L_c(\mu H)$
0.00691	1.1	233

Table 3.1: Motor Parameters

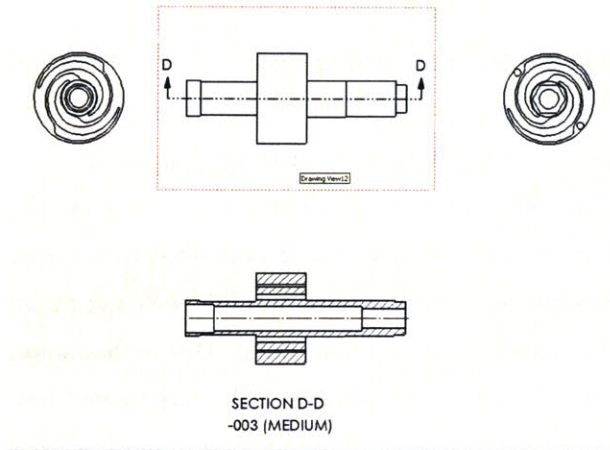
The measurements obtained of the per phase torque constant for the motor are given in Table 3.1 along with measurements of the coil resistance (R_C) and coil inductance (L_C).

3.1.2 Harmonic Geardrive and Belt

In order to produce the required torque, a gear reduction was placed at the output of the motor. The reduction is provided by the combination of a harmonic gear drive and a timing belt that connects the motor shaft with the input to the harmonic drive. The configuration of the motor and transmission are shown in Figure 3-1. The harmonic drive is a CSF-5-100-2XH-F produced by Harmonic Drive Systems Inc. and delivers a reduction of 100:1. The belt delivers a 2.3:1 reduction making the overall transmission ratio 230:1 (This $N : 1$ transmission ratio will be referred to by the constant N throughout this thesis). This large transmission ratio in combination with the geometry of the harmonic drive made series elasticity essential for the survival of the HISS robot. In general harmonic drives are not backdrivable because the high ratio scales the input damping and motor inertia by a factor of N^2 as seen from the environment, while nonlinearities, such as stiction forces, are scaled by a factor of N . As a result the input system looks highly constrained to the environment. Solid shafts were initially used on HISS to connect the output of the transmission to the load and it was found that even small amplitude high frequency torque application by the motor or torque disturbances by the environment would cause the harmonic drives to break. Furthermore, at low frequencies the continuous failure torque was found to be as low as 1.7 Nm on some drives making overloading under all operating conditions a concern.

3.1.3 Compliance

To provide the system with series elasticity a novel rotary spring shaft was designed. The shaft has a spiral configuration that gives it symmetry under both positive and negative deflections. The design is shown in Figure 3-2. It is linear up to $2Nm$ where it becomes stiffer due to contact of the spiral sections. The spring shaft's unique compact design allows it to fit inside the harmonic drive making for a compact shock tolerant unit. The location of the spring is shown in Figure 3-3. It connects to the harmonic drive through two pins on the outer edge of the spiral portion. A 5mm thick solid shaft is inside the spiral portion and interfaces with the load through a 4mm hex piece at its end. The other end of the shaft is used as the encoder interface. The spring shaft is made out of VascoMax 350C, specialty steel produced by Allvac, giving it good resistance to wear and corrosion.



(a) CAD Drawing of the Spring Shaft.



(b) Picture of the Spring Shaft.

Figure 3-2: Pictures of the spring shaft used as the series elastic element.

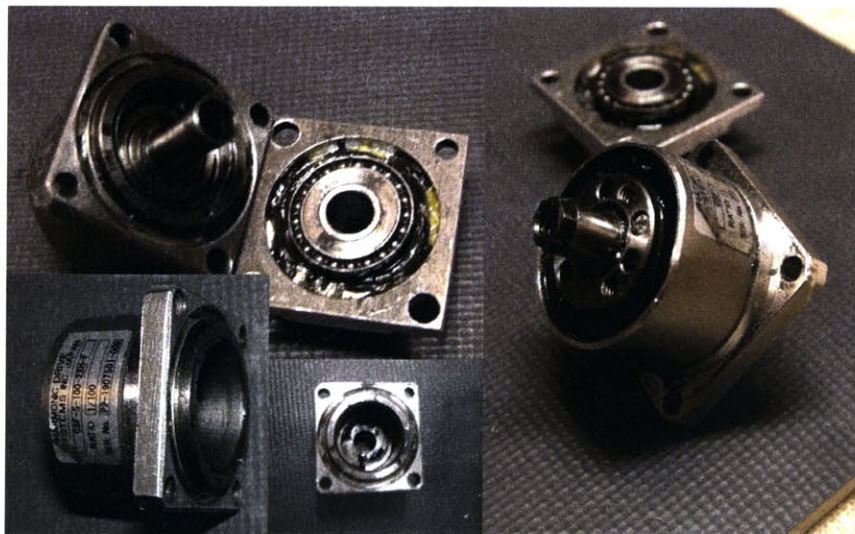


Figure 3-3: Picture of the Harmonic Drive/Spring Shaft interface.

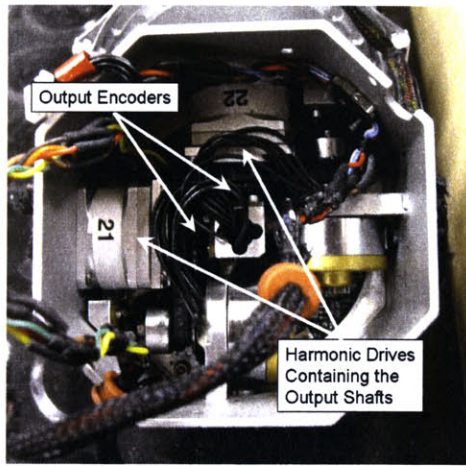
3.1.4 Sensors

Position of the motor shaft and the output of the spring shaft are sensed by RLS AM256 magnetic encoder IC's [RLS]. The encoders operate using Hall Effect principles to detect the magnetic flux density at the surface of the chip. The magnetic field is created by a diametrically polarized permanent magnet of cylindrical shape that is placed at the end of a rotating shaft. The encoder outputs analog sine and cosine signals that represent the magnetic field distribution. From these analog signals absolute position is calculated. The locations of the sensors are shown in Figure 3-1.

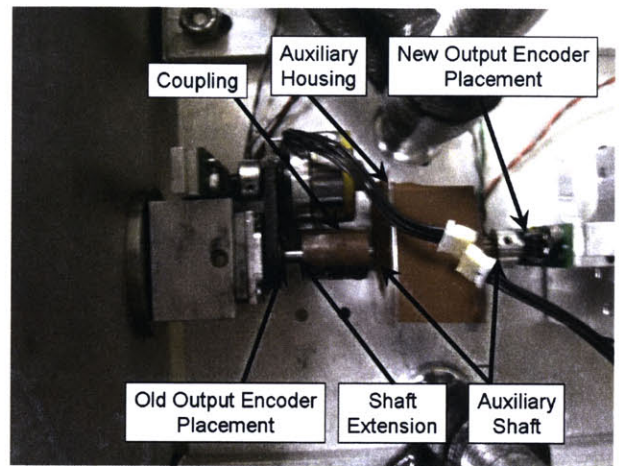
The motor encoder is placed at the end of the motor shaft, as can be seen from the photo. The output encoder, however, is placed at the end of an auxiliary shaft that is connected to the spring shaft through a flexible coupling. On the HISS robot the output encoder was positioned at the end of the spring shaft in a similar configuration to the motor encoder (Figure 3-4a). Due to the compact setup of the harmonic drive and spring shaft the magnet for the output encoder was located inside the harmonic drive's input pulley. A bearing was placed between the input pulley and the output shaft to make sure the two parts could move freely relative to each other. When the harmonic drive is actuated the input pulley runs in the opposite direction as the output shaft at 100 times the speed. Due to hysteretic magnetization of the bearing's outer race this relative motion caused an error in the output position detected by the encoder upon changes in direction (Figure 3-5). In order to avoid this error the magnet for the output encoder had to be moved outside of the pulley so its magnetic field could not be skewed by magnetic hysteresis of the bearing. Unfortunately, the shaft could not simply be extended because the nonlinear motion created by the harmonic drive would be amplified causing alignment error between the encoder and the magnet. To solve this problem an auxiliary output encoder shaft was added with its own housing to maintain encoder alignment (Figure 3-4b). Plots of the output encoder response are shown in Figure 3-5.

The encoders used are largely intolerant to misalignment of the magnet with respect to the encoder IC. A misalignment of $0.2mm$ for a magnet that is on the edge of the polarization symmetry tolerance will result in an additional position error of ± 0.6 degrees [Rotary and , RLS]. In order to minimize this error the output encoder IC is mounted on a three dimensional micrometer stage that is adjusted to achieve the optimal alignment. Even after the stage has been adjusted some integral nonlinearity remains in the measured position. This is the combination of the effect of noise and non-idealities on the measurement and is shown in Figure 3-6. The large amplitude nonlinearity is repeatable over a revolution of the output shaft and is compensated for in software by using a lookup table. The output position error before the correction is applied is shown in Figure 3-6.

The encoder noise for the AM256 is shown in Figure 3-7. A first order low pass filter with a corner frequency at $1000rad/s$ is used to filter the motor position signal. This filter is used mainly for control and display and is applied after the raw signal has been used for commutation. The motion seen at the output encoder is decoupled from the motor shaft by the harmonic drive and



(a) Hiss Output Encoder Placement.



(b) Thesis Output Encoder Placement.

Figure 3-4: Pictures of the output encoder placement on the Hiss vehicle and the Thesis hardware. In order to avoid magnetization error, the output encoder had to be moved away from the end of the spring shaft to an auxiliary shaft.

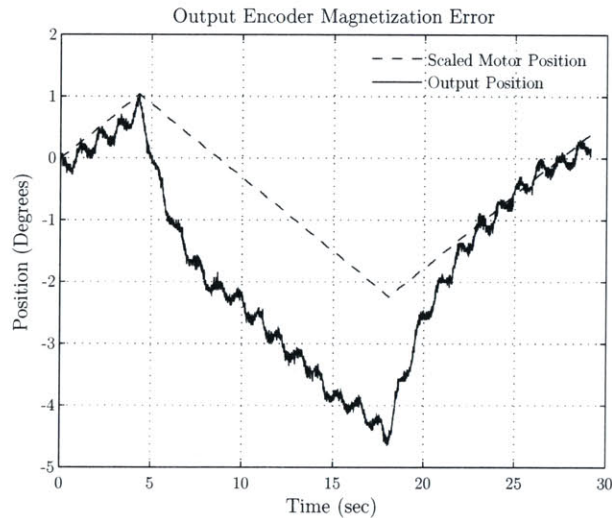


Figure 3-5: Plot of the output encoder error that was present on the HISS vehicle due to magnetization of a bearing. This data was taken with a solid shaft substituted in for the spring shaft so there should be no difference between the scaled motor position and the output position.

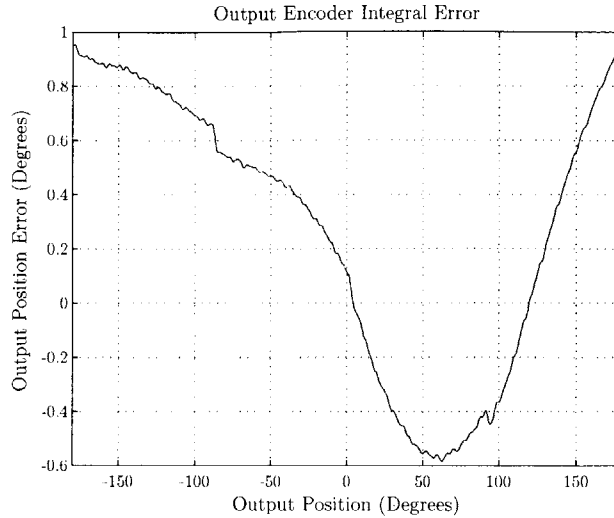


Figure 3-6: Integral Encoder Error upon a revolution of the output shaft.

compliance and does not operate at as high a bandwidth as the motor. It is filtered by a sixth order Bessel filter with a cutoff frequency at $200rad/s$. A Bessel Filter is used in order to maintain a linear phase response through the passband which minimizes distortion of the filtered signal. More than anything these filters are essential to reduce noise in the velocity (differential) signal. A plot of the motor angular velocity and output angular velocity before and after filtering are provided in Figure 3-8.

3.1.5 Electronics

The motor is powered by a custom-built driver circuit that is responsible for maintaining the desired current in each phase. A schematic of the circuit is given in Figure 3-9 and an operational block diagram is given in Figure 3-10. The current in phase A and phase B are controlled by analog current loops while the voltage on phase C is controlled to ensure that the motor operates in the middle of the supply's voltage range. The circuit is designed to operate at supply voltages up to $\pm 18Volts$ but is kept at $\pm 12Volts$ for the work in this thesis. Similarly the circuit can drive currents up to $\pm 6Amps$ but is limited to $3.5Amps$.

There are a few notable components in the driver circuit. At the heart of the circuit is the OPA549 Power Operational Amplifier from Burr Brown. It can maintain an output voltage close to its supply rails which can be set up to $\pm 18volts$ and provide continuous current up to 8amps. Also it has an open loop unity gain crossover at $1MHz$ meaning it can deliver current at high frequencies. The INA128 Instrumentation Amplifier from Burr Brown monitors the current being delivered to each phase by measuring the voltage across 0.025Ω current sense resistors from Ohmite. At $100kHz$ it has a CMRR of $60dB$ allowing a current control bandwidth that is much higher than the dSPACE

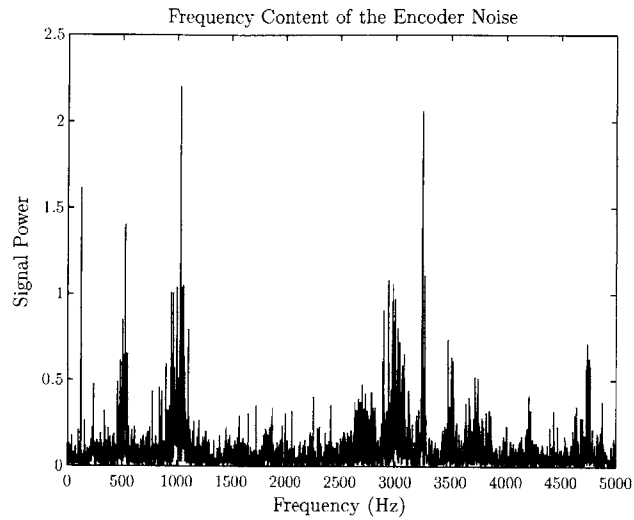


Figure 3-7: FFT of the encoder noise.

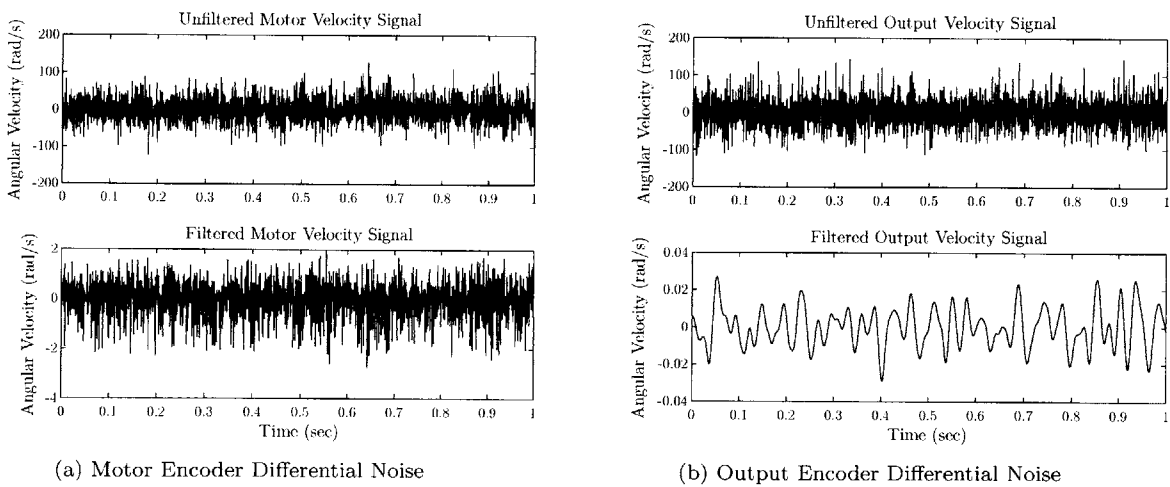


Figure 3-8: Noise on the velocity signals obtained by differentiating the encoder position signals. These plots illustrate the magnitude of noise on the unfiltered signals and the importance of applying strong filters.

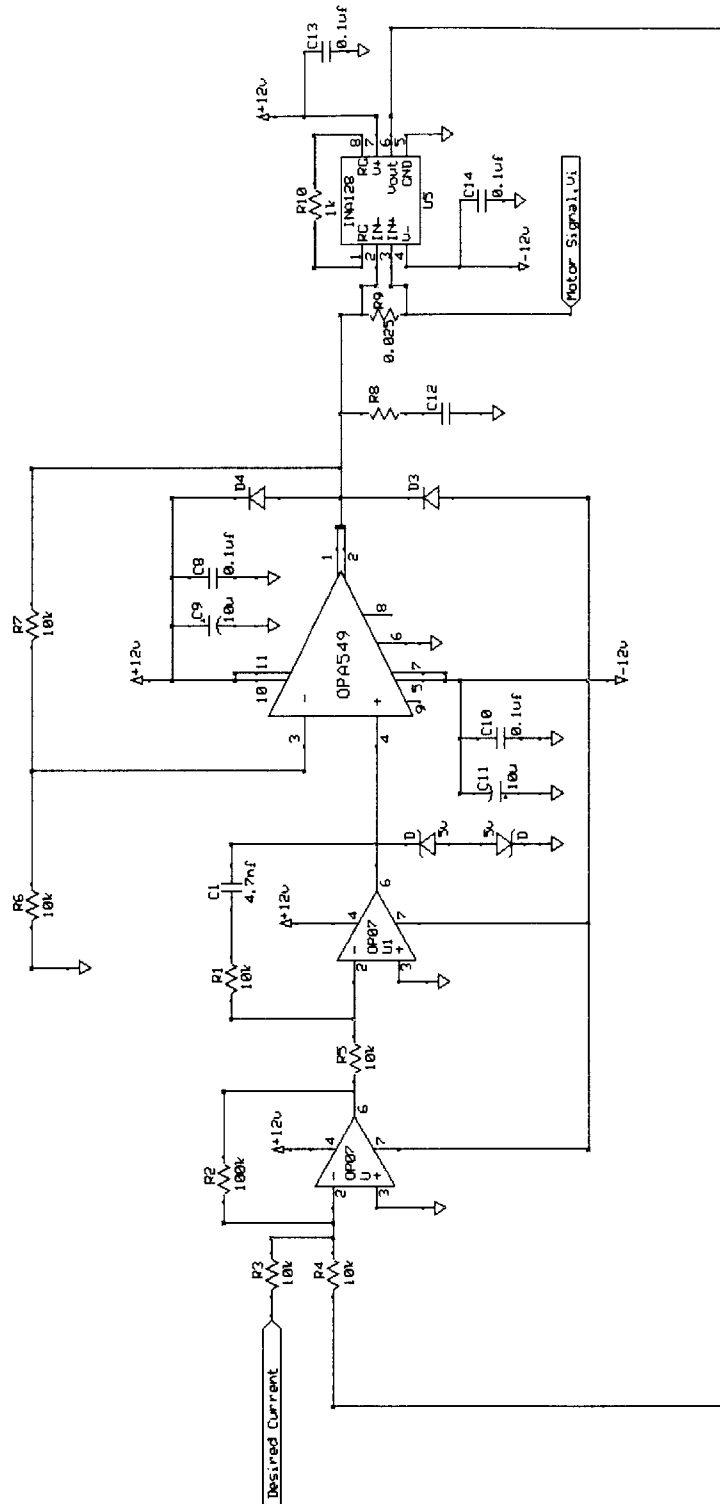


Figure 3-9: Schematic of the Electronics used to drive the motor. This schematic shows the entire circuit controlling a single phase of the motor. Phase A and B had current control loops and are represented by this schematic. Phase C only needs to control voltage so the INA128 and two OP27s are not present on that phase.

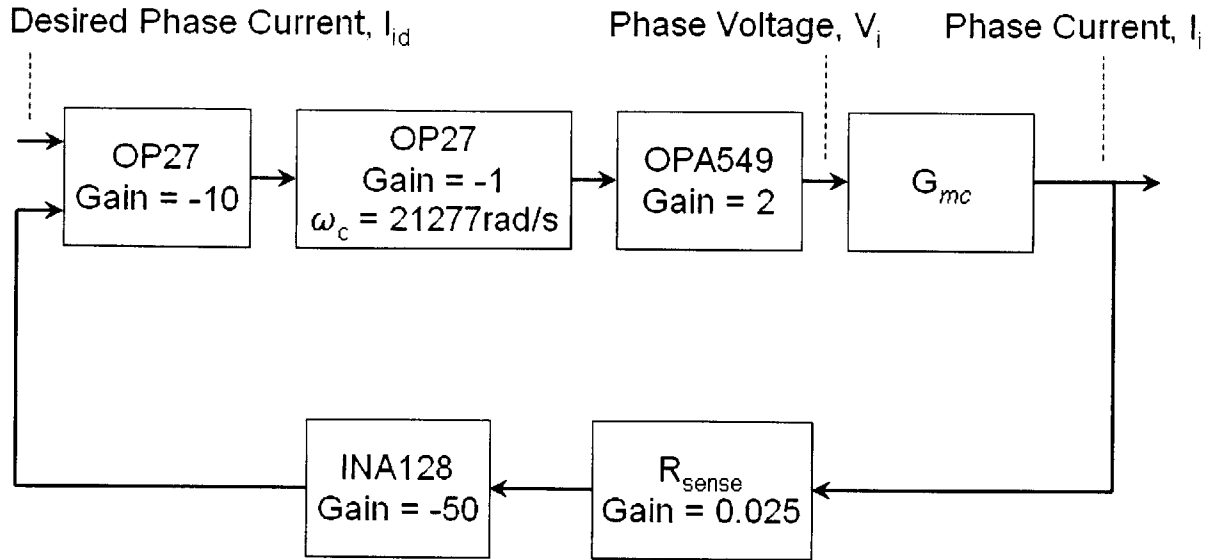


Figure 3-10: Electronics Operational Block Diagram. The block diagram represents the operation of phases A and B. Phase C only consists of the system plant (G_{mc}) and the OPA549.

computer's sampling frequency. It also has a high limit on common mode voltages which is essential for high speed motor control. The current loop is controlled with a PI compensator that is made out of OP27 low noise operational amplifiers from Analog Devices. Zener diodes are used to provide a 5volt saturation limit on the PI compensators to ensure that the common mode voltage limit of the INA128 is not reached. The passive component values are a result of the analysis of the analog current loop in Section 3.2.

3.1.6 Computer

The computer used for this thesis is a dSPACE ds1003/ds1004 (Alpha Combo) operated with a constant sampling rate of 10 kHz and run out of a PX10 expansion box. The ds1003 is powered by a Texas Instruments TMS320C40 digital signal processor (DSP) and was primarily used as the I/O controller. The ds1004 is powered by a DEC Alpha AXP21164 DSP and was used for the majority of the application's calculations. The ds1004 used stored data from the last clock cycle in order to minimize wasted processor time per cycle and increase the calculation capability of the system. Also in the expansion box are a ds2003 a 32 channel A/D board and a ds2103 32 channel D/A board both sampled at the update rate of the Alpha Combo. The resolution of both the D/A and the A/D is 16bits at either $\pm 5 \text{ Volts}$ or $\pm 10 \text{ Volts}$. The $\pm 10 \text{ Volts}$ setting was used for this thesis

3.2 Motor Commutation

The motor is the power delivery device for the actuator. It converts electrical energy from a source to mechanical energy and controls the rate at which that energy is transferred to the load. In order to achieve good control of a load it is important that the motor be able to deliver energy in a linear and predictable manner. This section gives a model of the motor electronics and derives the governing equations, a commutation law that achieves a linear current to torque relationship is found, and finally the implementation of that control law is described.

3.2.1 Motor Electrical Model

The motor is a three phase brushless motor where the phases are connected in a Y configuration. Each phase consists of a series combination of the winding resistance (R_c), the winding inductance (L_c) and a nonlinear gyrator (characterized by gyrational constant $k_{t,p}$ otherwise known as the per phase torque constant) that represents the interaction between the rotor's permanent magnets and the stator coils. This interaction is responsible for converting electrical energy to mechanical energy and is described by Eqs. 3.4 and 3.5 below.

$$Vb_i(\phi_e, \dot{\phi}_m) = k_{t,p} \sin(\phi_e + \psi_i) \dot{\phi}_m \quad i = A, B, C \quad (3.4)$$

$$\tau_i(\phi_e, i_i) = k_{t,p} \sin(\phi_e + \psi_i) i_i \quad i = A, B, C \quad (3.5)$$

τ_i is the per phase motor torque and i_i is the per phase current. The subscript i denotes the motor's phases A, B and C. A model of the motor electronics is shown graphically in Figure 3-11. Variables that haven't been referenced but are shown in the figure are V_i which is the node voltage at the input of each phase and V_0 which is the node voltage at the center of the Y.

The voltage across each phase is found by taking the sum of the voltage dropped across the lumped elements representing the coil resistance, coil inductance and the nonlinear gyrator

$$V_i(i_i, V_{bi}, V_0) = R_c i_i + L_c \frac{di_i}{dt} + V_{bi} + V_0 \quad (3.6)$$

By using Kirchhoff's current law at the center node the relationship between the current on each phase is found.

$$\sum_{i=A}^C i_i = 0 \quad (3.7)$$

Due to the 120degree difference between the phases the sum of the back EMF also equates to zero.

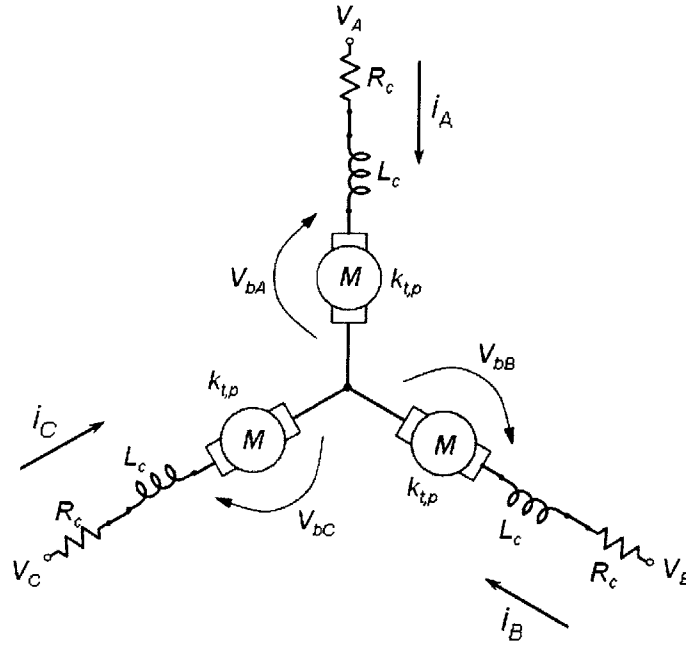


Figure 3-11: Motor Electrical Model.

$$\sum_{i=A}^C V_{bi} = k_{t,p} \dot{\phi}_m \sum_{i=A}^C \sin(\phi_e + \psi_i) = 0 \quad (3.8)$$

3.2.2 Commutation Law

In order to commutate the motor the current on all three phases must be controlled. Due to the motor configuration controlling the current on only two of the phases dictates the current for all three phases. This is because the current on the last phase, according to equation 3.7, is the resulting sum of the controlled currents. To achieve the desired current on the controlled phases the node voltage on those phases is defined by an analog current control loop (see section 3.2.3). The node voltage of the last phase is then free to be chosen so that the commutation voltages stay centered between the saturation limits of the electronic hardware. This is guaranteed if the voltage at the center of the Y is maintained at the reference voltage (V_{Ref}) of the driver circuit (in our case, ground). By summing the node voltages given in equation 3.6 and substituting in equations 3.7 and 3.8 a relation for V_0 in terms of the node voltages is found.

$$V_0 = \frac{1}{3}(V_A + V_B + V_C) \quad (3.9)$$

Setting V_0 to zero then yields a relation for the node voltage on the uncontrolled phase in terms

of the voltage on the two controlled phases.

$$V_C = -V_A - V_B \quad (3.10)$$

As mentioned earlier the main purpose of the commutation law is to ensure that the motor exhibits a linear relationship between commanded current (I_d) and motor torque (τ_m). As this is not enough to define a unique law, a secondary constraint that the efficiency of the motor during constant speed operation is maximized is also imposed. The torque produced by the motor is found by summing the per phase torques.

$$\tau_m = k_{t,p}(\sin(\phi_e)i_A + \sin(\phi_e - \frac{2\pi}{3})i_B + \sin(\phi_e + \frac{2\pi}{3})i_C) \quad (3.11)$$

Where ψ_i from Eq. 3.4 is equal to zero, $-\frac{2\pi}{3}$ and $\frac{2\pi}{3}$ for phases A, B and C respectively. By substituting Eq. 3.7 and solving for i_B , a relation for the current on phase B is found in terms of the current on phase A and the motor torque.

$$i_B = -\frac{\tau_m/k_{t,p} + \sqrt{3}\cos(\phi_e + \frac{\pi}{3})}{\text{sqrt}3\cos(\phi_e)} \quad (3.12)$$

The electrical efficiency (η_{Elec}) of the motor is given by the ratio of mechanical power supplied by the motor ($P_{Out, Elec}$) to input power drawn by the motor ($P_{In, Elec}$). This relation is given in equation 3.13 with the mechanical power supplied given in Eq. 3.14 and the input power is given in Eq. 3.15.

$$\eta_{Elec} = \frac{P_{Out, Elec}}{P_{In, Elec}} \quad (3.13)$$

$$P_{Out, Elec} = \sum_{i=A}^C \dot{\phi}_m \tau_i = \dot{\phi}_m \tau_m \quad (3.14)$$

$$P_{In, Elec} = P_R + P_L + P_{Out, Elec} = \sum_{i=A}^C (R_c i_i^2 + L_c i_i \frac{di_i}{dt} + \dot{\phi}_m \tau_i) \quad (3.15)$$

In Eq 3.15 P_R represents the resistive losses in the copper wire and P_L represents the inductive power stored in the coils.

If a constant motor torque is achieved by the commutation law the mechanical power supplied at constant velocity is a constant. The efficiency can then be maximized by minimizing the input power drawn by the motor. Substituting Eqs. 3.12 and 3.7 into Eq. 3.15 gives the input power in terms of the current on phase A.

$$P_{In,Elec}(i_A) = P_R(i_A) + P_L(i_A) + P_{Out,Elec} = 2R_c g(i_A, \dot{\phi}_e t) + L_c \frac{d}{dt} g(i_A, \dot{\phi}_e t) + \tau_m \dot{\phi}_m \quad (3.16)$$

$$g(i_A, \dot{\phi}_e t) = \frac{(\frac{\tau_m}{k_{t,p}})^2 - 3 \sin(\dot{\phi}_e t) \frac{\tau_m}{k_{t,p}} i_A + \frac{9}{4} i_A^2}{3 \cos^2(\dot{\phi}_e t)}$$

Noticing that power is stored in the inductors and not lost and again using the fact that $P_{Out,Elec}$ is a constant, a suitable commutation law can be found by minimizing the resistive losses. Setting the derivative of P_R with respect to i_A to zero and solving for i_A the optimal commutation current for phase A is found. Subsequently the commutation laws are found through back substitution and are given in Eqs. 3.17, 3.18 and 3.19.

$$i_A = \frac{\tau_m}{k_t} \sin(\phi_e) = I_d \sin(\phi_e) \quad (3.17)$$

$$i_B = \frac{\tau_m}{k_t} \sin(\phi_e - \frac{2\pi}{3}) = I_d \sin(\phi_e - \frac{2\pi}{3}) \quad (3.18)$$

$$V_C = -V_A - V_B \quad (3.19)$$

$$k_t = \frac{3}{2} k_{t,p}$$

Where the desired current is linearly related to the motor torque through the motor constant (k_t).

3.2.3 Implementation

Analog Current Loop

The desired phase current, given by the commutation law, is calculated by the dSPACE computer and output to the electronic driver circuit. Analog current loops are wrapped around phases A and B of the motor to maintain the desired current in each phase. A block diagram of the current loop¹ is given in figure 3-12. Using the voltage on phase C to hold V_0 at V_{Ref} effectively decouples the phases from each other yielding the simplified system plant ($G_{mc,phase}$) for each phase given in Eq. 3.20. The open loop bode plot of $G_{mc,phase}$ is given in Fig. 3-13a.

$$G_{mc,phase}(s) = \frac{i_i(s)}{V_i(s)} = \frac{1}{L_c s + R_c + \frac{3}{2} k_{t,p}^2 / b_m} \quad (3.20)$$

A proportional integral (PI) compensator, composed of a pole and a zero, is used in the current control loop. It's transfer function is given in Eq. 3.21. The compensator's pole lies at the origin, which adds low frequency gain and ensures that when the loop is closed the steady state error

¹identical current loops

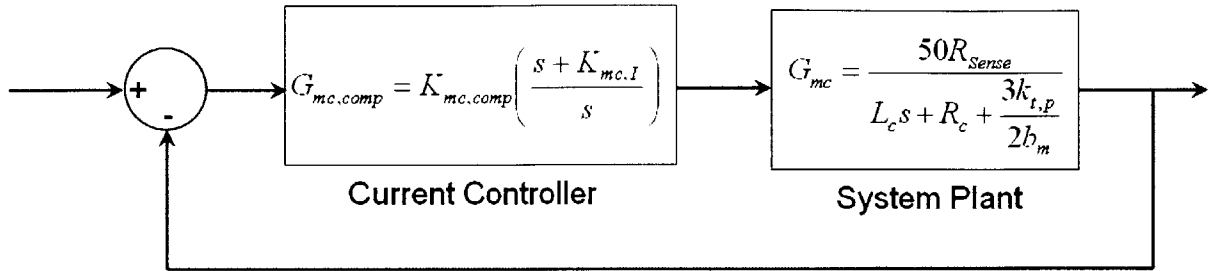
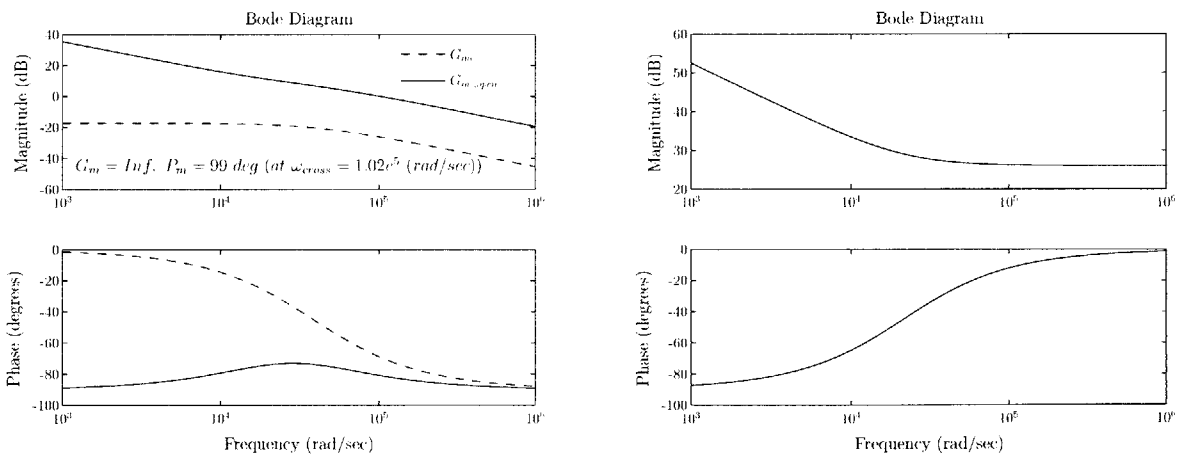


Figure 3-12: Current Loop Block Diagram



(a) Bode of the phase current from phase voltage

(b) Bode of the current loop compensator

Figure 3-13: Current Loop Bode Plots. (a) Shows bode plots of the system plant and of the open loop transfer function after the compensator has been applied. This plot displays the unity gain crossover for the system and the phase margin (P_m) achieved at the crossover frequency. (b) Shows the bode plot of the current loop compensator.

K_{mc}	$K_{mc,comp}$	$K_{mc,I}$	ω_{mc} (rad/s)
107296	20	21277	100krad/s

Table 3.2: Current Loop Parameters

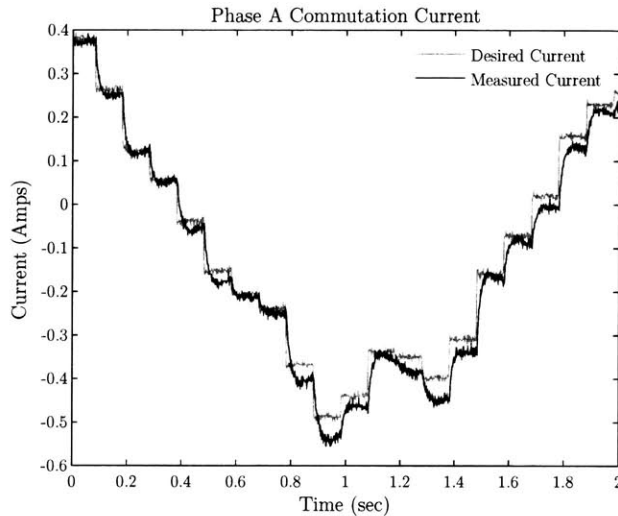


Figure 3-14: Controlled Commutation Current on Phase A. The plot shows that the current settles adequately within one sample period of the computer.

converges to zero. The zero is placed close to the pole of the system plant by adjusting the integral gain ($K_{mc,I}$). This is done to achieve the stable open loop transfer function $G_{mc,open} = K_{mc}/s$, where K_{mc} is the overall loop gain. The motor angular velocity limit based on the hardware is 1000rad/s. This requires a sampling rate of 10kHz in order to have at least ten samples per electrical cycle. In turn the bandwidth of the current loop is set so that the current settles adequately within the sample period. The compensator gain ($K_{mc,comp}$) is adjusted so that the open loop unity gain crossover occurs at $\omega_{mc} = 100krad/s$. The gains used in the current loop PI controller are given in Table 3.2. A bode plot of the open loop transfer function is given in Figure 3-13a and a bode plot of the compensator is given in Figure 3-13b. The controlled current during motor commutation is shown in Figure 3-14

$$G_{mc,comp}(s) = K_{mc,comp} \left(\frac{s + K_{mc,I}}{s} \right) \quad (3.21)$$

Angle Advance

A delay of two sample periods ($t_{delay} = 200\mu s$) is introduced by the dSPACE computer due to the data acquisition and calculation. This delay is shown in Fig. 3-15. As the motor angular velocity is increased, this delay becomes a much larger portion of the electrical commutation cycle. Conse-

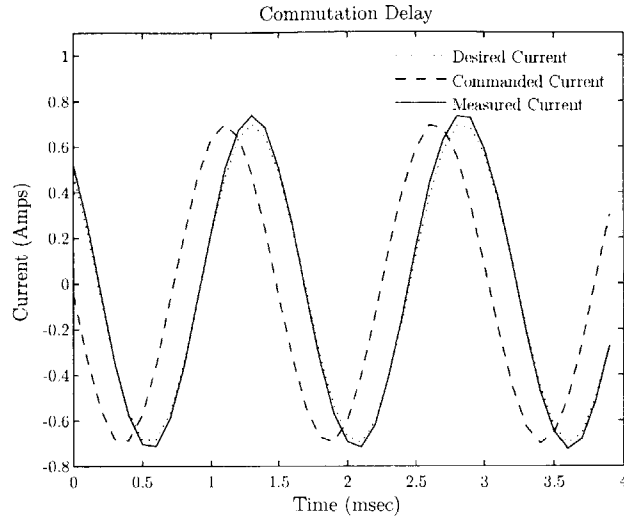


Figure 3-15: Plot of the commutation current delay cause by the data acquisition and processor computation. The plot shows how the commanded current is calculated two sample periods ahead of when it is desired to overcome the delay.

quently the commutation current lags behind the desired phase current defined by the commutation law creating a drop in both output torque and efficiency. In order to maintain actuator linearity a feedforward term based on the motor position and the motor angular velocity is introduced. This term advances the angle used to calculate the commutation current by two sample periods so that after the delay the desired current is achieved. The corrected commutation current is also shown in Fig 3-15.

3.3 Motor Model

Assuming a linear command-to-torque relationship is achieved, the motor electronics can be viewed as a torque source as long as the motor is within its saturation limits. It is then reasonable to reduce the total motor model to the simple mass damper system given in Eq 3.22, where J_m is the motor inertia and τ_f is the friction torque. The motor model is shown graphically in Fig 3-16. The standard motor model used for control assumes that friction torque is a linear term that is proportional to the motor angular velocity. This model yields the transfer function given in Eq. 3.23. The measured bode plot of the motor, however, deviates from this linear model as shown in Fig. 3-17a. A time domain response to a sinusoid at 1rad/s is given in Fig. 3-17b. It shows that the majority of the deviation from the linear model is due to nonlinear effects at low speeds.

$$J_m \ddot{\phi}_m + \tau_f = \tau_m \quad (3.22)$$

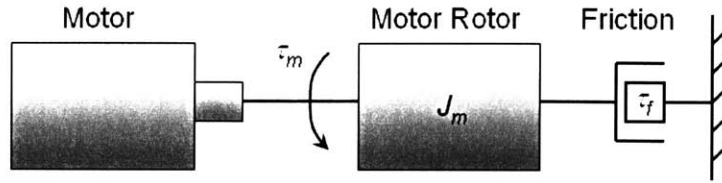


Figure 3-16: Motor Mechanical Model

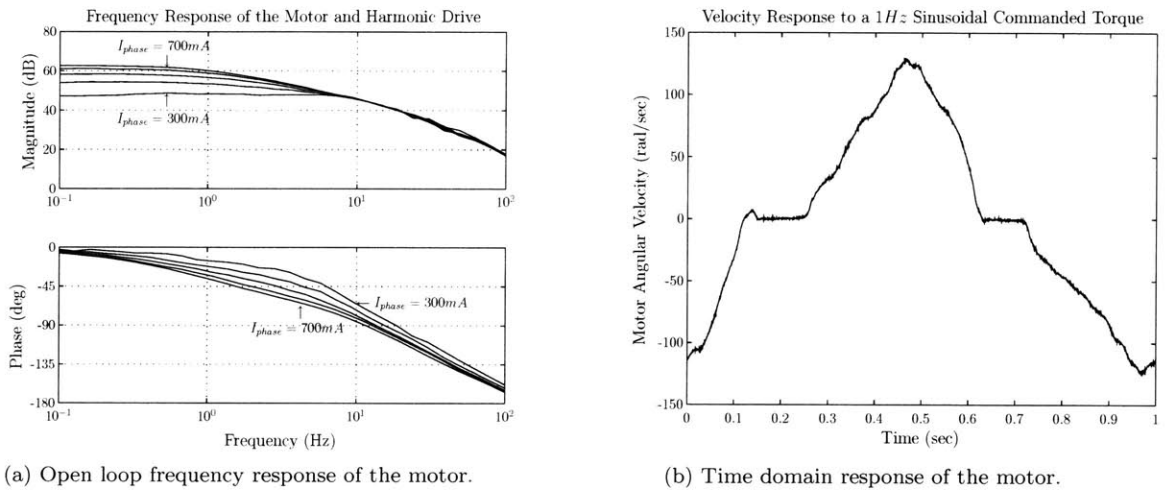


Figure 3-17: Plots of motor response without any compensation. (a) Bode Plot of the motor velocity from the motor current. The frequency response of the motor was taken at multiple values of current ranging from 300mA to 700mA. The plot shows how nonlinear effects create different responses based on the size of the input which hinders efforts to characterize the system and can hurt the effectiveness of control. (b) Open loop time domain response to a 1Hz sinusoid input. Due to nonlinear effects the rotor stops for a portion of each cycle.

$$G_m(s) = \frac{\dot{\phi}_m(s)}{\tau_m(s)} = \frac{1}{J_m s + b} \quad (3.23)$$

There are two nonlinear phenomenon responsible for this deviation. The first is cogging torque, a positional torque ripple caused by magnetic interaction between the stator and the rotor magnets. The second is static friction or “stiction”, which is a torque that occurs due to the metal to metal contact forces in the bearings.

3.4 Nonlinearity Compensation

The presence of nonlinear effects such as cogging torque and stiction are undesirable because they can reduce the effectiveness of standard control techniques or even introduce undesired stable equilibria

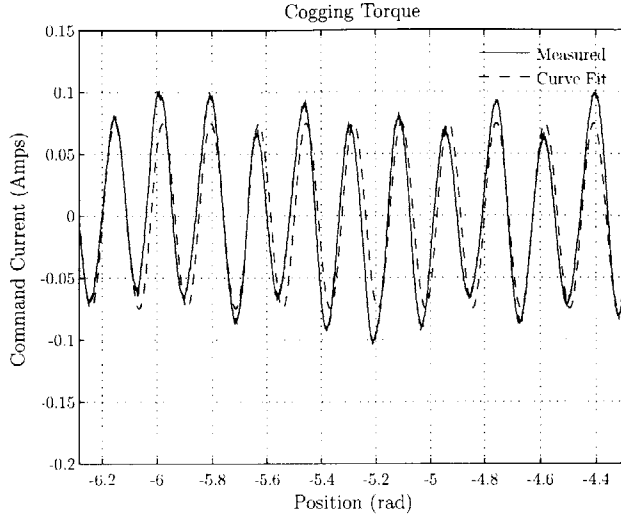


Figure 3-18: Plot of the torque required for the PD controller to overcome cogging torque and hold a position.

such as limit cycles. With the proper models, however, feedforward terms can be introduced to compensate for these nonlinearities. In this section the motor cogging torque and stiction are characterized and feedforward terms are added to the command signal to linearize the system.

3.4.1 Cogging torque

Cogging torque is a periodic torque ripple that occurs due to the interaction between the rotor’s permanent magnets and the stator slots or “teeth”. This torque is position-dependent and is produced regardless of stator current. The periodic nature of cogging torque causes a number of stable and unstable equilibria which can cause large errors under position control. Fortunately this disturbance is repeatable over a revolution of the motor and therefore can be compensated for in software.

In order to measure the cogging torque, a high gain proportional derivative (PD) position controller was implemented and the torque required to maintain a given position was measured about a revolution of the motor. A portion of this data is plotted in Fig. 3-18. A single harmonic curve fit was applied and a relation for cogging torque in terms of motor position was found and is given in Eq. 3.24. By adding this term to the command signal much of the disturbance due to the cogging torque was suppressed which can be seen from the reduction in position error under PD position control shown in Fig 3-19.

$$\tau_{cog}(\phi_m) = 7.69 \times 10^{-4} \sin(36\phi_m - 1.5796) \quad (3.24)$$

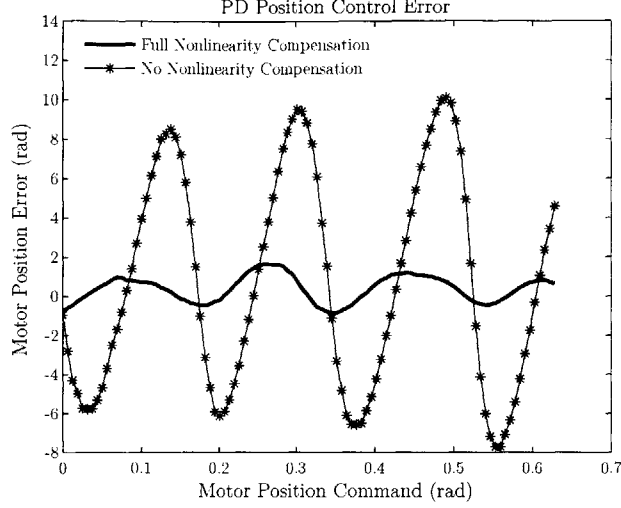


Figure 3-19: Plot of motor position error under PD control due to the motor's cogging torque. The plot illustrates how the cogging torque compensation improves the effectiveness of the PD control.

3.4.2 Stiction

The term stiction describes the forces resulting from microscopic irregularities of two surfaces in contact. An analogy that is commonly used is that the points of contact on the microscopic level act like wire bristles that exhibit a spring damper effect. Small deflections from rest produce large forces in the bristles until a critical force is reached causing the points of contact to start to slip. Canudas et al present a dynamic model that effectively describes this interaction [Canudas de Wit et al., 1995] and a technique for measuring the model parameters [Canudas De Wit and Lischinsky, 1997]. These methods are used in this thesis to characterize the bearing stiction and implement compensation for it.

The dynamic stiction model introduced by Canudas et al, called the LuGre Model, is composed of a rotor velocity state and an internal state (z) representing the average bristle deflection. The LuGre Model is given in Eqs. 3.25 and 3.26, where σ_0 , σ_1 , α_0 , α_1 , α_2 and $\dot{\phi}_{m,0}$ are all constant parameters of the model.

$$\tau_f = \sigma_0 z + \sigma_1 \frac{dz}{dt} + \alpha_2 \dot{\phi}_m \quad (3.25)$$

$$\frac{dz}{dt} = \dot{\phi}_m - \frac{\sigma_0}{g(\dot{\phi}_m)} z |\dot{\phi}_m| \quad (3.26)$$

$$g(\dot{\phi}_m) = \alpha_0 + \alpha_1 e^{-(\dot{\phi}_m / \dot{\phi}_{m,0})^2}$$

σ_0 is the stiffness of the bristles while σ_1 is the damping. α_0 is the critical force required for the bristles to start to slip. α_1 and $\dot{\phi}_{m,0}$ describe the increase in friction force that takes place at slow speeds due to lubrication called the Stribeck Effect. α_2 is the standard viscous damping. These

	σ_0 ($\frac{Nm}{rad}$)	σ_1 ($\frac{Nm}{rad/s}$)	α_0 (Nm)	α_1 (Nm)	α_2 ($\frac{Nm}{rad}$)	$\dot{\phi}_{m,0}$ (rad/s)
Motor	0.0001	0.0385	0.00035	0	N/A	0
Harmonic	0.0005	0.82	0.00478	0	$5e^{-6}$	0

Table 3.3: Stiction Parameters

constants are measured for both the motor and the harmonic drive using the techniques described in [Canudas De Wit and Lischinsky, 1997] and are given in Table 3.3. Using the parameters measured, the LuGre Model is implemented in software to actively calculate the stiction torque. This torque is then added to the command signal to compensate for the bearing stiction. The effect of the friction compensation with respect to velocity is shown in Fig. 3-21.

During implementation of the stiction compensation it was found that stability of the stiction model, was highly sensitive to motor speed and sampling bandwidth. At higher motor speeds the average bristle deflection state would become unstable and the compensation scheme would cause the motor current to spike and saturate. The explanation for this phenomenon came from a more detailed analysis of the stiction model, specifically the internal state z . Eq. 3.26 is a nonlinear differential equation describing the change in bristle deflection in terms of the motor velocity and the bristle deflection. By assuming a constant velocity the system takes on the form of a linear first order system.

$$\dot{z} = \dot{\phi}_{m,const} \left(1 - \frac{\sigma_0}{\alpha_0} z \right) \quad (3.27)$$

Where $\dot{\phi}_{m,const}$ represents the motor velocity as a constant. By transferring Eq. 3.27 into the Laplace domain and solving for $z(s)$ the system takes the form of a standard low pass filter.

$$z(s) = \frac{\dot{\phi}_{m,const}}{s + \dot{\phi}_{m,const} \frac{\sigma_0}{\alpha_0}} \quad (3.28)$$

This equation can also be looked at as the result of closing a proportional control loop around an integrator as is shown in Figure 3-20. The input to the control loop (u) is an impulse and the motor velocity is the proportional gain. The open loop phase margin of the continuous system will always be 90 degrees due to the single pole in the system plant (the integrator) regardless of the gain. When the system is implemented digitally, however, the sampling delay causes phase to rolloff at high frequencies so that when the gain is increased adequate phase margin is no longer maintained and the system becomes unstable. In the hardware implementation the system gain of the stiction model was limited by setting saturation limits on the motor velocity term at $\pm 100 rad/s$. With the saturation limits in place the system remains stable at high velocities. Moreover, the stiction force converges to a constant at high velocities, therefore the lack of system gain does not hinder its calculation.

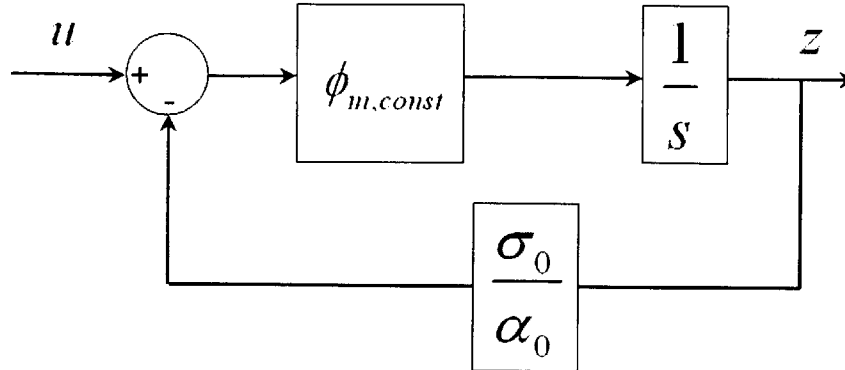


Figure 3-20: Proportional control representation of the linearized LuGre Model

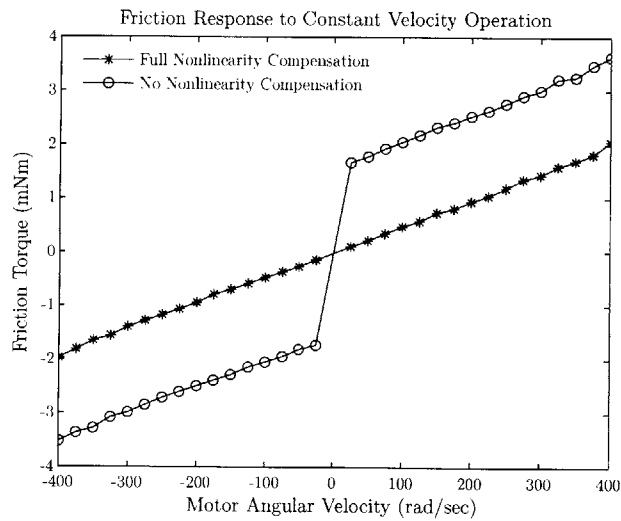
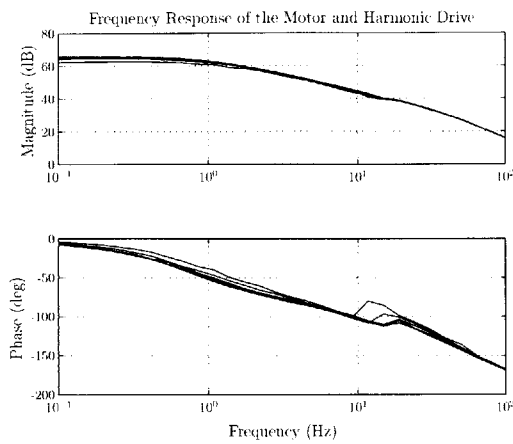
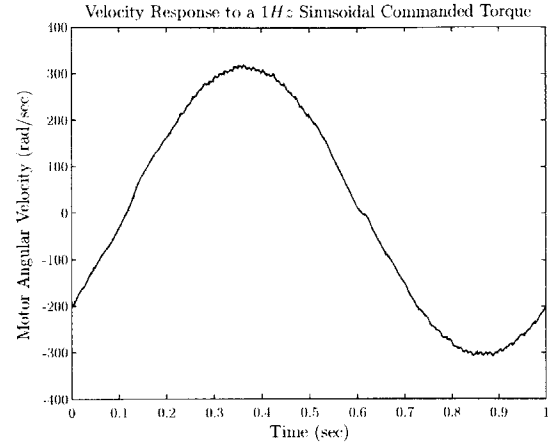


Figure 3-21: Plot of friction torque vs velocity. The plot shows the large jump in friction force due to stiction. Once the feedforward compensation scheme is implemented the friction torque appears to behave linearly to the command signal.



(a) Open loop frequency response of the motor with nonlinearity compensation.



(b) Time domain response of the motor with nonlinearity compensation to a sinusoidal input.

Figure 3-22: Plots of the motor's velocity response to commanded current with the nonlinearity compensation scheme implemented. In both the bode plot (a) and the time response to a sinusoid (b) the system responds linearly to the commanded current.

Once the feedforward compensation terms were applied a bode plot of the motor and harmonic was measured and is given in Fig. 3-22a. Also the time domain response to a sinusoidal command at 1 rad/s is shown in Fig. 3-22b. It can be clearly seen that the nonlinearities have been largely suppressed leaving a system that, for the most part, behaves linearly. With the feedforward compensation scheme in place the linear mass damper model given in Eq. 3.22 can be used.

3.5 System Model

In this section a general model for the entire system will be developed. First, the motor inertia and damping are combined with the elastic element and transmission to complete the model of the series elastic actuator. Then a general robotic model of the actuator and its load will be presented. Next, realistic loading conditions under which series elasticity can be exploited for improved efficiency are discussed and the general model is reduced to a few simplified loading conditions that accentuate this point. Finally, the frequency responses of the simplified models are compared with those of the actual hardware to confirm the validity of the model.

3.5.1 Series Elastic Actuator Model

The model of an electromagnetic linear Series Elastic Actuator is shown in Fig. 3-23 and is described analytically by Eq. 3.29. It consists of a motor acting as a torque source connected to a mass and damper, a transmission made up of the timing belt and the harmonic gear drive and an elastic element which is provided by the combination of a spring shaft and the transmission compliance.

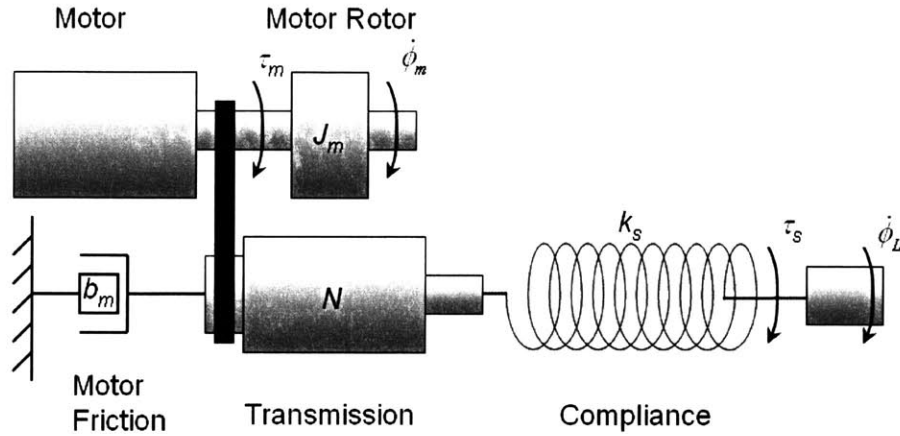


Figure 3-23: Series Elastic Actuator Model

$J_m (\frac{kgm^2}{rad})$	$b_m (\frac{kgm^2}{s-rad})$	N	$k_s (Nm/rad)$
$8.36e^{-7}$	$6e^{-6}$	230	10

Table 3.4: Series Elastic Actuator Parameters

The model coefficients were determined by measuring these elements and are given in Table 3.4. By fitting the linear motor model given in Eq. 3.23 to the bode plot in Fig. 3-22a the rotor inertia (J_m) and damping coefficient (b_m) were found. The value for the rotor inertia agrees with the value predicted by the CAD model and the value for the motor damping matches that obtained from the friction characterization in Figure 3-21, adding validity to the measured coefficients. The transmission ratio was measured by running the motor at constant speed and recording the output speed, and was found to be the predicted combination of the belt transmission and that of the harmonic gear drive. The stiffness of the system was found by locking the motor and loading the output of the spring shaft. Stiffness of the spring shaft was then distinguished from the stiffness of the transmission by locking a test transmission with epoxy and loading the spring shaft. It was found that the transmission added very little compliance, and thus the system compliance used in the model became that of the spring shaft. A plot of the spring stiffness (k_s) is shown in Fig. 3-24. It shows that the spring behaves linearly up to 2Nm where the stiffness begins to increase due to helical windup of the spring.

$$\begin{bmatrix} \ddot{\phi}_m \\ \dot{\tau}_s \end{bmatrix} = \begin{bmatrix} -\frac{b_m}{J_m} & -\frac{1}{NJ_m} \\ \frac{k_s}{N} & 0 \end{bmatrix} \begin{bmatrix} \dot{\phi}_m \\ \tau_s \end{bmatrix} + \begin{bmatrix} \frac{1}{J_m} & 0 \\ 0 & -k_s \end{bmatrix} \begin{bmatrix} \dot{\tau}_m \\ \dot{\phi}_L \end{bmatrix} \quad (3.29)$$

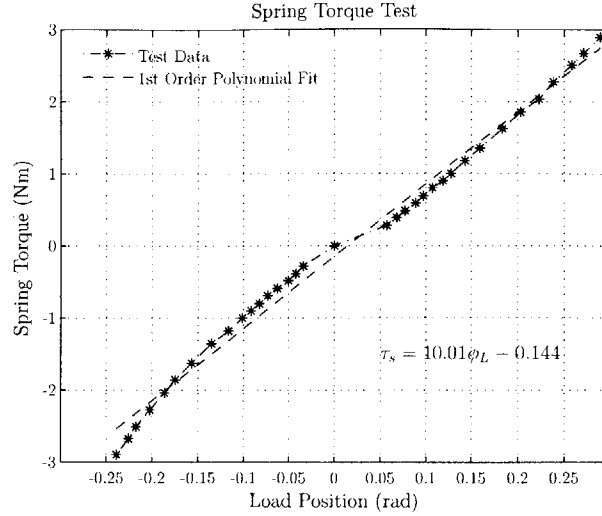


Figure 3-24: Plot of Spring Stiffness

3.5.2 General Robotic Loading

Series Elastic Actuators were designed for and are most commonly used in single or multi-link robotic manipulators. Generally these manipulators are in the form of arms or legs on biomimetic robots. They have also been used in serpentine robots, such as the HISS robot, where the multi-link manipulator makes up the entirety of the vehicle. The general model of a multi-link robotic manipulator is given below in Eq. 3.30.

$$H(\bar{\phi})\ddot{\bar{\phi}} + C(\dot{\bar{\phi}}, \bar{\phi}) + B\dot{\bar{\phi}} + E(\ddot{\bar{\phi}}, \dot{\bar{\phi}}, \bar{\phi}) = \bar{\tau}_{act} \quad (3.30)$$

Where $\bar{\tau}_{act}$ is the torque supplied by the joint actuator. $\bar{\phi}$, $\dot{\bar{\phi}}$ and $\ddot{\bar{\phi}}$ are $1 \times n$ matrices of the joint orientations (angle, angular velocity and angular acceleration), n being the number of links of the manipulator. $H(\bar{\phi})$ is the inertia matrix, $C(\dot{\bar{\phi}}, \bar{\phi})$ is the coriolis torques, B is the damping matrix and $E(\ddot{\bar{\phi}}, \dot{\bar{\phi}}, \bar{\phi})$ is the torques produced by environmental interactions. Combining the torque model of a generic multi-link robotic system with the model of a series elastic actuator gives the entire system model given in Eq. 3.31.

$$\begin{aligned}
 J_m \ddot{\bar{\phi}}_m + b_m \dot{\bar{\phi}}_m + \frac{1}{N} \bar{\tau}_s &= \bar{\tau}_m \\
 H(\bar{\phi}_L) \ddot{\bar{\phi}}_L + C(\dot{\bar{\phi}}_L, \bar{\phi}_L) + B \dot{\bar{\phi}}_L + E(\ddot{\bar{\phi}}_L, \dot{\bar{\phi}}_L, \bar{\phi}_L) &= \bar{\tau}_s \\
 k_s \left(\frac{1}{N} \bar{\phi}_m - \bar{\phi}_L \right) &= \bar{\tau}_s
 \end{aligned} \quad (3.31)$$

Eq. 3.31 in the multi-link case represents the loading configuration in a complex nonlinear equation that is difficult to use to analytically characterize actuator performance. It has been shown, however, that the organisms mimicked by biomimetic robots use the natural dynamics of their multi-link configurations to gain efficiency in locomotory movements (see Section 2.3). In

light of the complicated nature of the multi-link model, the simplified case of a single-link robot will be used in this thesis to investigate the conditions under which series elasticity can be used to enhance performance, in the hope that the insights gained can be used as a starting point for more complicated analysis.

In the case of the single link model Eq. 3.31 simplifies to Eq. 3.32 given below.

$$\begin{aligned}
J_m \ddot{\phi}_m + b_m \dot{\phi}_m + \frac{1}{N} \tau_s &= \tau_m \\
J_L \ddot{\phi}_L + b_L \dot{\phi}_L + E(\ddot{\phi}_L, \dot{\phi}_L, \phi_L) &= \tau_s \\
k_s (\frac{1}{N} \phi_m - \phi_L) &= \tau_s
\end{aligned} \tag{3.32}$$

Where the inertia matrix simplifies to the link inertia and the damping matrix simplifies to the link damping. Coriolis effects do not exist in the single link case and have been dropped, leaving the simplified environmental interactions $E(\phi, \dot{\phi}, \ddot{\phi})$ as the only nonlinear term. It is the contention of this thesis that the exploitation of natural dynamics to obtain efficiency gains is most effective during steady-state operation, therefore the interaction forces are simplified to loading conditions that simulate constant velocity movement. Two cases of loading are considered. Case 1: The environment enacts a purely frictional loading on the link. Case 2: The more realistic loading case where a nonlinear inertial loading term is used to represent the flight and contact phases present during terrestrial locomotion.

Case 1: Friction Load

A purely frictional load is created by two metal rods pressed up against the load plate. This setup creates a nonlinear form of friction called coulomb friction in which a constant force is created in the opposite direction of the load movement. Although nonlinear, this frictional load is considered somewhat of an ideal case because the loading is always in phase with the motion of the link and maximum power can be transferred to the load. Although it is not accurate for most patterns of locomotion, it comes very close for those that always maintain ground contact such as serpentine sidewarding, or in the case of machines a piston/crankshaft connected to a wheel. Nevertheless, the purely friction load sheds light on conditions for efficient actuation that can be applied to the more realistic case.

Under this case the environmental interaction term is simplified to:

$$E(\dot{\phi}_L) = \tau_{f,E} \left(\text{sign}(\dot{\phi}_L) \right) \tag{3.33}$$

Where $\tau_{f,E}$ is the environmental friction force. Substituting Eq. 3.33 into Eq. 3.32 gives the complete linear model.

$$\begin{aligned}
J_m \ddot{\phi}_m + b_m \dot{\phi}_m + \frac{1}{N} \tau_s &= \tau_m \\
J_L \ddot{\phi}_L + b_L \dot{\phi}_L + \tau_{f,E} \left(\text{sign}(\dot{\phi}_L) \right) &= \tau_s \\
k_s \left(\frac{1}{N} \phi_m - \phi_L \right) &= \tau_s
\end{aligned} \tag{3.34}$$

Case 2: Nonlinear Inertial Loading

In order to simulate more realistic robotic loading conditions, periodic ground contacts were added to the friction load of Case 1. The ground contact was achieved by hanging a weight off of the load plate and providing just enough cord so that the weight was barely in contact with the ground when the load position was at zero. The friction load from Case 1 was kept to ensure that power was being output by the actuator while the weight added non-linear inertial dynamics to the loading upon each ground contact.

3.5.3 Frequency Response

By substituting zero in for $E(\ddot{\phi}_L, \dot{\phi}_L, \phi_L)$ representing an unloaded system, the model given in Eq. 3.32 gives the following transfer functions in the Laplace Domain: Motor position from Motor Torque ($G_{p,mv}$), Link position from Motor Torque ($G_{p,lv}$) and Spring Force from Motor Torque ($G_{p,f}$) given in Eqs. 3.35, 3.36 and 3.37.

$$G_{p,mv}(s) = \frac{k_t(J_L s^2 + b_L s + k_s)}{J_m J_L s^3 + (b_m J_L + b_L J_m) s^2 + (b_m b_L + k_s J_{eq}) s + k_s b_{eq}} \tag{3.35}$$

$$G_{p,lv}(s) = \frac{k_t k_s / N}{J_m J_L s^3 + (b_m J_L + b_L J_m) s^2 + (b_m b_L + k_s J_{eq}) s + k_s b_{eq}} \tag{3.36}$$

$$G_{p,f}(s) = \frac{\frac{k_t k_s}{N} (J_L s + b_L)}{J_m J_L s^3 + (b_m J_L + b_L J_m) s^2 + (b_m b_L + k_s J_{eq}) s + k_s b_{eq}} \tag{3.37}$$

$$b_{eq} = b_m + b_L / N^2 \quad J_{eq} = J_m + J_L / N^2$$

The frequency response of the unloaded hardware was taken and compared with that of the system model in Figures 3-25, 3-26 and 3-27. As can be seen from the plots the simulation results correspond quite well to the hardware response verifying the system model developed in this section.

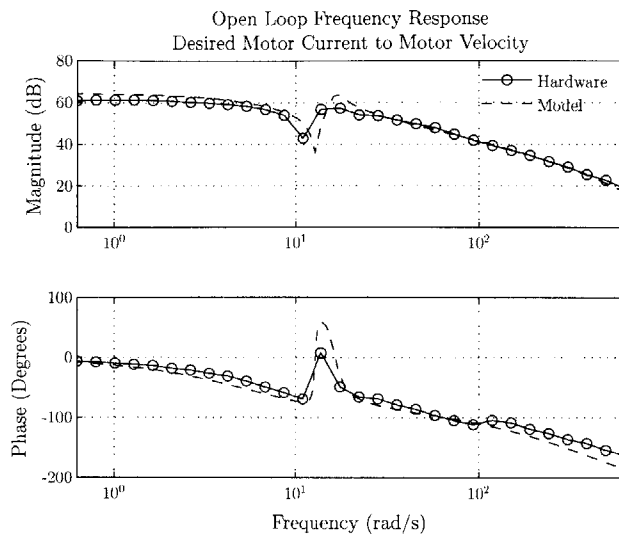


Figure 3-25: Frequency response of motor velocity from motor torque.

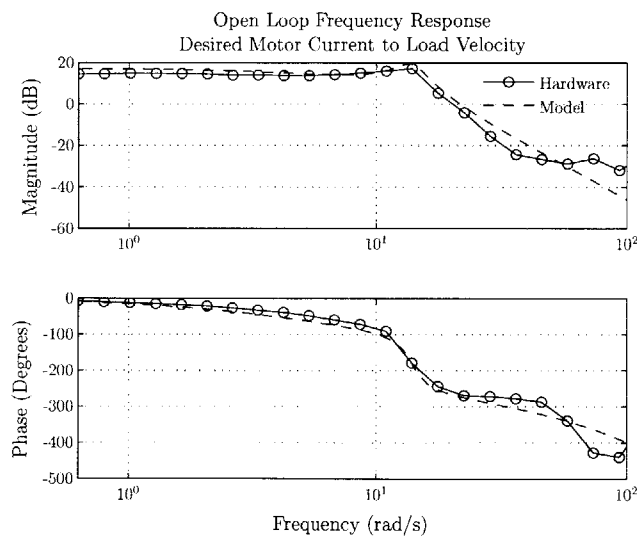


Figure 3-26: Frequency response of load velocity from motor torque.

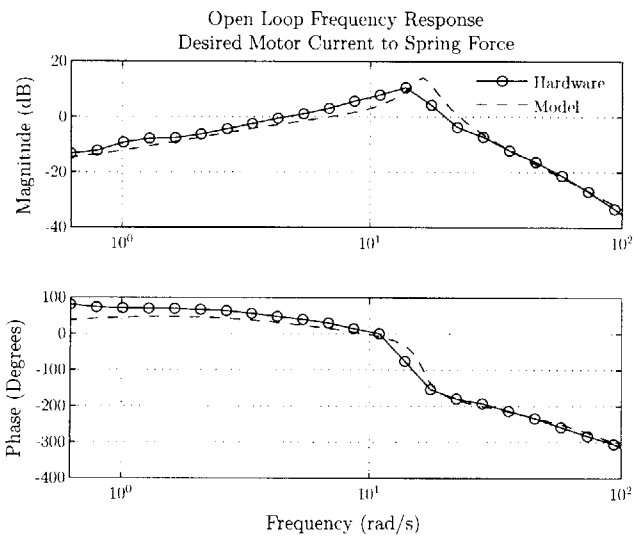


Figure 3-27: Frequency response of spring torque from motor torque.

Chapter 4

Control

In this chapter the control strategy used to investigate the performance of the actuator is developed. Just as if the actuator was being placed in a biomimetic robotic system, certain control requirements must be achieved. The control scheme must react to high loading conditions to limit the force in the spring and protect the gear train. In order to achieve efficient actuation the controller must be able to operate at the resonant frequency of the system. Finally, the controller must be robust to changes in the load inertia that may be present on a real vehicle due to changes in the manipulator's configuration or interactions with the environment. The control strategy developed to achieve these requirements is made up of a number of control stages. The design and implementation of these stages are described in the subsequent sections. Section 4.1 describes the motor position control loop. Section 4.2 derives a law that achieves accurate force control in the elastic element. In section 4.3 the load position control loop is designed. Control issues including sensor noise, control bandwidth and stability issues are discussed in section 4.4. Adaptive feedforward cancellation is added in section 4.5. Finally, the control scheme's overall performance is demonstrated by data taken in a few representative experiments in section 4.6.

4.1 Motor Position Control

One of the benefits of Series Elastic Actuation is that the addition of the compliance changes force control, a problem which geared motors are poor at handling, to a position control problem which geared motors are well suited. This section develops a motor position control loop that is used as the foundation for active force control. The frequency response of motor position from command current is given below:

$$G_{p,mp}(s) = \frac{k_t(J_L s^2 + b_L s + k_s)}{s(J_m J_L s^3 + (b_m J_L + b_L J_m)s^2 + (b_m b_L + k_s J_{eq})s + k_s b_{eq})} \quad (4.1)$$

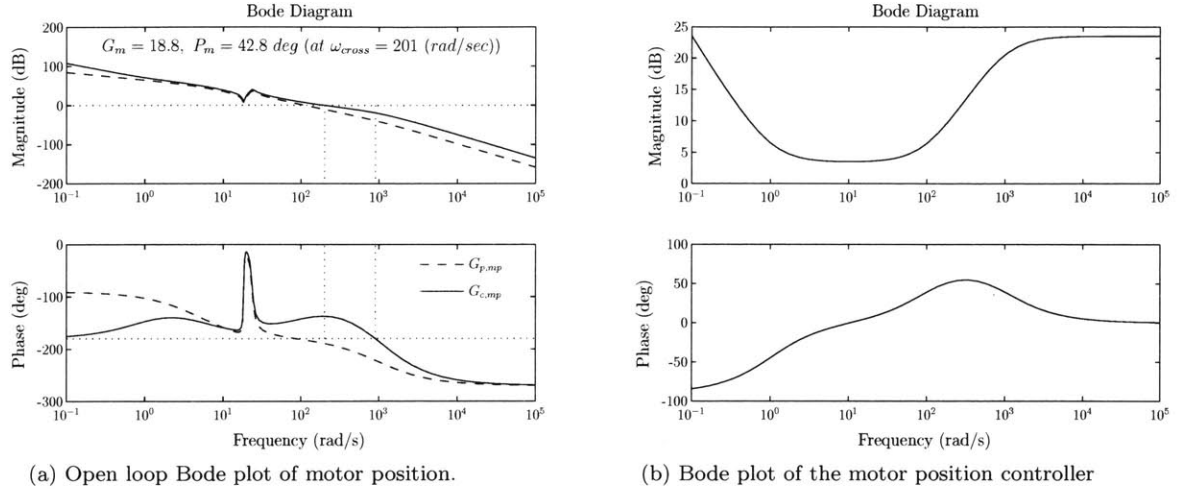


Figure 4-1: Motor Position Control

Fig. 4-1a shows the frequency response of the unloaded actuator from motor torque to motor position. The motor position response exhibits a resonant peak at $\omega_{system} = 23.4 \frac{rad}{s}$, due to the dynamic coupling between the load inertia and the motor inertia through the spring, this is referred to as the system resonance throughout this thesis. Figure 4-1a also shows a trough at $\omega_{load} = 16.9 \frac{rad}{s}$, due to the coupling between just the load inertia and the spring, this is referred to as the load resonance throughout this thesis. The trough is located in the vicinity of the peak if the load inertia is small compared to the motor inertia, causing the trough and the peak to partially cancel each other. This is generally the case with series elastic actuators because it is the large reflected motor inertia that created the need for the spring in the first place. Due to the closeness of the load resonance and the system resonance, there is only a small deviation between the motor position response of a rigid system and that of the current hardware. This is illustrated in Fig. 4-2. As a result, standard motor control techniques can be used despite the presence of the spring.

A requirement for the load position controller was that it be able to operate with a bandwidth above the system's efficient frequency. In order to achieve this, the inner force control loop and subsequently the motor position control loop were designed to operate at a bandwidth one decade above that of the outer loop. With the efficient frequency at ω_{load} , a bandwidth of $\omega_{lp} = 20 \frac{rad}{s}$ was chosen for the outer loop and a bandwidth of $\omega_{mp} = 200 \frac{rad}{s}$ was chosen for the motor position loop. A PID controller, consisting of a pole at the origin and two zeros, was used in the motor position loop to achieve this bandwidth. The zeros were placed at $\omega_{Z1,mp} = 1 \frac{rad}{s}$ and $\omega_{Z2} = 100 \frac{rad}{s}$ in order to achieve a phase margin of 45 degrees at ω_{mp} . A controller gain of $K_{c,mp} = 1.5$ then achieved an open loop unity gain crossover at the desired bandwidth. The transfer function for the motor position controller is given in Eq. 4.2 with its parameter values given in Table 4.1 and its response is shown in Fig. 4-1b.

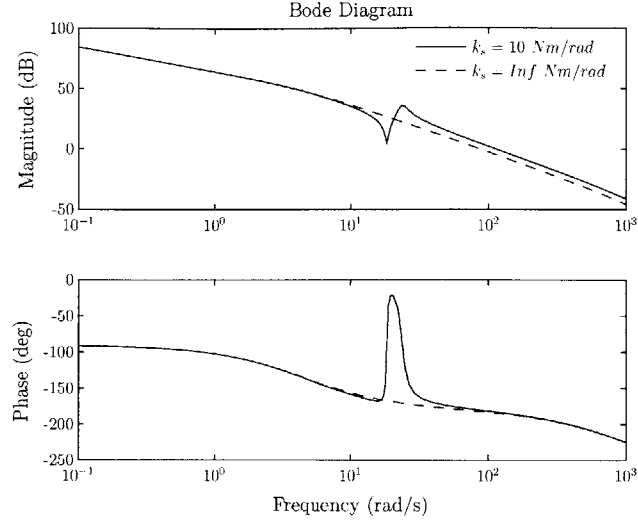


Figure 4-2: Bode response comparing an elastic actuator to one which has the spring shaft replaced by a solid shaft.

$$G_{c,mp} = K_{c,mp} \frac{K_{d,mp}s^2 + K_{p,mp}s + K_{I,mp}}{(K_{f,mp}s + 1)s} \quad (4.2)$$

$K_{c,mp}$	$K_{d,mp}$	$K_{p,mp}$	$K_{I,mp}$
1.5	0.01	1	1

Table 4.1: Motor Position Controller Parameters

Fig. 4-3 shows the closed loop motor position response of the implemented controller compared with the theoretical closed loop response predicted by the model. As can be seen from the plot the model corresponds nicely to the measured data. The relationship between the desired motor position and the actual motor position shown in Figure 4-3 is described by the term G_{mp} as follows.

$$\frac{\phi_m}{\phi_{m,d}} = G_{mp}(s) \quad (4.3)$$

4.2 Force Control

4.2.1 Spring Compensation Law

The torque in the spring is defined as the difference between the load position and the motor position scaled by the transmission.

$$\tau_s = k_s(\phi_m/N - \phi_L) \quad (4.4)$$

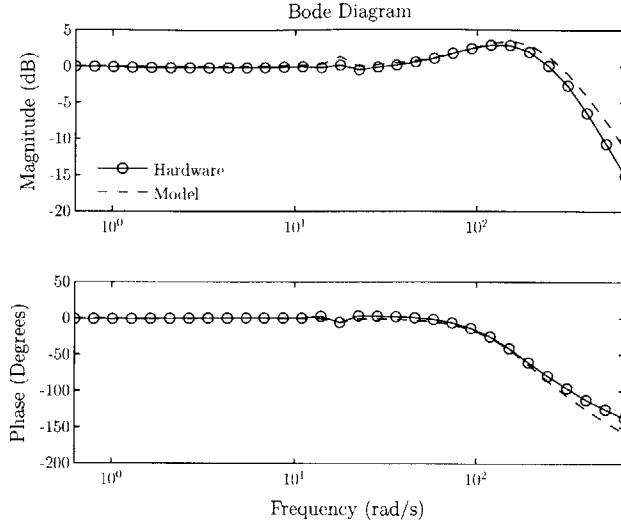


Figure 4-3: Frequency Response of Closed Loop Motor Position Control. The plot shows the response of motor position from the desired motor position command.

In order to achieve force control, a control law is chosen that defines the motor position necessary to maintain the desired spring torque. Solving Eq. 4.4 for motor position results in the appropriate law.

$$\phi_{m,d} = \frac{N}{k_s} \tau_{s,d} + N \phi_{L,meas} \quad (4.5)$$

Where $\phi_{m,d}$ is the desired motor position, $\tau_{s,d}$ is the desired spring torque and $\phi_{L,meas}$ is the measured load position.

This force control law can be broken into two parts, a spring compensation term $N\phi_L$ and a desired force term $\frac{N}{k_s}\tau_{s,d}$. The spring compensation term is solely based on load position and defines the position the motor must achieve to guarantee zero force in the spring. It, in effect, decouples the load inertia from the motor inertia thus suppressing the complicated dynamics associated with resonance.

The load dynamics in terms of motor position and load disturbance torque is given by:

$$J_L \ddot{\phi}_L + b_L \dot{\phi}_L + k_s \phi_L = \tau_d + \frac{k_s}{N} \phi_m \quad (4.6)$$

In the ideal system infinite bandwidth, perfect sensing and therefore perfect tracking is achieved by the motor position law, an assumption that is not reasonable in the real world but is useful in that it illustrates the decoupling effect of the spring compensation term. The control law given in Eq. 4.5 is now substituted in to Eq. 4.6 under the ideal assumption that $\phi_m = \phi_{m,d}$ and $\phi_{L,meas} = \phi_L$ resulting in a relation for load position in terms of the desired spring torque and the load disturbance torque.

$$J_L \ddot{\phi}_L + b_L \dot{\phi}_L = \tau_d + \tau_{s,d} \quad (4.7)$$

It can be seen that the spring compensation term of the force control law cancelled the spring force that results from the load dynamics thus transforming the system into a simple mass damper composed of the load inertia and load damping.

4.2.2 Closed Loop Force Control

Although the ideal system is useful to illustrate the concept of spring compensation it is not reasonable to use as a system model because it does not illustrate any of the limitations that are inherent to active force control. These limitations are best investigated by breaking the operating conditions of the actuator into two main categories. The first is fixed load operation, where the load inertia is constrained somehow, as can be the case during interactions with the environment. The second category is operation during load motion, where the load is in free space and the load inertia is that of the link plus a possible added inertia due to the robot's task.

A model of the actuator under closed loop force control is now derived in order to investigate the two operating conditions. Moving Eqs. 4.4 and 4.5 into the Laplace domain gives:

$$\phi_{m,d}(s) = \frac{N}{k_s} \tau_{s,d}(s) + N \phi_{L,meas}(s) \quad (4.8)$$

$$\tau_s(s) = k_s(\phi_m(s)/N - \phi_L(s)) \quad (4.9)$$

Then substituting Eq. 4.8 and Eq. 4.3 into Eq. 4.9 yields the relation for spring torque in terms of the desired spring torque, the load position and the measured load position.

$$\tau_s(s) = G_{mp}(s) \tau_{s,d}(s) + k_s(G_{mp}(s) \phi_{L,meas}(s) - \phi_L(s)) \quad (4.10)$$

The load position sensor introduces a significant amount of noise and is filtered as explained in Section 3.1.4. This introduces dynamics between the measured load position and the actual load position:

$$\phi_{L,meas}(s) = G_{f,lp}(s) \phi_L(s) \quad (4.11)$$

where $G_{f,lp}$ represents a sixth order Bessel filter with a cutoff frequency at $\omega_{f,lp} = 200 \frac{rad}{s}$. Substituting Eq. 4.11 into Eq 4.10 gives the spring torque in terms of the desired torque and the load position.

$$\tau_s(s) = G_{mp}(s)\tau_{s,d}(s) + ks(G_{mp}(s)G_{f,lp}(s) - 1)\phi_L(s) \quad (4.12)$$

Fixed Load Operation

Operation when the load is fixed is the most pertinent condition for active force control. It provides the conditions under which position control and rigid actuation are not compatible with dynamic constraints and is the motivation behind series elastic actuation. Accurate force control is important in this case to prevent large spikes in force that could damage either the robot itself or the objects that the robot is interacting with.

During fixed load operation ϕ_L goes to zero and Eq. 4.12 simplifies to:

$$\tau_s(s) = G_{mp}\tau_{s,d} \quad (4.13)$$

The developed model in Eq. 4.13 states that the limitation on force control during fixed load operation is the bandwidth of the motor position controller. The closed loop motor position response in Figure 4-3 is then also the response for fixed load force control, thus good force control is achieved.

Dynamic Load Operation

During operation when the load is allowed to move, the requirements on the force control law are not as rigid as in the fixed load case. There are two major requirements that must be met by the force control scheme if acceptable actuator performance is to be attained. First and foremost, just as in the fixed load case, accurate force control at frequencies around the system resonance must be obtained if that resonance is to be suppressed. After that, during load motion the purpose of force control becomes the manipulation of the load and thus accurate force control is only necessary in the range of frequencies present in transients associated with load movement.

In the case of a dynamic load ϕ_L does not go to zero and the second term in Eq. 4.12 is able to have a significant impact on the closed loop force control. The relation for load motion in terms of the spring torque is represented by a mass damper model similar to the motor.

$$J_L\ddot{\phi}_L + b_L\dot{\phi}_L = \tau_s \quad (4.14)$$

Which in the Laplace domain is given by:

$$\frac{\phi_L(s)}{\tau_s(s)} = \frac{1}{(J_Ls + b_L)s} \quad (4.15)$$

Substituting Eq. 4.15 into Eq. 4.12 and solving for τ_s gives a model of the closed loop force control under dynamic loading conditions.

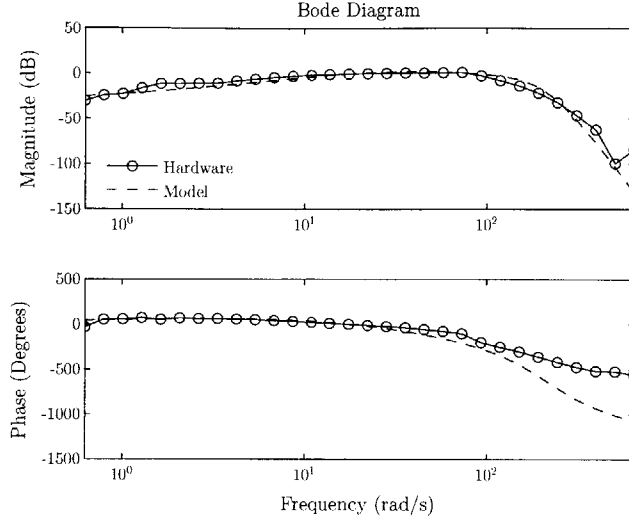


Figure 4-4: Bode plot of the closed loop force control. The plot gives the response of the spring torque from the desired spring torque. The Bode plot characterizes the measured spring torque with respect to the desired spring torque. The plot shows that good force control is achieved at frequencies between $1 - 100 \frac{rad}{s}$, which is an adequate range to achieve position control of a dynamic load.

$$G_f(s) = \frac{\tau_s(s)}{\tau_{s,d}(s)} = G_{mp}(s) \left(\frac{(J_L s + b_L)s}{J_L s^2 + b_L s + k_s(G_{mp}(s)G_{f,lp}(s) - 1)} \right) \quad (4.16)$$

The model in Eq. 4.16, when compared to experimental data in Fig. 4-4, agrees nicely with the hardware. The plot illustrates the dynamics added by the second term in Eq. 4.12 through the rolloff of magnitude present at low frequencies. This rolloff occurs because under dynamic load conditions, low frequency spring torque equates to low frequency acceleration of the load inertia. The lower the frequency range the closer the load acceleration is to a constant, thus resulting in large load velocities. At higher load velocities, however, a delay in the measured load position is introduced by the load position filter, thus the motor position commanded by the force control law is no longer the correct value to achieve the desired spring torque.

In order to determine if this force control scheme is adequate, the requirements for good system performance given at the beginning of this section must be checked. The resonant frequency of the system is at $23.3 \frac{rad}{s}$ falling within the range of good force control, therefore the system resonance will be suppressed and the first requirement is satisfied.

In order to check the second requirement, the model of the system from spring torque to load position is used to determine the range of frequencies required to achieve load manipulation. Fig. 4-5 shows a typical torque control signal from the model in Eq. 4.7. The model parameters were set to the same values as the load inertia and damping measured in section 3.5.1. Position control of the model was realized with a PID controller configured to a bandwidth of $20 \frac{rad}{s}$, just above the

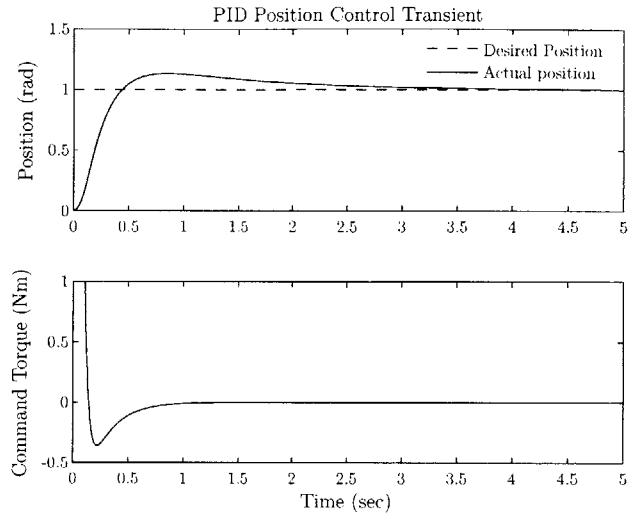


Figure 4-5: Transient response of a mass/damper system under PID position control to a step input.

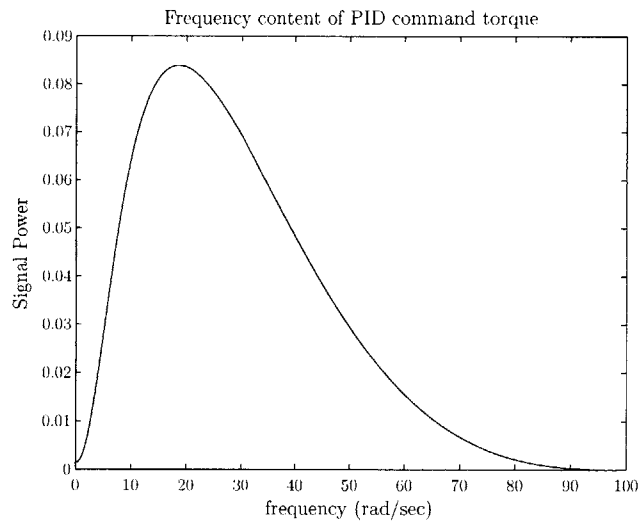


Figure 4-6: Frequency composition of a PID position controller's torque command during a step in position. The plot shows that during load movements it is not necessary to have accurate force control at low frequencies.

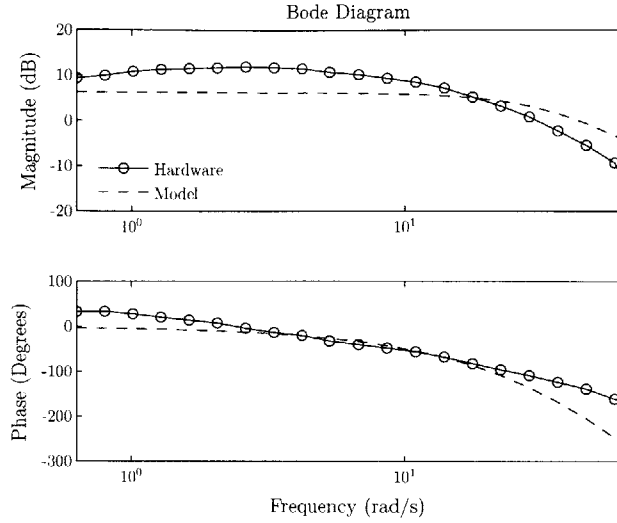


Figure 4-7: Frequency Response from desired spring torque to load velocity.

load resonance. The torque signal in Fig. 4-5 is the result of a step in desired position on the input. Figure 4-6 gives the FFT of the torque signal. It shows that the majority of the information in the torque signal lies in the frequency range from $3\frac{rad}{s}$ – $60\frac{rad}{s}$. The force control scheme is effective in this range therefore the second requirement is satisfied and good actuator performance can be achieved during load movement.

4.3 Load Position Control

In order to manipulate the load, a PID load position controller such as the one referred to in the last section was designed and implemented. In the last section the ideal model was used for the controller design. This model is not sufficient because it neglects the limitations of the force control scheme. Substituting Eq. 4.15 into Eq. 4.16 and solving gives the transfer function from the desired spring torque to the load position.

$$G_{sfc,lp}(s) = \frac{\phi_L(s)}{\tau_{s,d}(s)} = G_{mp}(s) \left(\frac{1}{J_L s^2 + b_L s + k_s (G_{mp}(s) G_{f,lp}(s) - 1)} \right) \quad (4.17)$$

Differentiating this equation, which in the Laplace domain is equivalent to multiplying by s , changes load position to load velocity.

$$G_{sfc,lv}(s) = \frac{\phi_L(s)}{\tau_{s,d}(s)} = G_{mp}(s) \left(\frac{1}{J_L s + b_L + k_s \frac{G_{mp}(s) G_{f,lp}(s) - 1}{s}} \right) \quad (4.18)$$

The frequency response of Eq. 4.18 is given in Fig. 4-7. Viewing the relation of load velocity to desired spring torque as opposed to load position to desired spring torque makes it easy to see the

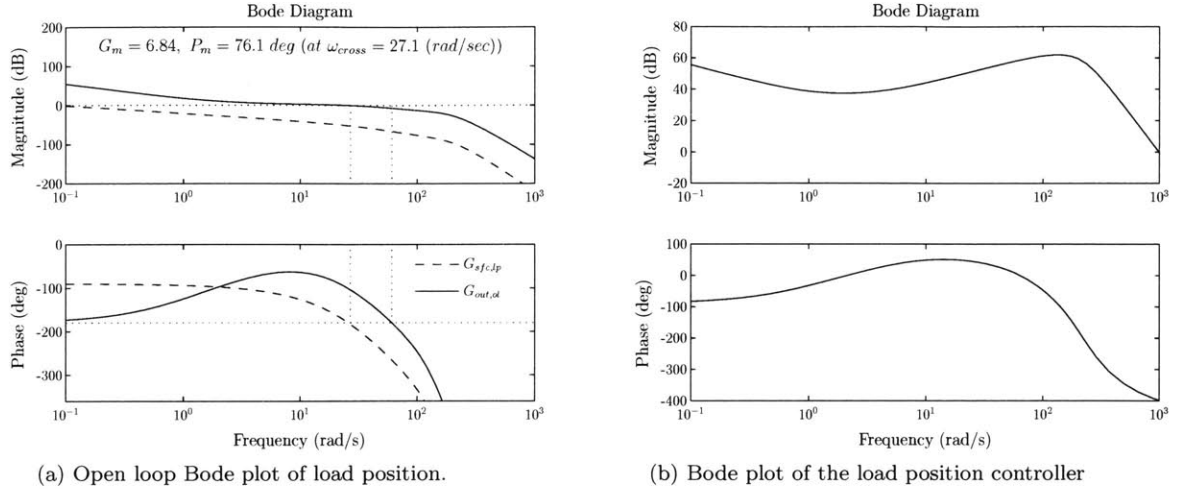


Figure 4-8: Load Position Control

location of the pole created by the interaction between the load inertia and damping. When fit with the ideal model in Eq. 4.7 the load inertia and damping coefficients are found to be $J_L = 0.0305 \frac{kg \cdot m^2}{rad}$ and $b_L = 0.4865 \frac{Nm \cdot s}{rad}$ respectively. The inertia value matches the model of the hardware, however, the damping coefficient is much higher than what was previously measured on the hardware. This discrepancy is due to the force control limitations. The delay introduced by the load position filter creates a force that is linearly coupled to load velocity. This delay manifests itself as an additional damping term causing the perceived damping of the load to be much higher than that of the actual hardware.

The load position controller's design process was identical to that of the motor position controller due to the likeness of the two models. As stated earlier a controller bandwidth above the system's efficient frequency at $16.9 \frac{rad}{s}$ was required to investigate the efficiency gains possible using series elastic actuators. Zeros were placed at $\omega_{Z1,lp} = 1 \frac{rad}{s}$ and $\omega_{Z2,lp} = 4 \frac{rad}{s}$ to ensure that there was adequate phase margin in the frequency range at and above resonance. The gain was then adjusted to achieve as high a bandwidth as possible. A final value of $K_{lp} = 60$ was settled on yielding a bandwidth of $27.1 \frac{rad}{s}$. The load position controller parameters are given in Table 4.2. The frequency response of the open loop system is shown in Fig 4-8a. It shows a phase margin of 74.6 degrees and a gain margin of 6.8 dB. A Bode plot of the load position compensator is given in Figure 4-8b. The closed loop response of the system under load position control is given in Fig 4-9.

$K_{c,lp}$	$K_{d,lp}$	$K_{p,lp}$	$K_{I,lp}$
60	0.25	1.25	1

Table 4.2: Load Position Controller Parameters

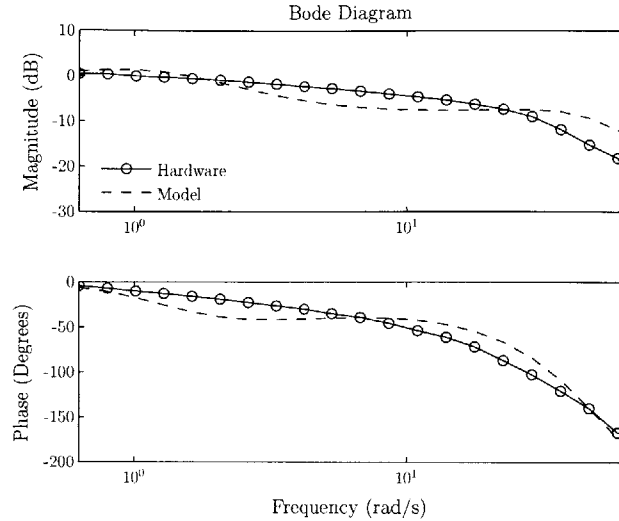


Figure 4-9: Frequency Response of Closed Loop load Position Control. The plot shows the response of load position from the desired load position command.

Part of the reason for the relatively low placement of the controller's two zeros was to ensure adequate phase margin at frequencies lower than the current systems resonant frequency. This precaution was taken so that the system could be robust to small changes in load inertia. Fig. 4-10 shows how the system's open loop response changes due to variations in the load. As can be seen from the plot the controller remains stable for both increases and decreases in the load inertia. Although stability is maintained upon small decreases in load inertia, the amount of decrease is limited before instability is a concern. This is acceptable as long as the controller is designed so that the load inertia corresponding to the robot link inertia results in good stability margins. In addition to stability, the controller maintains a bandwidth higher than the system resonance during load variations. This is due to the fact that as the load increases the natural frequency of the system drops at a higher rate than the controller bandwidth.

4.3.1 Shock Protection

One of the largest shortcomings of the hardware used in this thesis, which was experienced during the HISS project, was that there was not adequate protection for the delicate harmonic drives. Initially solid shafts were used and the harmonic drives were damaged so much that they could no longer support a third of their original torque rating. Spring shafts were introduced to alleviate the burden on the drives but due to the sensor problems described in section 3.1.4 only loose force control was implemented and the harmonic drives still sustained a great deal of damage. PID controllers such as the one used here were impossible due to the large spikes in force they called for during sudden movements. The improved force control scheme developed in the present work, however, allows active spring force saturation to be implemented to protect the harmonic drives. The addition of

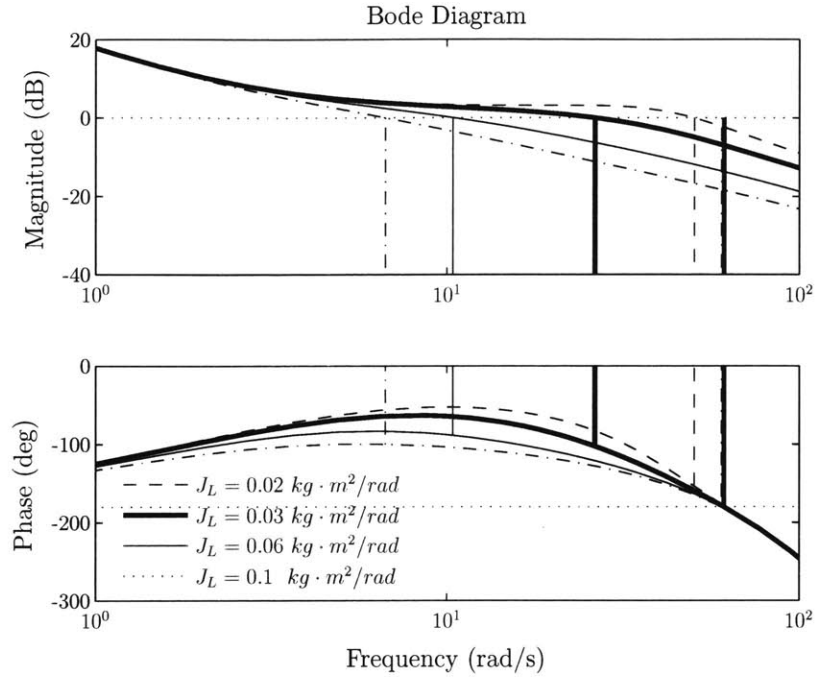


Figure 4-10: Load Position open loop stability margins upon changes in load inertia.

force saturation made the actuator tolerant to shock loads either created by the system or those enacted on the system by the environment.

4.4 Control Issues

There were a number of issues that turned up that limited the performance of the control. Three major problems called for constant attention and had a notable affect on the final design. They are sensor noise, vibration and stability and are described in this section.

4.4.1 Sensor Noise

In order to calculate the load position controller's damping term the load position is differentiated amplifying the sensor noise at higher frequencies. This noise is then amplified again by the controller gain and propagates through the force control law to the desired motor position signal. The motor then tracks any noise within the bandwidth of the motor controller causing the motor to chatter. Fig. 4-11 shows the noisy differential signal and the resulting motor movement. If too much noise is allowed to enter into the desired motor position term the chattering would become violent ultimately degrading the performance of the force control and therefore the load position control.

The bandwidth achieved by the load position control is directly related to the gain of the controller. Propagation of noise through the controller's differential term, however, limited the gain and

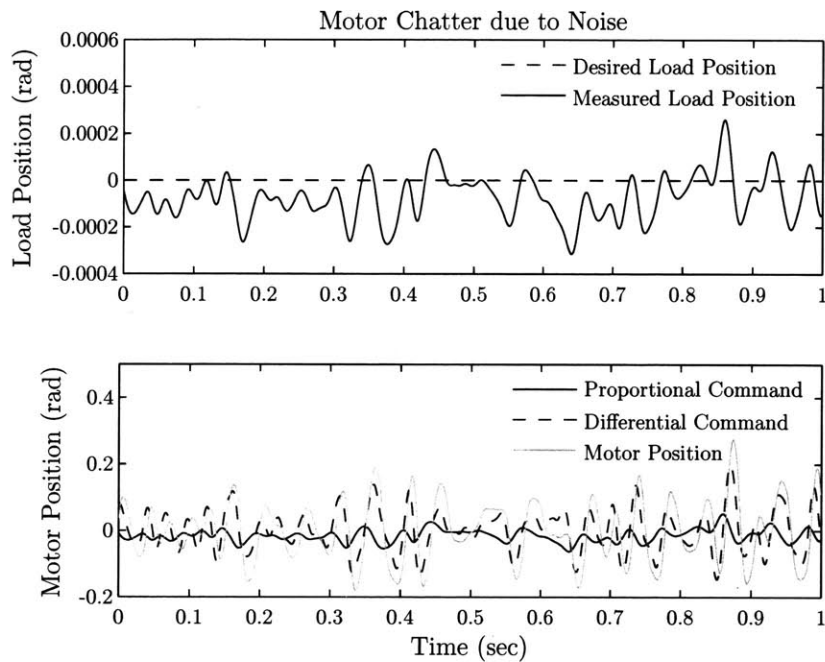


Figure 4-11: Motor Chatter due to noise under load position control. The load is for the most part not moving however the load position sensor is measuring a small amount of movement due to either vibrations or sensor noise (Top Plot). The load position controller then amplifies the load position error through three terms. The spring compensation term and the proportional control term are both proportional to load position and are shown in the bottom plot as the proportional command. The differential control term is shown as the differential command. The resulting motor position tracks these noisy command signals. This is what is referred to as motor chatter.

in turn limited the control bandwidth. In order to suppress the sensor noise and increase controller gain the load position signal was filtered as described in section 3.1.4. Unfortunately, the phase lag added by the filter threatened controller stability thus creating a tradeoff between noise suppression and controller gain. The final designs used for the noise filter and controller are the result of experimental tweaking in order to find a configuration that satisfies this tradeoff.

4.4.2 Vibration

Due to coupling between the load plate and the unique movement of the harmonic drive, large load vibrations out of the plane of interest were present during operation. The load plate used to simulate the link inertia of a robot was a $\frac{3}{4}$ inch thick 12 inch diameter cylindrical piece of aluminum, which interfaced with the harmonic drive through the spring shaft connected at its center. The spring shaft is supported by two bearings, one close to the load plate (the load bearing) and another at the other end of the shaft (the input bearing). The input bearing did not provide enough support for the size of the load plate and allowed radial deflections of the spring shaft. The special movement pattern characteristic to harmonic drives coupled with the stresses provided by the load plate excited radial vibrations of the spring shaft. The vibrations were in turn reflected through the coupling and auxiliary shaft, where they created small misalignments with the load sensor, and thus error in the position and spring torque measurements. It was also propagated through the control scheme as described in Section 4.4.1 eventually causing extra chatter in the motor signal. As load position control gains were increased the coupling between motor chatter and load vibration worsened to the point that limit cycles about the controlled load position occurred. This placed yet another constraint on controller gain and in turn bandwidth.

4.4.3 Stability

Stability of the force control loop was a major concern during controller design. The load position controller depended on stable force control to maintain good load position control. More importantly, the hardware depended on the force control loop to protect it under adverse loading conditions. If the force control loop were to go unstable the harmonic drive would be destroyed.

The issue of stable force control is really an issue of stable motor position control. The standard linear control methods used in Section 4.1 ensured motor position control stability for the hardware configuration used in the controller design. There were two cases not addressed by the standard linear method that were taken into consideration during the controller design. Case 1: Changing load inertia. Case 2: Motor current saturation.

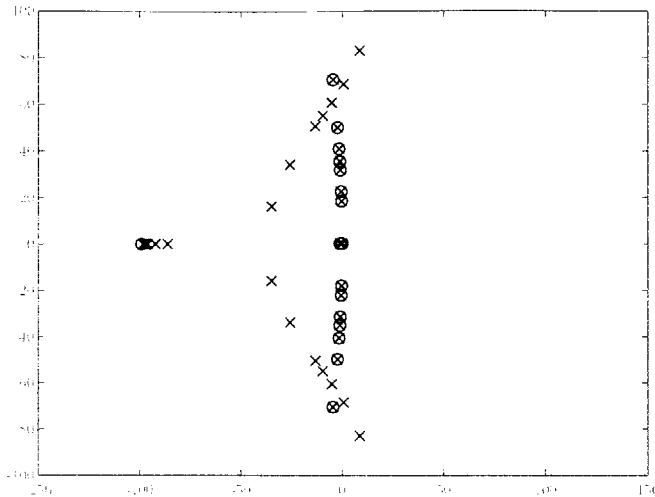


Figure 4-12: This plot shows the movement of the system poles under closed loop motor position control. As the load inertia is decreased the poles that correspond to the system resonance move into the right half plane where the system is unstable.

Changing Load Inertia

Figure 4-12 shows the movement of the systems poles under closed loop motor position control as the inertia is varied. As the inertia is decreased the conjugate pair of poles corresponding to the system resonance moves both away from the real axis and toward the right half plane. If the load inertia becomes small enough the poles enter the right half plane and the system becomes unstable. This makes sense because as the load inertia decreases the resonant frequency of the system increases. If the system resonant frequency is allowed to climb too high the motor position bandwidth will no longer be high enough to suppress the resonance. Just as is the case with the load position loop, the motor position loop requires a minimum load inertia (i.e. that of the link) to maintain stability.

Motor Current Saturation

Motor current saturation creates constraints on the region in the frequency domain in which the motor position responds linearly to commands. It was found that as long as the motor position movement required to suppress the system resonance was located in the linear region, stability was maintained.

Ignoring the spring and load for a moment to simplify the system, the motor dynamics is given by:

$$J_m \frac{d^2 \phi_m}{dt^2} + b_m \frac{d \phi_m}{dt} = \tau_{amp} \cos(\omega t) \quad (4.19)$$

Where τ_{amp} is the amplitude of the commanded motor torque. Then solving this differential equation for motor position yields:

$$\phi_m = \frac{\tau_{amp}}{\omega \sqrt{(J_m \omega)^2 + b_m^2}} \sin(\omega t - \psi) = \phi_{m,amp} \sin(\omega t - \psi) \quad (4.20)$$

If τ_{amp} is replaced with the saturation limit (τ_{sat}) the linear region for motor position is defined.

$$\phi_{m,sat} = \frac{\tau_{sat}/(b\omega_0)}{(\omega/\omega_0)\sqrt{(\omega/\omega_0)^2 + 1}} \quad (4.21)$$

$$\omega_0 = b_m/J_m$$

Eq. 4.21 represents the non-dimensionalized linear constraints on motor position based on motor torque saturation and in turn motor current saturation. Plotting these constraints (Figure 4-13) sheds light on the limitations of motor position linearity and helps to show the mechanisms that can be used to keep the motor operation in a linear region. Current saturation puts both a frequency limit and a magnitude limit on motor position linearity. Increasing the current saturation increases both of these limits. In order to maintain stability the system resonance must be at a low enough bandwidth and the magnitude limit must be high enough so that the required motor movement is in the linear range. This is done in two ways. First by limiting the system resonance to lower frequencies by using a minimum load inertia. Second by increasing the current limit to make sure saturation does not cause instability. It was found through simulation that using a current limit of 2Amps and a load inertia of $J_L = 0.015 \frac{kg \cdot m^2}{rad}$ put the system on the brink of instability. For the work in this thesis the current limit was set at 3Amps and the minimum load inertia use was $J_L = 0.03 \frac{kg \cdot m^2}{rad}$ ultimately resulting in a stable system.

4.5 Adaptive Feedforward Cancellation

Under no external loading conditions, commanding the load to follow a sinusoid at the resonant frequency with an amplitude of 0.1 radians resulted in a phase delay of $-71.4degrees$ and subsequently an error signal with a magnitude of $0.072rad$ (Figure 4-14). This tracking is poor enough that the control is inadequate to execute robotic gaits. The inability to accurately tack a desired load position is due to the limitation on controller gain caused by sensor noise and load vibrations. Due to the cyclic nature of the gait, however, the error caused can be decomposed into a set of harmonics of the commanded frequency. By using an adaptive feedforward cancellation (AFC) scheme as in [Trumper et al., 2005] the tracking error can be suppressed at each harmonic.

AFC works by placing a set of parallel resonators in a loop around the load position loop as shown in Fig. 4-15. Each resonator is designed to cancel a particular harmonic that is present in the error signal and is of the following form:

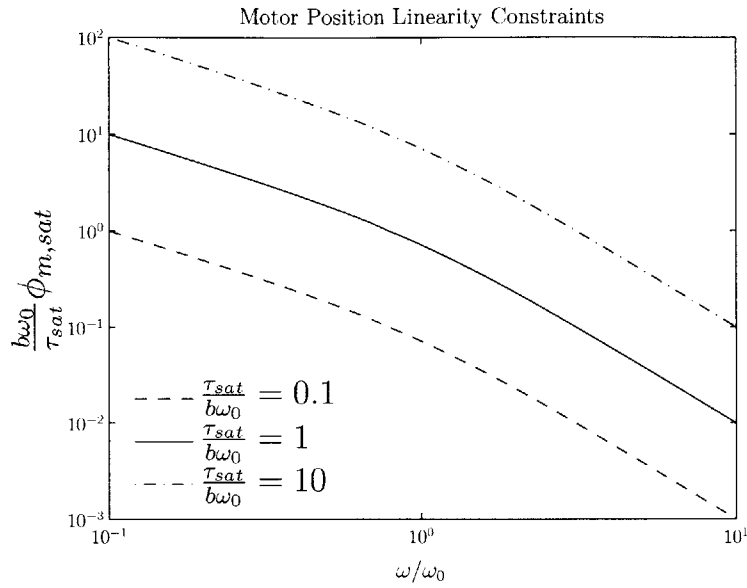


Figure 4-13: Non-Dimensional Motor Saturation Characteristic. This plot shows the region in which the motor can operate linearly due to the constraints set by motor current saturation.

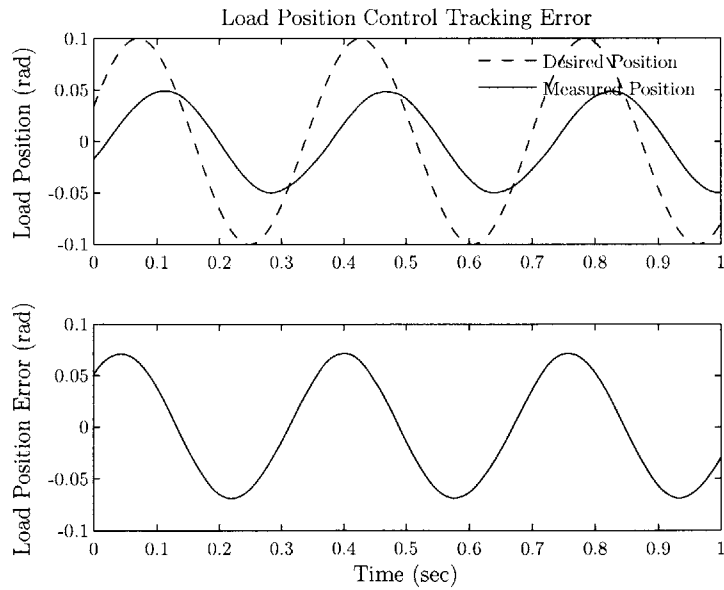


Figure 4-14: Tracking Error under Load Position Control. The system was commanded to follow a $0.1rad, 2.8Hz$ sinusoid. This plot shows the resulting tracking error.

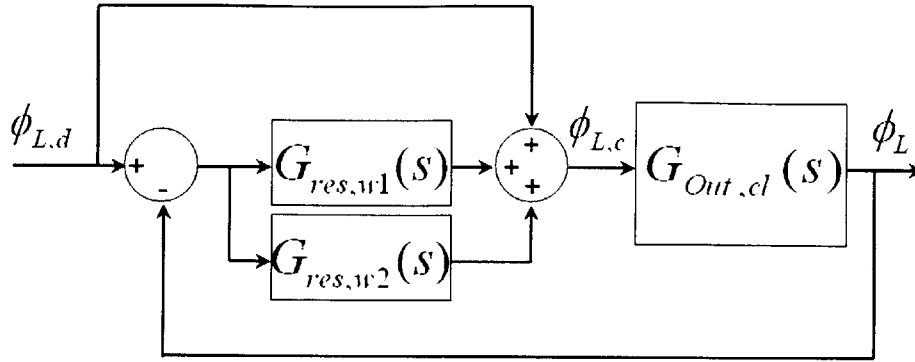


Figure 4-15: Block Diagram of the AFC Loop.

$$G_r(s) = g_n \frac{s \cos \phi_n + \sin \phi_n}{s^2 + \omega_n^2} \quad (4.22)$$

Where ω_n is the natural frequency of the resonator, ϕ_n is the phase offset term and g_n is the gain. In order to tune the resonators these three terms are adjusted. The result is that harmonics in the error signal excite the corresponding resonator producing an oscillatory signal that augments the load position command signal ($\phi_{L,c}$). The load position loop still exhibits its fundamental shortcomings, however, the addition of the AFC terms adjust $\phi_{L,c}$ in such a manner that the desired load position signal ($\phi_{L,d}$) is followed.

4.5.1 Resonator Tuning

In order to tune the resonators the three design parameters, ω_n , ϕ_n and g_n must be chosen. The frequency term of each resonator is chosen based on the harmonic composition of the error signal. The FFT of the error signal produced by the loaded actuator is given in Fig 4-16. It shows that the disturbance is mainly manifested in the error signal at the first two harmonics of the commanded frequency. AFC resonators are placed at these frequencies to compensate for the disturbance.

The phase terms and gain terms are then chosen to achieve sufficient phase and gain margins to ensure controller stability as is done in standard controller design. The literature shows that there is a discontinuity in phase at the natural frequency of the resonator centered on the phase parameter. The design process presented involves choosing the gain parameter so that the unity gain crossover for that resonator falls at approximately the natural frequency. The phase parameter is then chosen so that the entirety of the phase discontinuity is in a location that achieves good phase margin (i.e. $P_m > 45$ degrees). Due to the actuator's application to locomotion, the control design differs from that described by [Trumper et al., 2005] in that the AFC scheme will be designed to operate under

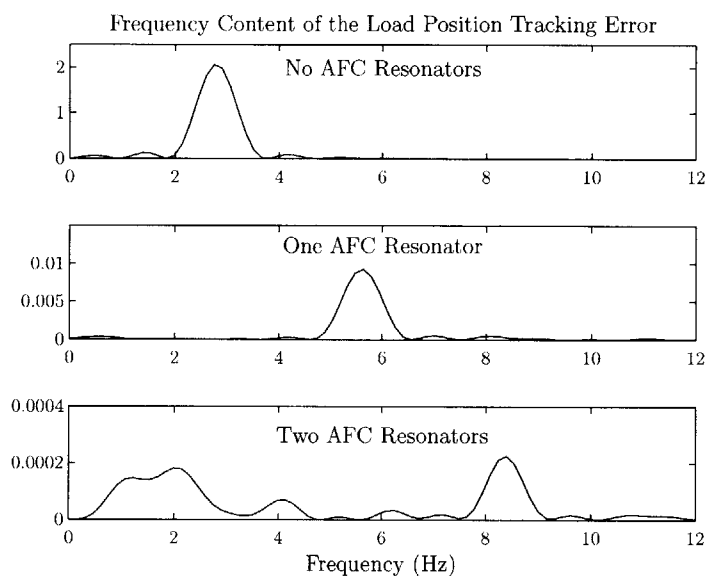


Figure 4-16: Frequency Content of the Tracking Error under Load Position Control. The system was commanded to follow a $0.1rad$, $2.8Hz$ sinusoid and is loaded with both linear damping and the nonlinear inertial ground contacts. The top plot shows that without the AFC loop closed the majority of the tracking error is localized at the commanded frequency. The second plot shows how after closing the AFC loop with a single resonator at the commanded frequency the remainder of the tracking error is localized at the second harmonic of the commanded frequency. Finally the bottom plot shows that with two resonators operating in the AFC loop most of the tracking error is suppressed with the remaining error on the order of the sensor noise.

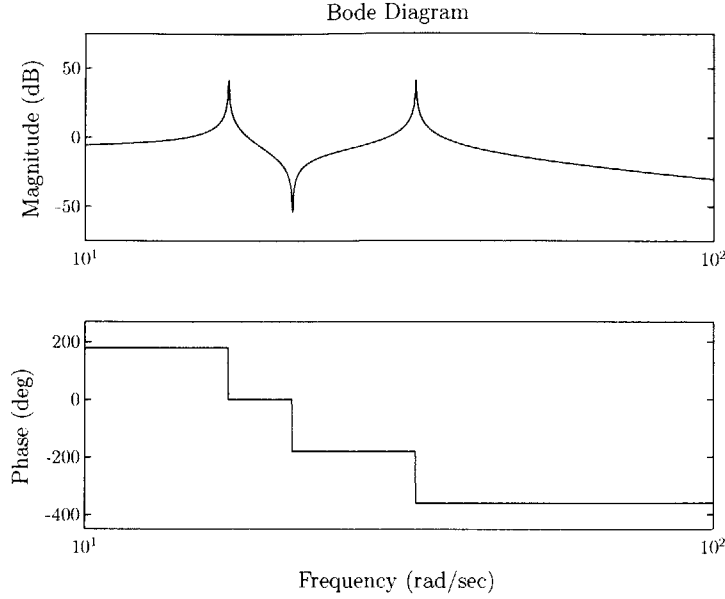


Figure 4-17: Frequency Response of the AFC Resonators. The commanded frequency and therefore the frequency of the first resonator is $\omega_1 = 16.9 \frac{rad}{s}$. The second resonator is placed at the second harmonic or twice the command frequency of $\omega_2 = 33.8 \frac{rad}{s}$.

a range of commanded frequencies instead of being tuned for just a single commanded frequency. This means that phase and gain terms must be chosen in terms of commanded frequency and be sufficiently generic so that system stability is maintained during changes in command frequency.

The frequency response of the load position loop ($G_{out,cl}$) in Fig. 4-15 is given in Fig. 4-9. It shows that the system behaves as a first order system with a pole at $10 \frac{rad}{s}$. The frequency range of interest spans from $1 \frac{rad}{s} - 20 \frac{rad}{s}$, as these are the frequencies that a locomotion gait is useful to operate in for the given actuator. The phase varies from 0 - 90 degrees in this frequency range. Choosing a phase term of $-\pi/4$ radians (45 degrees) ensures that the low side of the discontinuity never drops below -135 degrees and that at least 45 degrees of phase margin is always achieved.

$$g_n = -0.2 \frac{\omega_n}{\sin(\phi_n)} \quad (4.23)$$

The gain of the load position loop stays close to 0dB for the majority of the frequency range. The frequency response of the two resonators is shown in Fig. 4-17. By choosing the gain term in Eq. 4.23, a gain margin of -14dB is achieved for both resonators and stability of the system is ensured. The gain margin is set on the large side because it was found that a higher gain inducing faster convergence would produce some overshoot causing the force control loop to reach the saturation limit at high frequencies.

Fig. 4-19 shows the open loop transfer function of the AFC loop and Fig. 4-20 shows the transfer function of the entire closed loop system with resonators placed at the load resonant frequency and

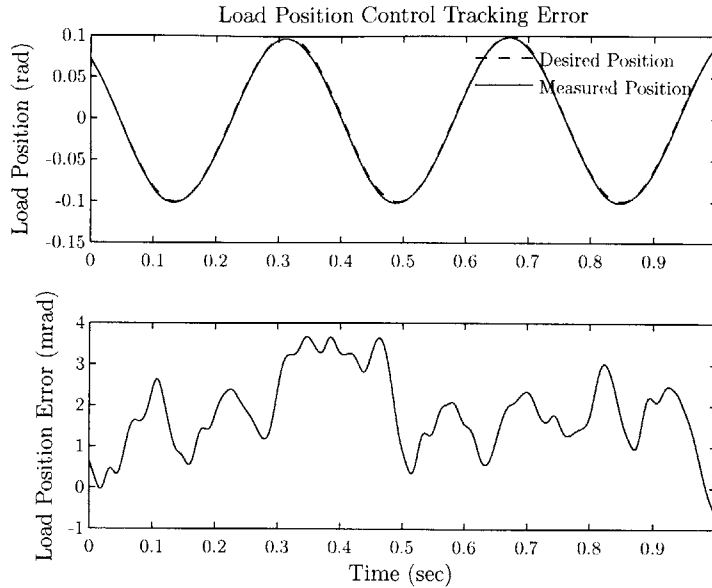


Figure 4-18: Tracking Error with the AFC Loop Closed

its second harmonic. It can be seen from the plot that good tracking is achieved at those two frequencies and thus disturbances will be rejected minimizing error. Fig. 4-18 shows the result when the load position is commanded to the system resonant frequency. The shortcomings of the load position loop are compensated for by the AFC loop and the error signal is reduced to 5.6% of the original error.

4.5.2 Force Limit Violation

Although setting the gain margin to 14dB kept the controller from producing torques that violated the force control limit, disturbance torque on the load could still cause large enough torques in the spring to engage the force limit. When this happened, as stated earlier, the AFC could not maintain control of the system. In order to deal with this problem the AFC resonators are reset and held at zero upon reaching the force limit thus allowing force control to take over and protect the system. Once the spring torque returns safely under the force limit the AFC resonators are allowed to regain control.

4.6 Controller Performance

This section demonstrates the performance of the control scheme through a few representative experiments. Figures 4-19 and 4-20 give the open loop and closed loop bode responses of the AFC loop. The closed loop response shows that at the command frequency ($2.8Hz$) and its second harmonic ($5.6Hz$), the system achieves unity gain and zero phase lag between desired load position

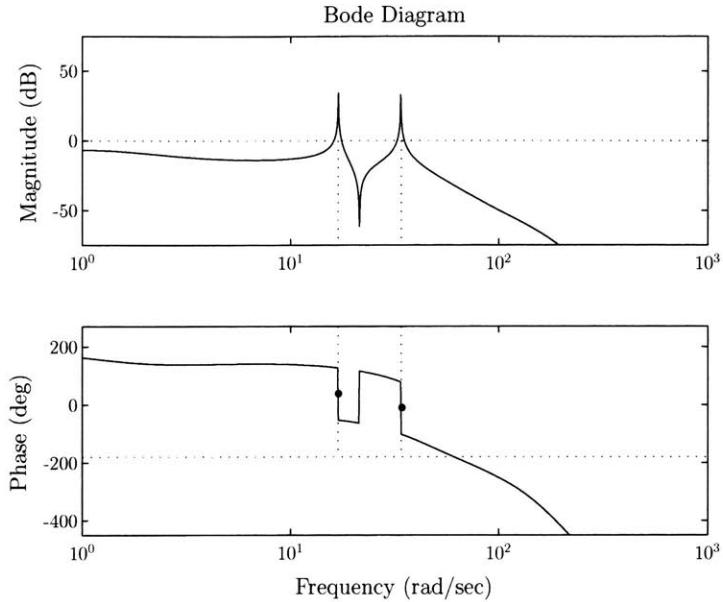


Figure 4-19: Open Loop Frequency Response of the AFC Loop. The midpoints of the phase discontinuities are located at 37.1 degrees for the resonator at the fundamental harmonic resonator and -11.2 degrees for the resonator at the second harmonic. The locations of these discontinuities ensure phase margins of at least $P_m = 127.1$ degrees for the first harmonic and $P_m = 78.8$ degrees for the second harmonic.

and actual load position. This translates to the excellent tracking shown in Figure 4-18.

Figure 4-21 shows the step response of the system. Figure 4-22 shows the resonant response of the system and the system's ability to react to changes in the loading. In this experiment, the nonlinear loading is added during operation forcing the control system to adjust. Figures 4-23 and 4-24 show how the system deals with extreme disturbances that are potentially harmful to the drive train. In these experiments, the load plate is pulled by hand causing the force controller to take over and limit the force in the spring. As a result, the hardware is not damaged and the system can resume control when the disturbance subsides.

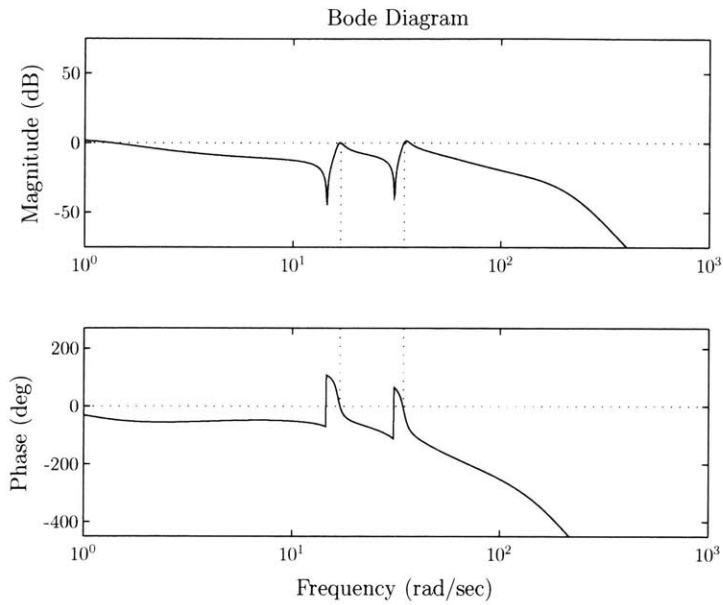


Figure 4-20: Closed Loop Frequency Response of the entire system

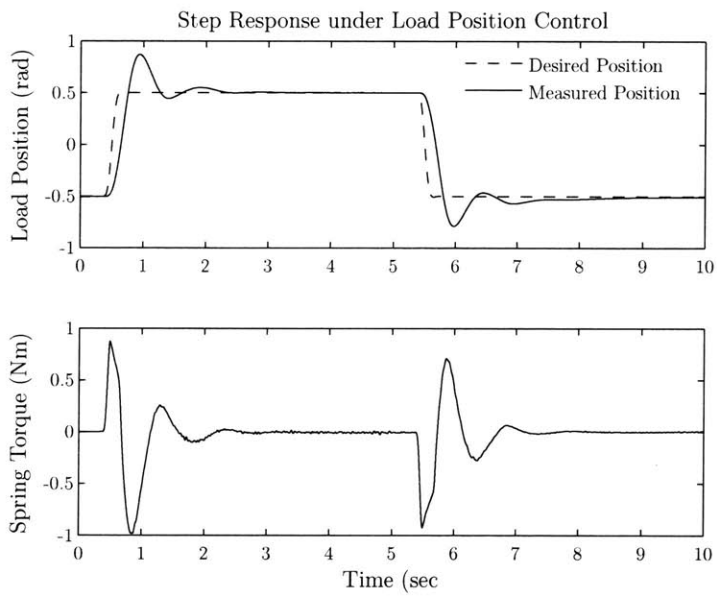


Figure 4-21: Step Response of the system under load position control

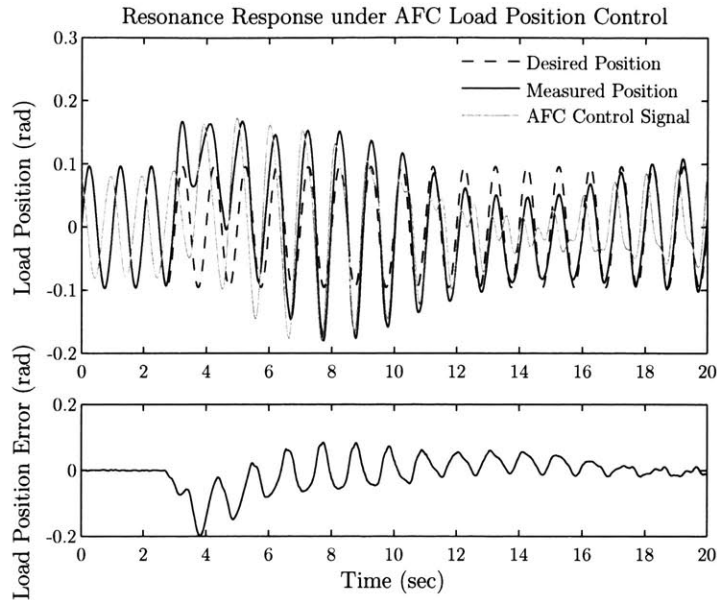


Figure 4-22: System response to a sinusoidal load position command with the AFC loop closed. Initially the system is operating at steady state with the control loop active resulting in negligible position error. At 2.7 seconds the nonlinear loading is added (a bucket with intermittent ground contacts) and the AFC loop reacts and suppresses the disturbance.

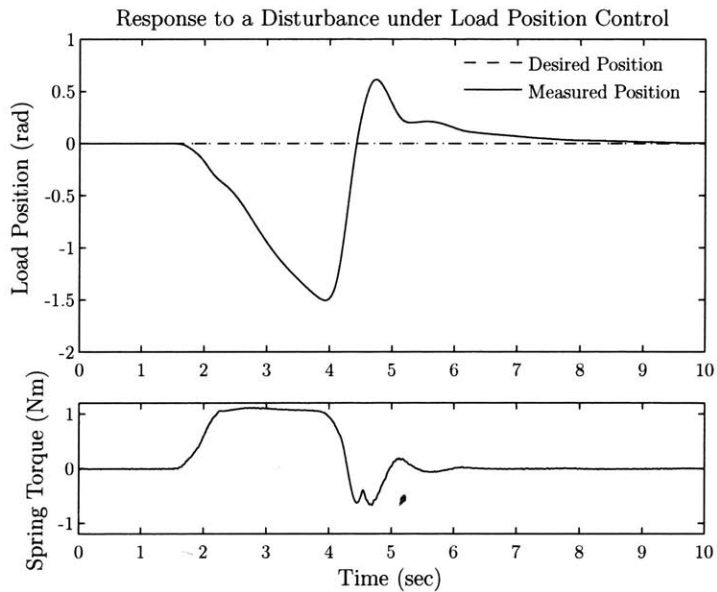


Figure 4-23: Response of the system to a disturbance while not in resonant mode. Initially the load is being held at the desired load position of zero radians. At 1.5 seconds the load plate is pulled by hand to demonstrate the system's response to extreme disturbances. When the spring torque reaches 1Nm the load position control command saturates and the force control loop attempts to hold the spring torque at 1Nm. The load is then release at 4 seconds and once the load position controller asks for a spring torque below the 1Nm limit the load position loop resumes control.

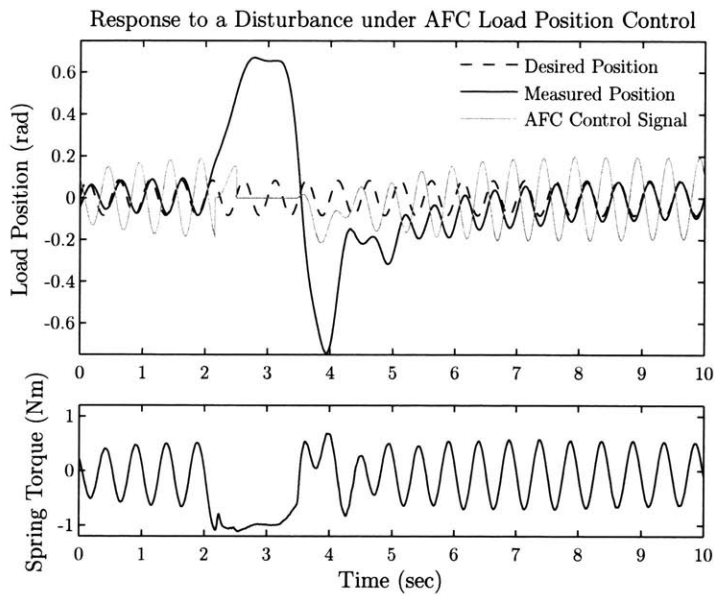


Figure 4-24: Response of the system to a disturbance while the AFC loop is active. Initially the system is under AFC control and the resonators have built up to deal with the position error. At 2 seconds the load plate is pulled by hand to demonstrate the system's response to extreme disturbances. When the system reaches the spring torque limit of 1Nm the load position saturates and the AFC resonators reset leaving the system under force control. The force control loop holds the spring torque at 1Nm until the load position controller stops asking for more than 1Nm at which time the resonators react and the full AFC loop retakes control.

Chapter 5

Power Delivery and Efficiency

Series elastic actuators, like animal muscles and tendons, have the ability to conserve energy during locomotory tasks by storing energy in their elastic element. For efficiency to be gained, however, certain operating conditions must apply. This chapter investigates those conditions in order to characterize the effectiveness of using the actuators to gain efficiency, as well as to determine the mechanisms through which power is lost. In section 5.1 the system is run open loop in order to determine the potential efficiency gains of the system. The control loop is then closed in section 5.2 and the efficiency of the controlled system is explored. The frictional loading presented in section 3.5.2 is used for the open loop data taken in section 5.1 and the control response data taken in section 5.2. Finally, in section 5.3 the nonlinear inertial load described in section 3.5.2 is added to the friction load in order to quantify the efficiency of the actuator under more realistic conditions.

5.1 Open Loop

The open loop power response of the system represents the potential performance achievable by the system. It is used as a baseline to investigate the losses due to extra layers of complexity such as nonlinearities and control.

5.1.1 Linear Model

The ideal system, obtained by substituting the linear environmental loading term, $b_e \dot{\phi}_L$ in for $E(\dot{\phi}_L)$ in eq. 3.34, provides the highest benchmark of actuator performance. A comparison of the experimental results to the ideal model is used later to shed light on the mechanisms that limit actuator performance and reduce efficiency. The models updated with the linear environmental damping term are given here.

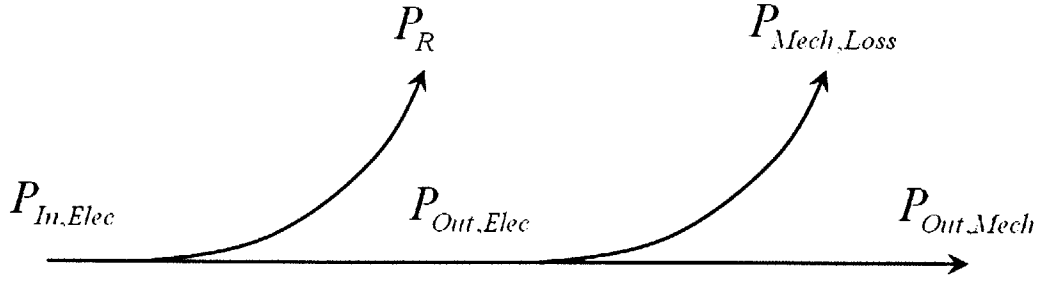


Figure 5-1: Power flow diagram of the actuator and load.

$$G_{p,mv}(s) = \frac{k_t(J_L s^2 + (b_L + b_E)s + k_s)}{J_m J_L s^3 + (b_m J_L + (b_L + b_E)J_m)s^2 + (b_m(b_L + b_E) + k_s J_{eq})s + k_s b_{eq}} \quad (5.1)$$

$$G_{p,tv}(s) = \frac{k_t k_s / N}{J_m J_L s^3 + (b_m J_L + (b_L + b_E)J_m)s^2 + (b_m(b_L + b_E) + k_s J_{eq})s + k_s b_{eq}} \quad (5.2)$$

$$G_{p,f}(s) = \frac{\frac{k_t k_s}{N}(J_L s + (b_L + b_E))}{J_m J_L s^3 + (b_m J_L + (b_L + b_E)J_m)s^2 + (b_m(b_L + b_E) + k_s J_{eq})s + k_s b_{eq}} \quad (5.3)$$

$$b_{eq} = b_m + (b_L + b_E)/N^2 \quad J_{eq} = J_m + J_L/N^2$$

The power flow of the system is broken up into three stages, the input power drawn from a source ($P_{In,Elec}$), the power transferred from the electromagnetic domain to the mechanical domain ($P_{Out,Elec}$) and the power output by the actuator ($P_{Out,Mech}$). Figure 5-1 illustrates the three stages of power flow graphically as well as shows the loss terms.

The power at each stage is calculated by multiplying the two conjugate variables effort and flow. Voltage and current are multiplied in the electromagnetic domain while torque and velocity are multiplied in the mechanical domain.

$$P_{In,Elec} = V_s I_d = R_{eq} I_d^2 + V_{b,eq} I_d = (R_{eq} + k_t(G_{p,mv})^*) I_d^2 \quad (5.4)$$

$$P_{Out,Elec} = V_{b,eq} I_d = \dot{\phi}_m \tau_m = k_t(G_{p,mv})^* I_d^2 \quad (5.5)$$

$$P_{Out,Mech} = \dot{\phi}_L \tau_s = G_{p,f}(G_{p,tv})^* I_d^2 \quad (5.6)$$

$$R_{eq} = \frac{3}{2} R_c \quad V_{b,eq} = \frac{3}{2} k_t \dot{\phi}_m$$

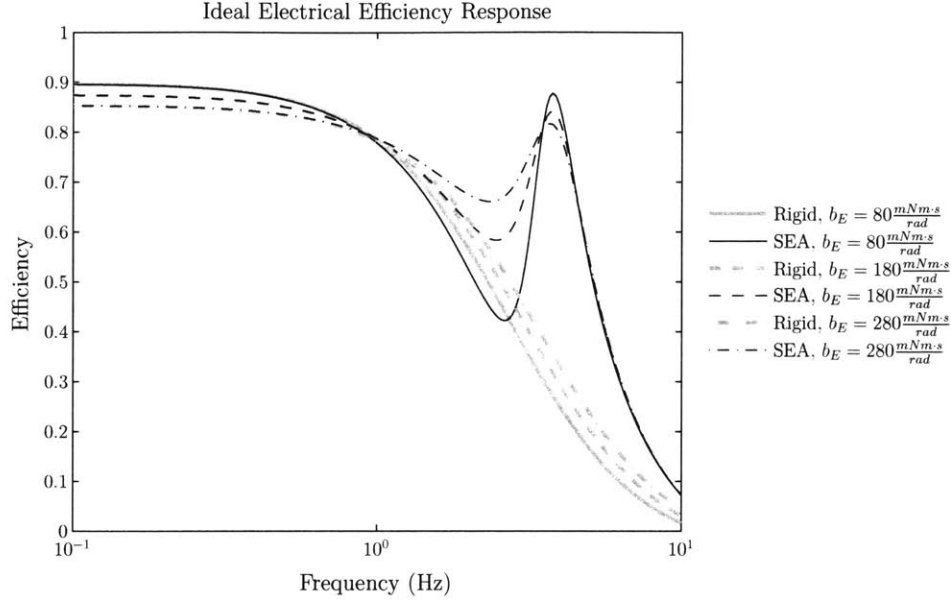


Figure 5-2: Ideal Electrical Efficiency Response. The plot shows that there is a drop in electrical efficiency at the load resonance. This drop in efficiency is due to the decrease in motor velocity. There is a then a peak in electrical efficiency at the system resonance before efficiency rolls off at high frequencies.

Where R_{eq} and $V_{b,eq}$ are the equivalent coil resistance and back Emf when the motor is viewed as a lumped linear DC model. The efficiency is then found by taking the ratio of output power to input power. Electrical efficiency (η_{Elec}) is the ratio of the power transferred between the electrical and mechanical domains to the total input power. It illustrates the effect resistive losses have on the system. Mechanical efficiency (η_{Mech}) is the ratio of the power output to the load to the power transferred to the mechanical domain. It shows the effect friction losses have on the system. The total system efficiency (η_{System}) is then the ratio of the power output to the load to the total input power draws by the system.

$$\eta_{Elec} = \frac{P_{Out,Elec}}{P_{In,Elec}} \quad (5.7)$$

$$\eta_{Mech} = \frac{P_{Out,Mech}}{P_{Out,Elec}} \quad (5.8)$$

$$\eta_{System} = \frac{P_{Out,Mech}}{P_{In,Elec}} \quad (5.9)$$

The ideal electrical, mechanical and overall system efficiencies given varying load damping are plotted in Figures 5-2, 5-3 and 5-4 respectively. In each plot the efficiency values of the compliant series elastic system are compared with those of a rigid system by sending the spring stiffness to infinity. Figure 5-4 clearly shows that under certain loading conditions there is a peak in the actuator efficiency at $3.25Hz$ for light damping to $3Hz$ for heavier damping that is not present with the rigid

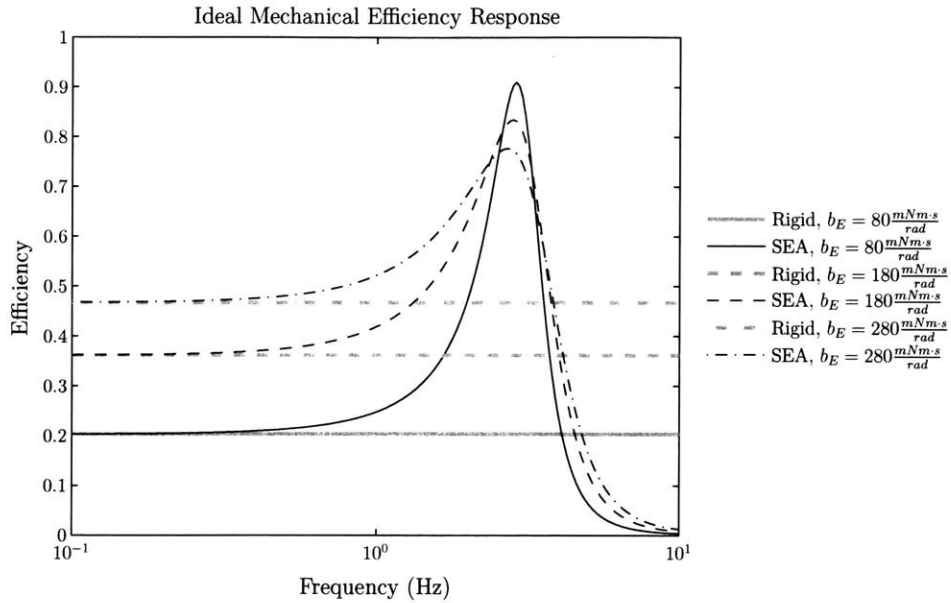


Figure 5-3: Ideal Mechanical Efficiency Response. The plot shows the large peak in mechanical efficiency present at the load resonance due to the decrease in motor movement necessary to produce output movement.

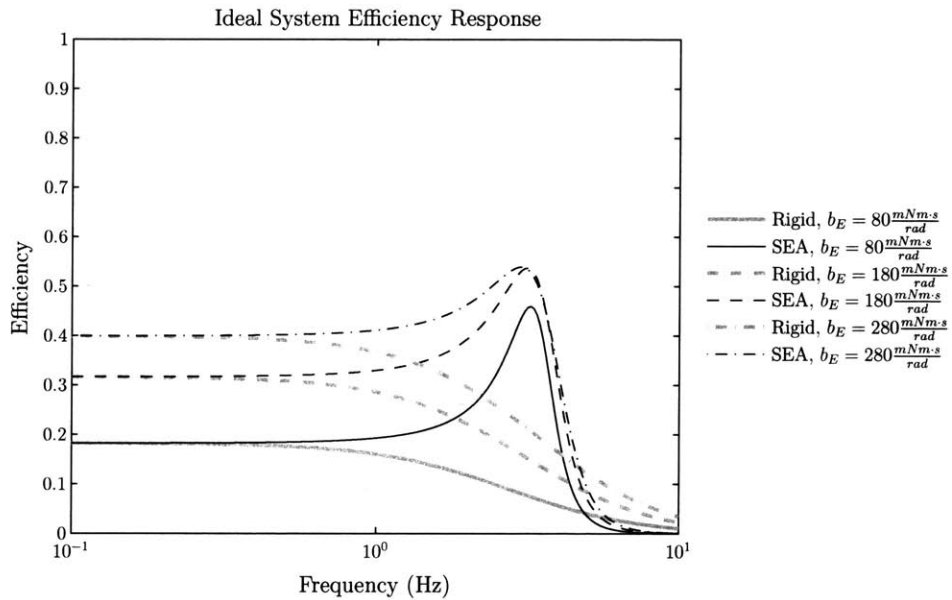


Figure 5-4: Ideal Efficiency Response of the entire Series Elastic Actuator. An efficiency peak occurs between the load resonance frequency and the system resonance frequency indicating that efficiency can be scavenged by series elastic actuators if operated at the optimal frequency

actuator. This peak represents an efficiency increase as a result of the resonant mode of the actuator.

Series elastic actuators exhibit significant efficiency gains over rigid actuators for a range of load damping values. The ideal model shows that for the current hardware, that range exists from no load to approximately 20 times the bearing friction term. The efficiency gains over a rigid system are maximized at low damping values (approximately 0 - 5 times the bearing friction term) while system efficiency in general increases as load damping increases. This indicates that the system efficiency would be truly maximized under large loading conditions such that the resonant modes of the system are heavily damped. Loading conditions, however, are not predetermined and a robot therefore may have to operate in ranges of lower damping. Human walking and running gait for example are lightly damped by the environment because the direction of movement is parallel with the environmental interface. For these types of lightly damped applications series elastic actuators have the potential to be exploited for large efficiency gains if run at the appropriate frequency.

The plots of the system mechanical and electrical efficiency provide an explanation for the resulting system efficiency gain. In Figure 5-3, a peak in mechanical efficiency similar to that of the system efficiency is present due to the resonance between the spring and the load inertia (load resonance). This resonance only requires small oscillation at the motor inertia to create large movements at the output inertia and as a result requires very little mechanical power to drive the system. It is notable, however, that this peak in mechanical efficiency is lower in frequency than the system efficiency peak and cannot account for the gain in system efficiency alone. In the rigid system, the electrical efficiency shown in Figure 5-2 drops at frequencies above $1Hz$ as the load impedance as seen through the coils becomes reactive. This drop is present in the series elastic system as well and counteracts some of the gains achieved in mechanical efficiency. In addition, the decrease in motor movement in reaction to the load resonance causes its own drop in efficiency due to the fact that motor electronics are much less efficient at low motor velocities. This drop is focused at the height of the mechanical efficiency peak and therefore works to counteract the gains achieved in the mechanical domain. The electrical efficiency, however, has an efficiency peak much like the one in the mechanical efficiency. It appears at frequencies above the system efficiency peak and is the result of assistive coupling between the load inertia and the motor inertia through the spring. The combination of the gains in mechanical efficiency and electrical efficiency create the peak in the overall system efficiency that can be exploited during oscillatory tasks.

5.1.2 Hardware Response

Although the ideal system confirms the hypothesis that series elastic actuators have the potential for efficiency gains at resonance, the actual system is not ideal and therefore the potential of the real system is given by the hardware's open loop response. Data is taken on the hardware and is compared to the ideal system. Through this comparison, non-idealities that hinder performance are

identified and an updated non-ideal model is used to help explain them.

Data Acquisition

In order to measure the power flow of the system, $P_{In,Elec}$, $P_{Out,Elec}$ and $P_{Out,Mech}$ were measured instantaneously in real time by calculating the product of the two conjugate variables (Voltage/Current, Velocity/Torque). $P_{In,Elec}$ was taken as the sum of the power flowing into the motor on each of the three electrical phases. The power on each phase was found by multiplying the voltage on each phase measured at the output of the OPA549 and the current on each phase measured across the sense resistors using the INA128. No filtering was performed on these signals. $P_{In,Elec}$ was taken at the input to the motor, therefore motor driver and CPU inefficiencies are not taken into account in this analysis. The losses from the computer and driver electronics should be small, thus the results found are taken as representative for real world application. Sample data of $P_{In,Elec}$ is given in Figure 5-5. $P_{Out,Elec}$ was taken as the product of the motor torque and the motor angular velocity. The motor torque is calculated from the current measured on each phase using Eq. 5.10 restated below from Section 3.2.2.

$$\tau_m = k_{t,p}(\sin(\phi_e)i_A + \sin(\phi_e - \frac{2\pi}{3})i_B + \sin(\phi_e + \frac{2\pi}{3})i_C) \quad (5.10)$$

The motor velocity was found by differentiating the motor position signal obtained by the am256 magnetic encoder. Although the signal from the encoder is inherently noisy and thus the velocity is noisier still due to the differentiation, the unfiltered velocity signal was used in the power calculation to avoid errors due to filtering delays. The accuracy of the calculation of $P_{Out,Elec}$ was validated by taking data over ten mechanical cycles and comparing the average of the real time power calculation to a post processed equivalent in which the velocity signal was filtered with a zero phase filter. Sample data of the $P_{Out,Elec}$ calculation is given in Figure 5-6. $P_{Out,Mech}$ is calculated by taking the product of the spring torque and the load velocity. Both signals depend on the am256 magnetic encoder and are noisy. Both signals are filtered by a 6th order Bessel filter with a cutoff frequency at $200rad/s$ ensuring equal phase distortion. Sample data of the $P_{Out,Mech}$ calculation is given in Figure 5-7. The three power signals were then filtered in real time with a cutoff frequency of $0.1rad/s$ in order to obtain average power. The power frequency response plots given in this chapter use the filtered power signals described here measured and averaged over ten mechanical cycles of the load.

Open Loop Results

Load friction is applied by two metal rods that are pressed up against opposite sides of the load plate as shown in Figure 5-8. This setup creates a frictional force ($\tau_{f,E}$) that is opposite to the direction of the load plate movement and is proportional to the normal force applied by the rods known as

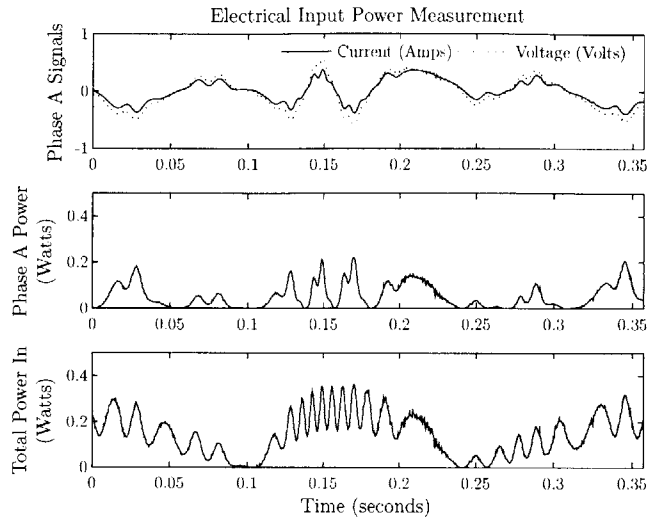


Figure 5-5: Representative Waveforms of the Electrical Input Power Calculation. Phase current and voltage are multiplied to get the instantaneous phase power. The instantaneous phase powers are then summed to get the instantaneous input power. The instantaneous input power is then filtered to obtain the average input power.

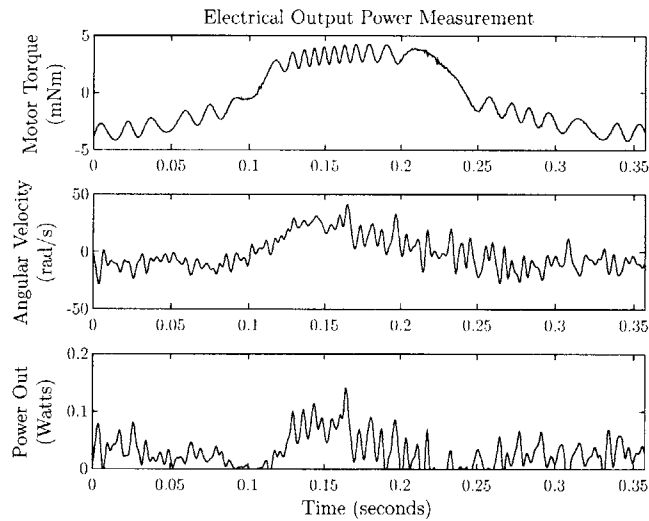


Figure 5-6: Representative Waveforms of the Electrical Output Power Calculation. Motor torque is multiplied by motor angular velocity to obtain instantaneous electrical output power. The instantaneous power is then filtered to obtain the average electrical output power.

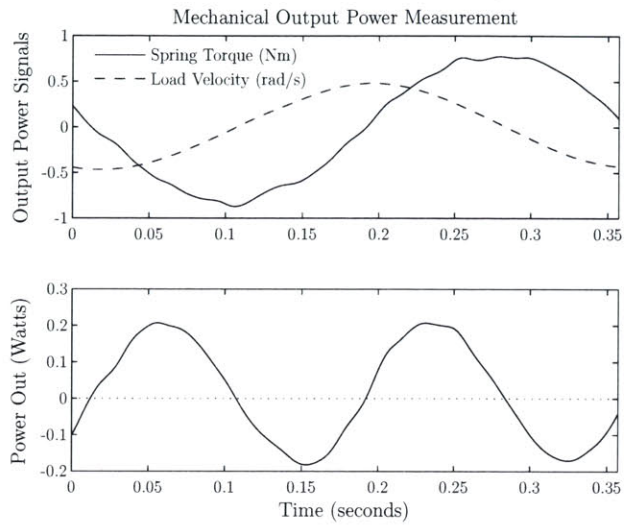


Figure 5-7: Representative Waveforms of the Mechanical Output Power. Spring torque is multiplied by the load velocity to get the instantaneous mechanical output power. The instantaneous output power is then filtered to obtain the average mechanical output power.

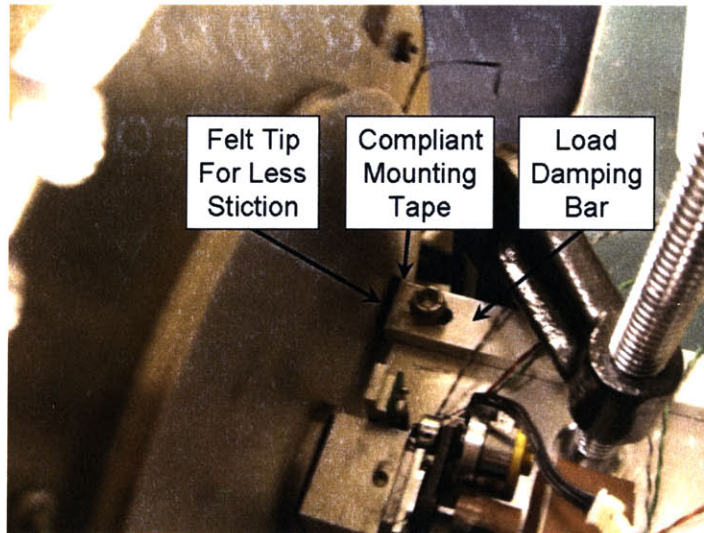


Figure 5-8: Picture of the damping mechanism used on the load. The two bars are pressed up against the load plate to create viscous friction. The bars are covered with felt at the end to minimize stiction. The felt is attached to the bar with layers of compliant mounting tape to increase damping coefficient resolution.

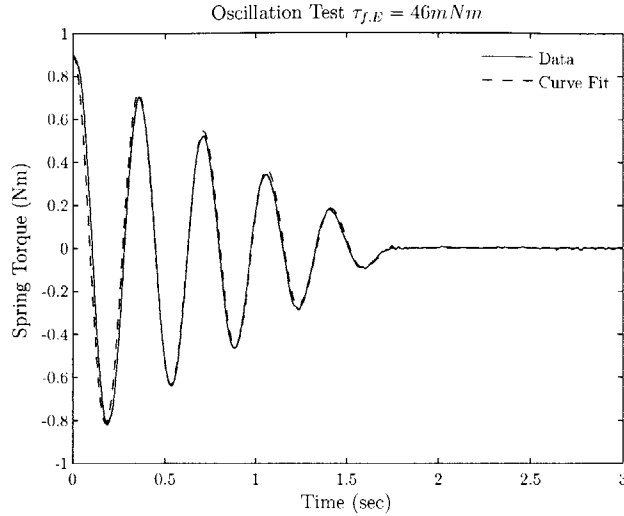


Figure 5-9: Representative Waveforms of the oscillation test used to determine load friction values. The data was taken by holding the load plate at a constant torque while the motor was locked, then releasing and recording the response. The data was then curve fit with a simulated response using a least squares method.

coulomb friction. The rods are fitted with felt tips that are attached with compliant mounting tape to increase the resolution of the normal force.

Power frequency response data for this thesis is taken at three values of load friction, low loading ($\tau_{f,E} = 45mNm$), medium loading ($\tau_{f,E} = 85mNm$) and heavily loaded ($\tau_{f,E} = 125mNm$). The load friction torques were determined by running oscillation tests and fitting a simulated response to the resulting spring torque signal. This is shown for the $\tau_{f,E} = 45mNm$ load in Figure 5-9.

The load friction applied to the hardware, although similar to the linear damping in that it is in phase with the load velocity, is nonlinear and provides a different system response than that of the ideal model. Simulations of the system efficiency were run using the model given in eq. 3.34 and are compared with the linear results in Figure 5-10. The plot shows that there is a discrepancy in the efficiency response between the linear system and the system with the coulomb friction loading. At frequencies away from resonance the efficiency of the system with coulomb friction is less than that of the linear system. At resonance, however, the systems behave very similarly and a large efficiency gain at resonance is still expected. Also, the similarity between the models at frequencies close to resonance show that the mechanisms responsible for the gain in efficiency identified using the linear model are still present despite the nonlinear loading.

The open loop power response for a load friction of $\tau_{f,E} = 46mNm$ is given in Figure 5-11. The open loop power response for a load damping of $\tau_{f,E} = 85mNm$ is given in Figure 5-12. And the open loop power response for a load damping of $\tau_{f,E} = 45mNm$ is given in Figure 5-13.

The figures show that the efficiency peak predicted in the ideal model is present but it is much

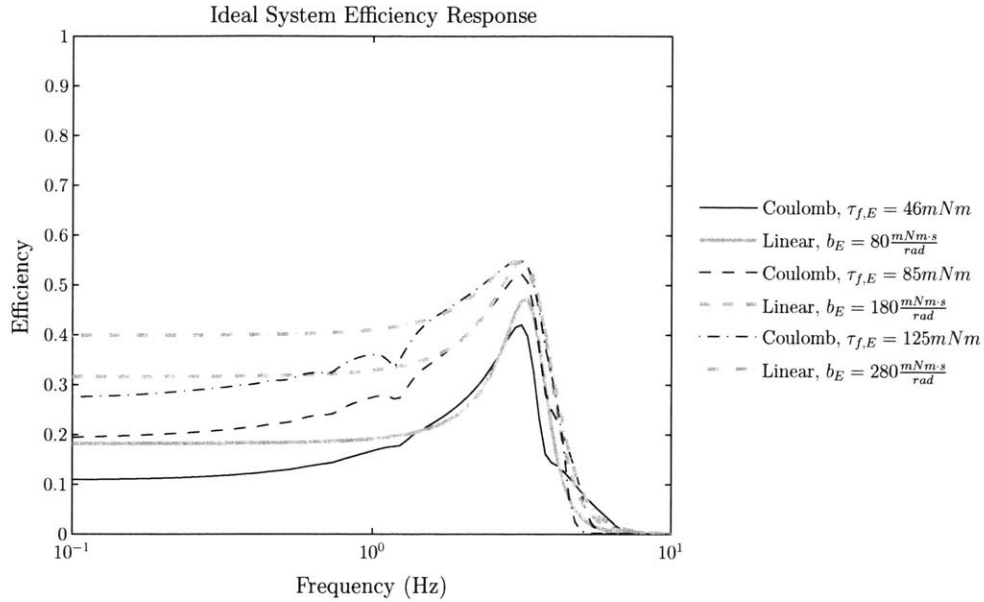


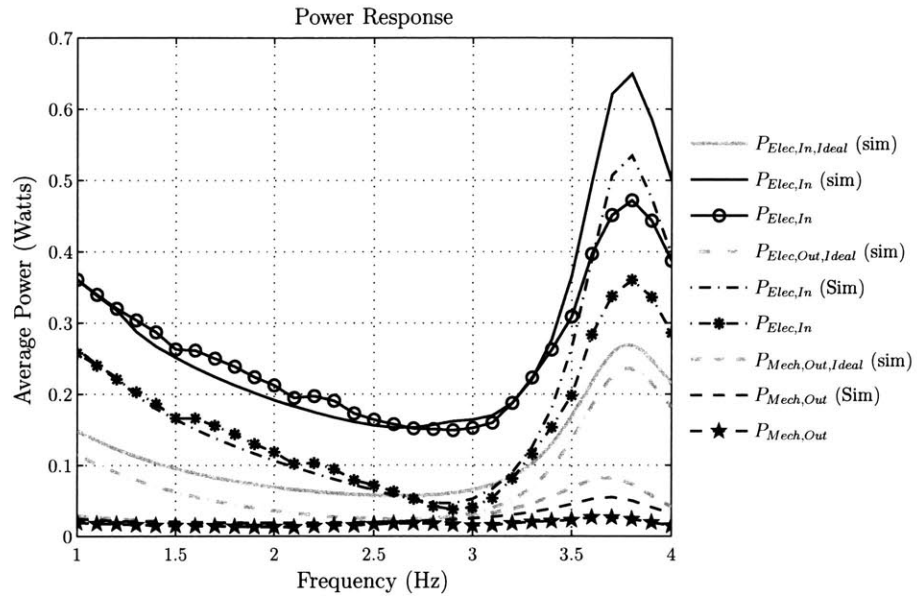
Figure 5-10

lower than expected. For the $\tau_{f,E} = 45mNm$ load the system efficiency peaks at $\eta_{System,2.8Hz} = 12\%$ at a frequency of $2.8Hz$. This is 2.2 times the solid shaft efficiency of $\eta_{System,1Hz} = 5.4\%$ at a frequency of $1Hz$. Unfortunately it is also four times smaller than the ideal system efficiency peak at $\eta_{System,Ideal} = 46\%$. The same trend is followed under the other two loading conditions. The peak efficiencies and their relation to the efficiencies away from resonance are given in Table 5.1 for all of the loading conditions. The plots also show that the hardware follows the same trend as the ideal model, in that the efficiency at all frequencies increases as load friction increases. As predicted the system gets the highest efficiency, and subsequently the lowest efficiency gain due to the resonance peak, when heavily loaded. In turn, it generates the largest gains over a rigid system at low friction values. It is clearly shown, however, that for a wide range of loading conditions, the highest attainable efficiency is achieved by operating a series elastic actuator at resonance.

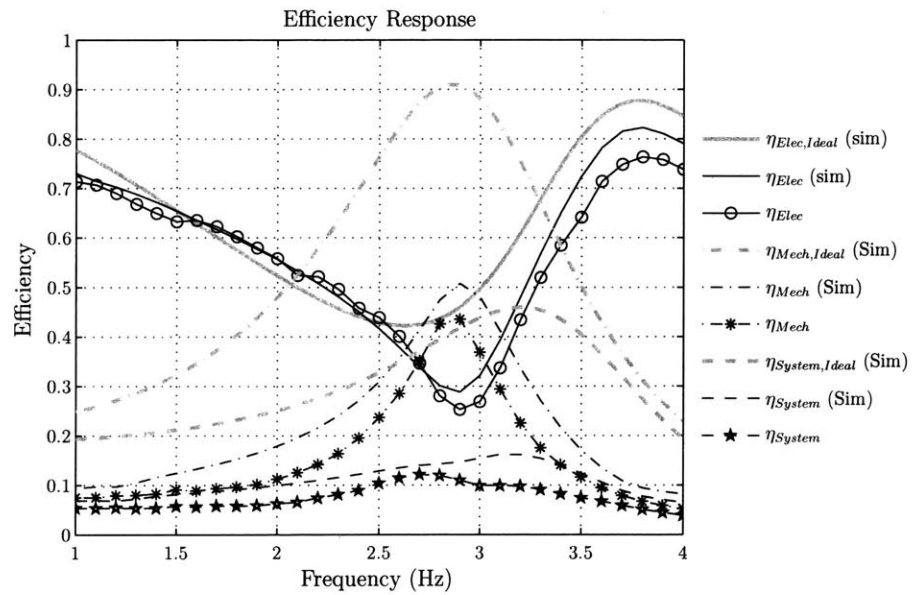
	$\tau_{f,E} = 46mNm$	$\tau_{f,E} = 85mNm$	$\tau_{f,E} = 125mNm$
1Hz Efficiency	5.4%	12.8%	16.5%
2.8Hz Efficiency	12%	18%	21.7%
Efficiency Gain	2.2	1.4	1.3

Table 5.1: Open Loop Efficiency Values.

The cause for the drop in efficiency from the ideal system to the real system is mainly due to the presence of motor stiction which is not modeled in the ideal system. Stiction losses affect the system efficiency two ways. Motor stiction (meaning stiction of the motor and gear train) creates a mechanical power loss in phase with the motor velocity reducing mechanical efficiency. In order

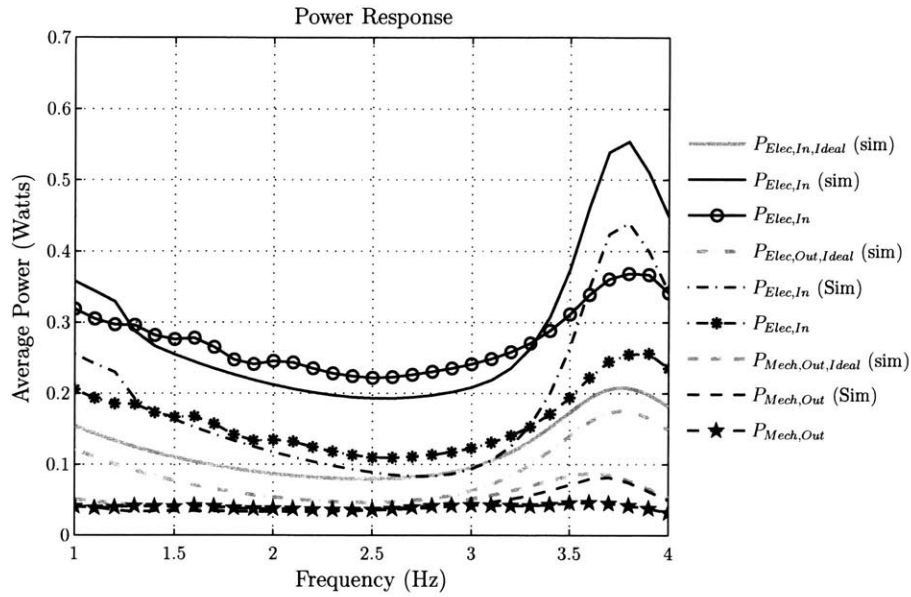


(a) Open Loop Power Response

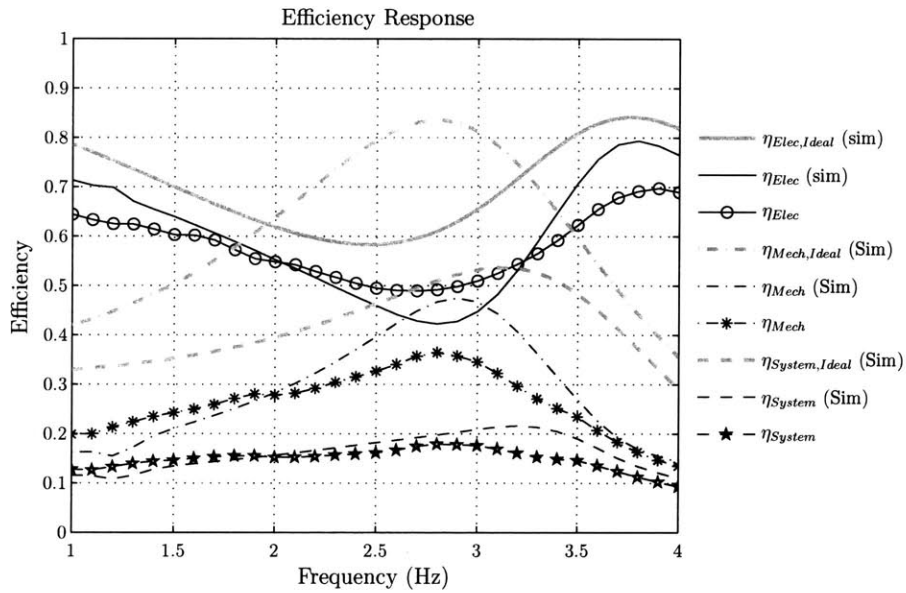


(b) Efficiency Response

Figure 5-11: Open Loop Efficiency Response under low loading. These plots represent the load friction case where $\tau_{f,E} = 46mNm$. The system exhibits a peak in efficiency at $2.8Hz$ and has the largest gain in efficiency of the three loading values used. A significant drop in efficiency from the ideal case is demonstrated due to motor/gear stiction.

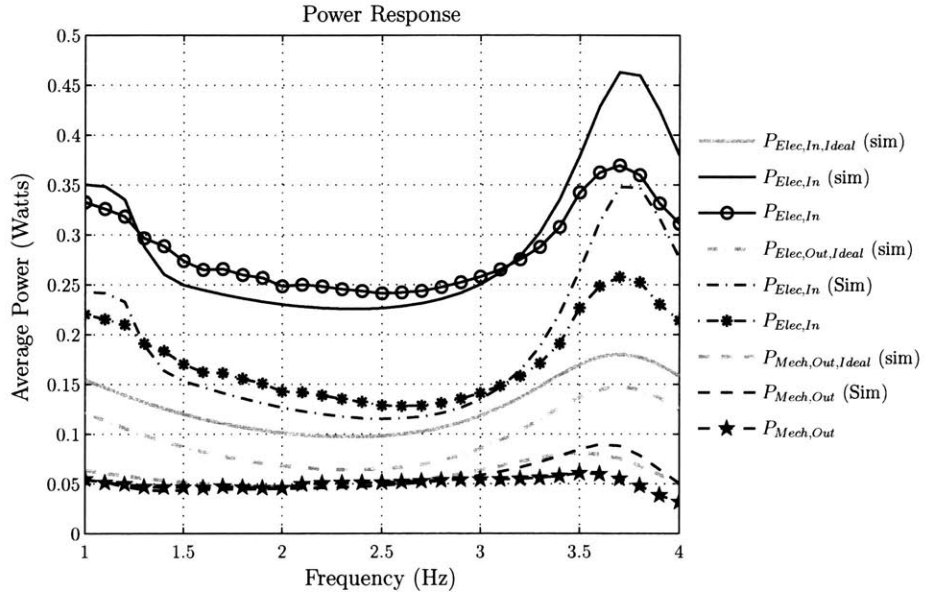


(a) Open Loop Power Response

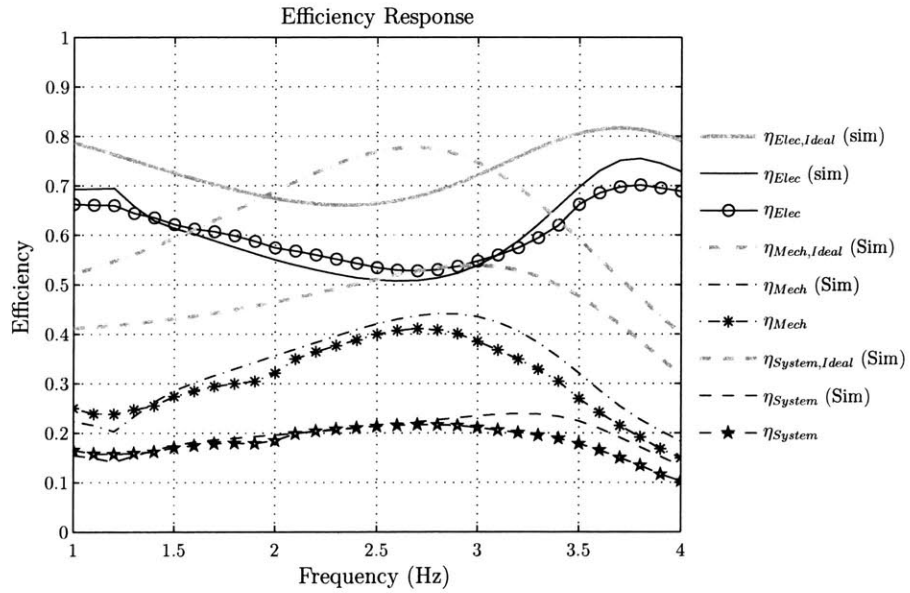


(b) Open Loop Efficiency Response

Figure 5-12: Open Loop Efficiency Response under medium loading. These plots represent the load friction case where $\tau_{f,E} = 85mNm$. Like the low loading case the system exhibits a peak in efficiency at $2.8Hz$, however, it does not have as high efficiency gains as the low loading case. It also exhibits higher efficiency away from resonance than the low loading case. Again there is a large drop in efficiency from the ideal case due to stiction.



(a) Open Loop Power Response



(b) Open Loop Efficiency Response

Figure 5-13: Open Loop Efficiency Response under high loading. These plots represent the load friction case where $\tau_{f,E} = 125mNm$. Like the other two cases the system exhibits a peak in efficiency at $2.8Hz$ and a large drop in efficiency from the ideal case due to stiction. This case yields the highest overall efficiency both at and away from resonance.

to compensate for the motor stiction extra current is drawn, creating higher resistive losses in the motor thus reducing electrical efficiency.

Motor Stiction Model

A model of motor stiction using the linear system model is presented here to help understand the resulting efficiency drops. Due to the similarity between the linear model and the model with coulomb friction, the linear model can be used to shed light on trends in power loss. Analytical relations for power loss in terms of the amplitude and frequency of the commanded current are derived below.

The effect of motor stiction is to produce a torque that is in the opposite direction as the motor movement. Although the stiction mechanism is a complex nonlinear system as described in Section 3.4, for simplicity it can be modeled as a constant torque in the power calculation without incurring a large error.

$$\tau_{ms}(\dot{\phi}_m) = k_t i_{ms,0} \text{sign}(\dot{\phi}_m) \quad (5.11)$$

Where τ_{ms} is the stiction torque, $i_{ms,0}$ is the stiction compensation current. The velocity in an oscillatory system is:

$$\dot{\phi}_m = |G_{p,mv}(s)| i_d \sin(\omega t + \psi_{ms}) \quad (5.12)$$

The power lost due to motor stiction is then found by taking the product of the stiction torque and the motor velocity.

$$P_{ms} = \tau_{ms} \dot{\phi}_m = k_t i_{ms,0} i_d |G_{p,mv}(s)| |\sin(\omega t + \psi_{ms})| \quad (5.13)$$

Integrating Equation 5.13 over one cycle then yields the average power loss due to motor stiction.

$$P_{ms,avg} = \frac{2}{\pi} k_t i_{ms,0} i_d |G_{p,mv}(s)| \quad (5.14)$$

The extra current that is needed to overcome stiction is calculated by the controller's feedforward stiction compensation term and is proportional to the stiction torque.

$$i_{ms} = \frac{\tau_{ms}}{k_t} \quad (5.15)$$

This current is in phase with the motor velocity and therefore is not always in phase with the open loop driving current. The total current is then the sum of the stiction current and the driving current.

$$i = \begin{cases} i_d \sin(\omega t) - i_{ms,0} & \text{for } 0 \leq t \leq \psi_{ms} \\ i_d \sin(\omega t) + i_{ms,0} & \text{for } \psi_{ms} \leq t \leq \frac{T}{2} \end{cases} \quad (5.16)$$

Where ψ_{ms} is the phase offset between the driving current and the motor velocity. The resistive losses are then calculated using the total current in the usual fashion.

$$P_R = R_{eq} i^2 = \begin{cases} R_{eq} \left(i_d^2 \sin^2(\omega t) - 2i_{ms,0} i_d \sin(\omega t) + (i_{ms,0})^2 \right) & \text{for } 0 \leq t \leq \psi_{ms} \\ R_{eq} \left(i_d^2 \sin^2(\omega t) + 2i_{ms,0} i_d \sin(\omega t) + (i_{ms,0})^2 \right) & \text{for } \psi_{ms} \leq t \leq \frac{T}{2} \end{cases} \quad (5.17)$$

The average resistive power lost is then found by integrating 5.17 over half a cycle and simplifying.

$$P_{R,avg} = R_{eq} \left(\frac{1}{2} i_d^2 + \frac{4}{\pi} i_d i_{ms} \cos(\psi_{ms}) + (i_{ms,0})^2 \right) \quad (5.18)$$

Eq. 5.14 describes the average mechanical power loss due to motor stiction. The stiction force is a constant value that is in phase with the motor velocity, therefore the motor velocity response is the only variable term in the equation. The amount of mechanical losses produced are proportional to the magnitude of the motor velocity at each command frequency. This says that at load resonance, where motor movements are small, the mechanical power lost due to stiction is small as well. In turn, at frequencies away from resonance, motor stiction has a much larger effect on the system performance. This is precisely the mechanism that allows series elastic actuators create efficiency gains.

Eq. 5.18 describes the average electrical power loss due to motor current. This term represents the majority of discrepancy in efficiency between the ideal models and the experimental data. The first and last terms of the eq. 5.18 represent the direct losses from the commanded current and the current drawn to compensate for stiction respectively. The commanded current is scaled by $\frac{1}{2}$ because it is sinusoidal whereas the stiction current maintains a constant depending on the direction of the motor movement. The middle term accounts for the difference in phase between the motor movement and the commanded current. As they become more out of phase the resistive losses drop. The decrease in power loss from the phase term is small compared to the total resistive losses and yields negligible increases in efficiency. Also, at frequencies in which the motor velocity is out of phase from the command current, the velocity magnitude is attenuated causing a drop in mechanical power. This creates a drop in efficiency that far outweighs the increase from the phase term.

With the stiction terms, the input power becomes the sum of the mechanical stiction losses, the updated resistive losses and the ideal power transferred from the electromagnetic domain to the mechanical domain.

$$P_{In,Elec} = P_{R,avg} + P_{ms,avg} + k_t(G_{p,mv})^*i_d^2 \quad (5.19)$$

Subtracting out the resistive losses gives the electrical output power.

$$P_{Out,Elec} = P_{ms,avg} + k_t(G_{p,mv})^*i_d^2 \quad (5.20)$$

Similar motor stiction terms are added to the model containing the nonlinear load friction and the results are compared to the hardware results in Figures 5-11, 5-12 and 5-13. The stiction terms account for a majority of the discrepancy between the ideal model and the hardware results. This illustrates the importance of minimizing bearing stiction in robotic systems whether they are driven with rigid actuators or compliant actuators. Nevertheless, efficiency can still be gained through the use of series elastic actuators despite the presence of stiction losses.

It can be seen in Figures 5-11, 5-12 and 5-13 that the non-ideal model updated with the stiction losses corresponds nicely with the hardware results at lower frequencies. At higher frequencies at and above the system resonance, however, there is still discrepancy between the model and the data. In fact the system efficiency peak is lower in the data than it is in the model and occurs at the peak in mechanical efficiency. This lower efficiency peak is believed to be due to the fact that the harmonic gearbox is for the most part, not backdriveable. As explained in Section 5.1.1 the system's efficiency peak ideally lands between the load resonance and the system resonance, but because the gearbox isn't backdriveable there is less coupling between the load inertia and the motor inertia and the effect of the system resonance is suppressed. The result is that the load resonance dominates causing the system efficiency peak to be aligned with it.

5.2 Controlled Response

Although the open loop results give merit to the claim that efficiency can be gained by exploiting the resonant modes of series elastic actuators, the results do not confirm the actuator's feasibility in real world applications. In order to show that the actuators can produce efficient locomotion when realistically applied, power frequency response tests were run with the control scheme developed in Chapter 4 active. These test were run under the same loading conditions as the open loop test and are plotted in Figure 5-14 for $\tau_{f,E} = 46mNm$, Figure 5-15 for $\tau_{f,E} = 85mNm$ and Figure 5-16 for $\tau_{f,E} = 125mNm$. The plots show that even though the efficiency suffers a great deal due to the active control, gains are still achieved at resonance proving that the elastic nature of the actuators can be exploited for efficiency during practical application. As in the open loop case, the largest gains occurred under the lowest loading with much lower gains but higher overall efficiency at the higher loadings. For the $\tau_{f,E} = 46mNm$ load the system efficiency peaks at $\eta_{System,2.8Hz} = 4.7\%$

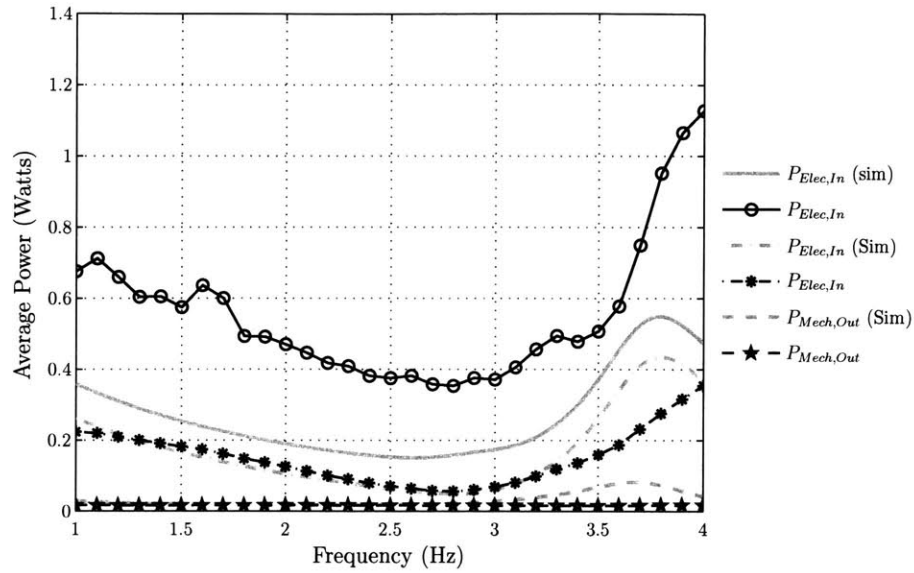
at a frequency of $2.8Hz$. This is 1.9 times the efficiency below resonance of $\eta_{system,1Hz} = 2.5\%$ at 1Hz. The gains for all of the loading conditions are given in Table 5.2.

	$\tau_{f,E} = 46mNm$	$\tau_{f,E} = 85mNm$	$\tau_{f,E} = 125mNm$
1Hz Efficiency	2.5%	7.1%	8.7%
2.8Hz Efficiency	4.7%	9.5%	11%
Efficiency Gain	1.88	1.34	1.26

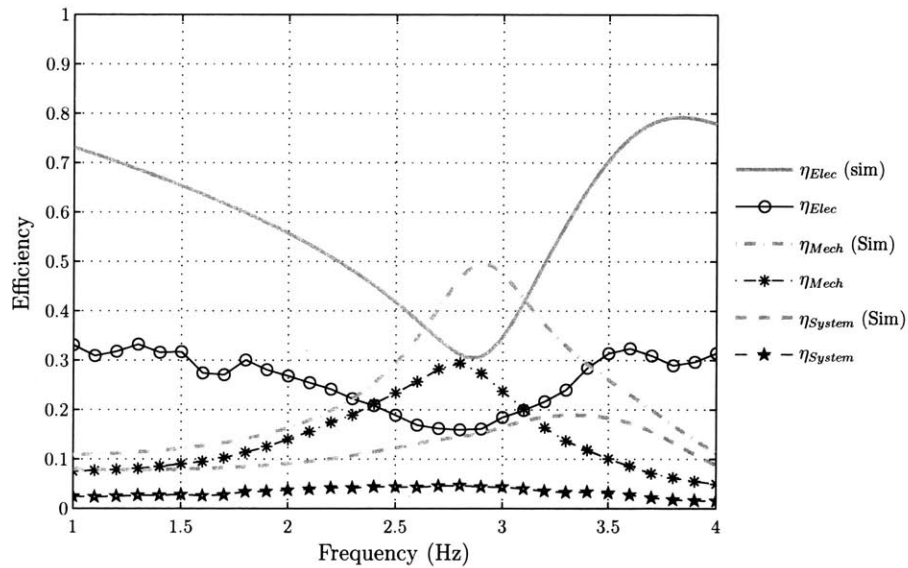
Table 5.2: Controlled Efficiency Values.

Unfortunately the system's efficiency does take a major blow due to the addition of control. In Figures 5-14, 5-15 and 5-16 the controlled results are compared with the open loop results. Under all of the loading conditions, both the electrical and system efficiencies were reduced by almost a half. The reduction in efficiency stems from the control algorithm's demand for current to make fine adjustments to the motor position that allow it to maintain stable force control. Extra motor current adds to the resistive electrical losses without increasing the power output of the system, thus efficiency is lost.

It is not unreasonable for the control algorithm to use some power to achieve a controlled system. The amount of power being used, however, is excessive and can be reduced through a hardware redesign. The major cause of power loss is due to load position noise that propagates through the control algorithm. The load position is used by the outer load position control loop to define the desired motor position. The control algorithm gains up load position by a factor of 230 due to the spring compensation term and gains up the even noisier load velocity term by 6.25 due to the load position loop's differential term. Any noise on the load position signal causes unnecessary and substantial motor movement through these two terms. The load signal noise comes from two main sources, the inherent noise of the magnetic load position encoder and encoder misalignment due to inadequate mounting support and vibration of the load. A hardware redesign including an improved load mounting system would decrease encoder misalignment while a higher resolution encoder would decrease sensor noise. Both are reasonable additions for the scale of the hardware. The input power required to hold the load plate stationary was measured at an average of $150mWatts$. This power represents the excess system power due to noise. Table 5.3 gives the estimated system efficiencies that would result if there was no power wasted due to noise. These estimates show that the system has the potential for significant increases in efficiency. The peak efficiencies match or exceed the rigid system open loop efficiencies implying that a series elastic system run at resonance has the potential to be more efficient than its rigid counterpart.

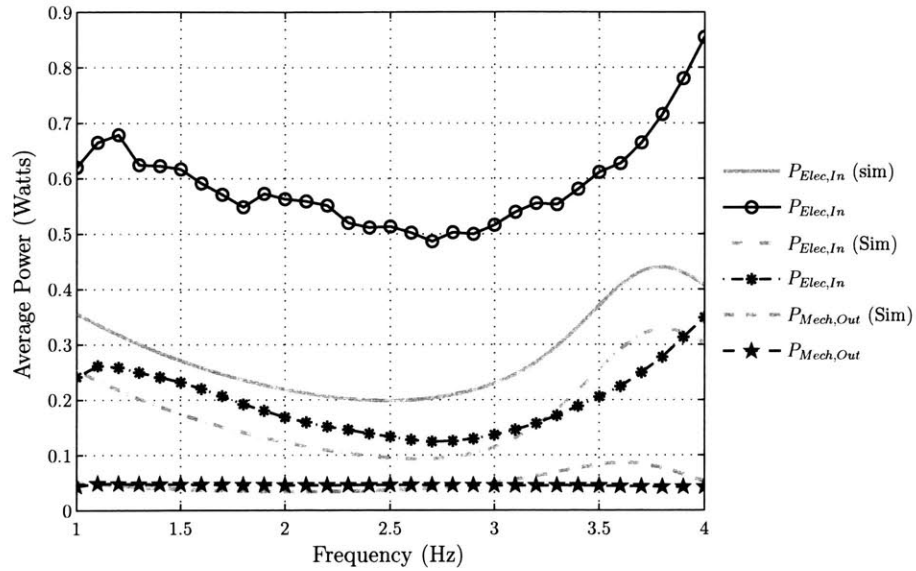


(a) Controlled Power Response

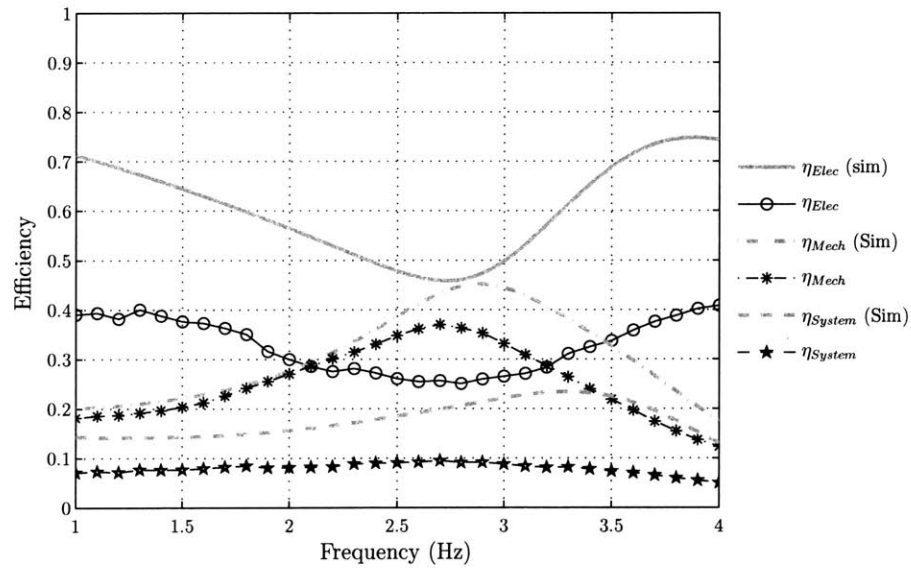


(b) Controlled Efficiency Response

Figure 5-14: Controlled Efficiency Response under low loading. These plots represent the load friction case where $\tau_{f,E} = 46mNm$. The system exhibits a peak in efficiency at $2.8Hz$ and has the largest gain in efficiency of the three loading values used.

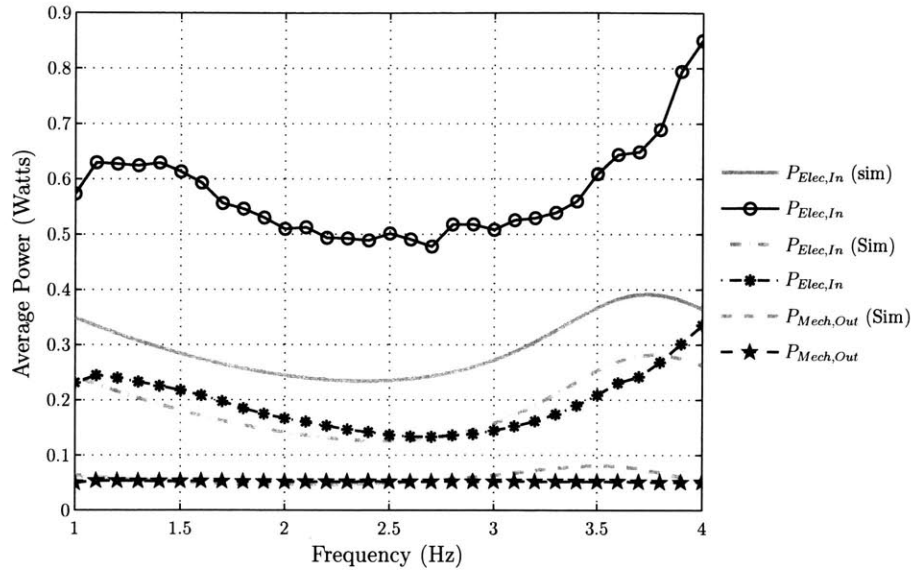


(a) Controlled Power Response

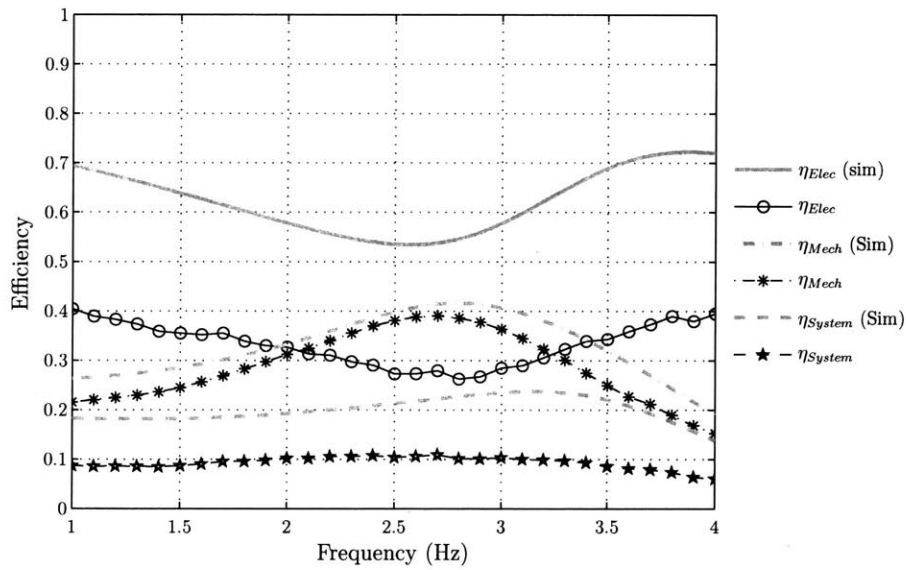


(b) Controlled Efficiency Response

Figure 5-15: Controlled Efficiency Response under medium loading. These plots represent the load friction case where $\tau_{f,E} = 85mNm$. Like the low loading case the system exhibits a peak in efficiency at $2.8Hz$, however, it does not have as high efficiency gains at resonance as the low loading case. It also exhibits higher efficiency away from resonance than the low loading case.



(a) Controlled Power Response



(b) Controlled Efficiency Response

Figure 5-16: Controlled Efficiency Response under high loading. These plots represent the load friction case where $\tau_{f,E} = 125mNm$. Like the other two cases the system exhibits a peak in efficiency at $2.8Hz$, however, the peak is small when compared to the other two cases. The high damping case exhibits the highest efficiency both at and away from resonance.

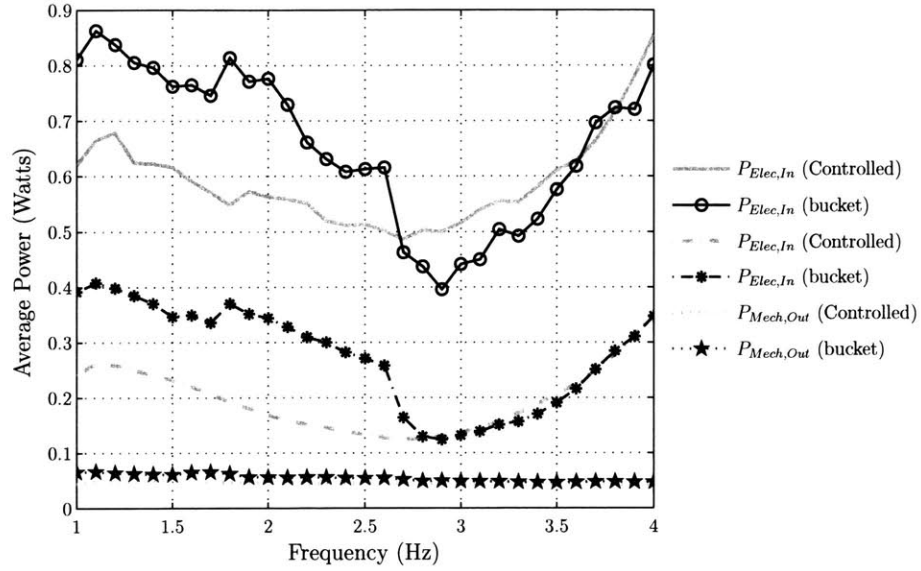
	$\tau_{f,E} = 46mNm$	$\tau_{f,E} = 85mNm$	$\tau_{f,E} = 125mNm$
1Hz Efficiency	3%	8.7%	10.8%
2.8Hz Efficiency	8.2%	13.7%	15.9%
Efficiency Gain	2.73	1.57	1.47

Table 5.3: Estimated controlled efficiency values after the power lost due to noise has been taken out.

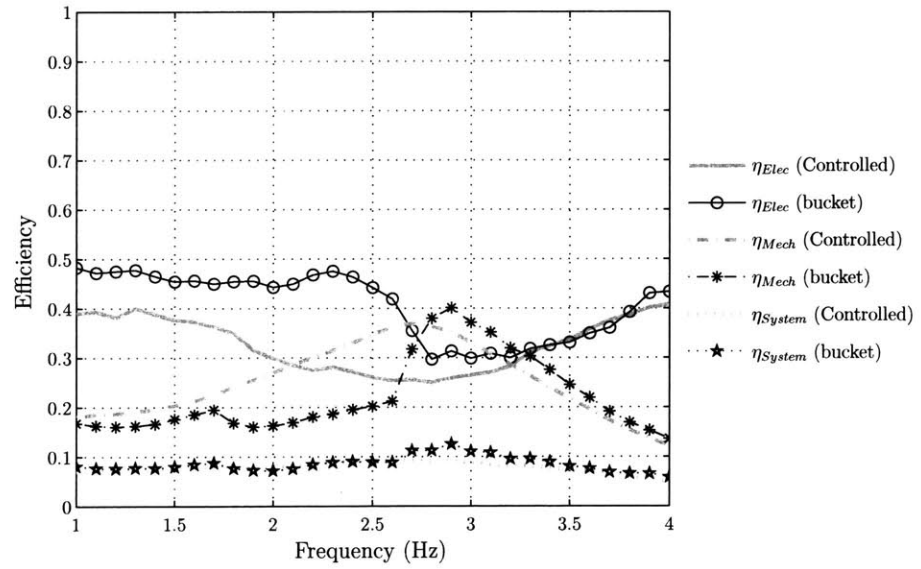
5.3 Non-Linear Loading

As a final test of the system's ability to conserve power due to resonance, the nonlinear inertial load was added to the friction load as described in Section 3.5.2. Adding a nonlinear load causes the resonant frequency of the system to change with load variations. In theory, however, the system should still have an optimal frequency which it can be operated at to achieve the maximum efficiency. The test results using the nonlinear inertial load are given in Figures 5-17, 5-18 and 5-19 for $\tau_{f,E} = 46mNm$, $\tau_{f,E} = 85mNm$ and $\tau_{f,E} = 125mNm$ respectively. The responses show that there is still an efficiency peak indicating that the actuators can be exploited for efficiency in real world applications.

The efficiency peak of the actuators under nonlinear inertial loading is at a higher frequency than when under just the friction load. This is reasonable as it was expected that the addition of a changing inertia to the load would alter the coupling between the load and the spring. It does, however, make control slightly more complicated because it becomes much harder to rely on models to predict the efficient frequency. In order to have robots that can operate at their efficient frequency, either experiments to determine that frequency for each gait will have to be performed or an improved control strategy that naturally finds the optimal frequency will be required.

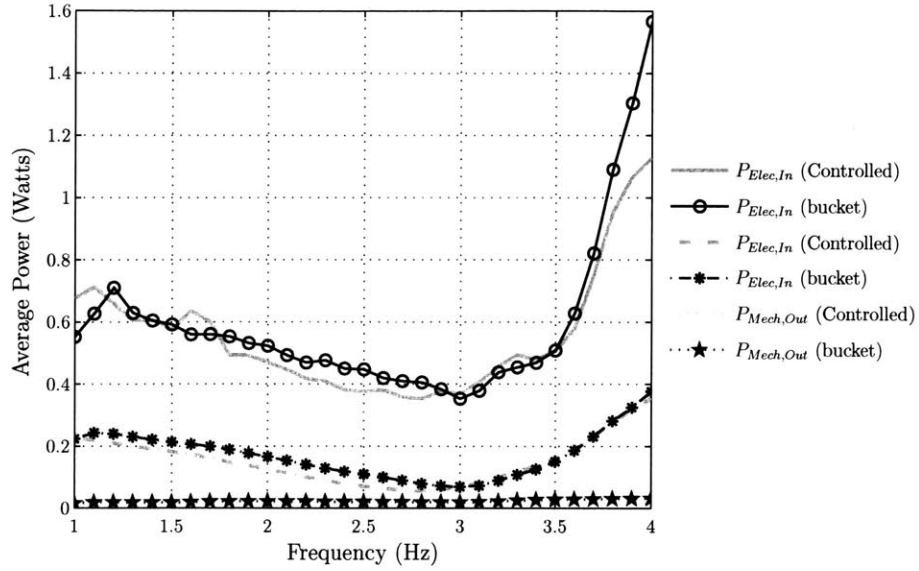


(a) Controlled Power Response

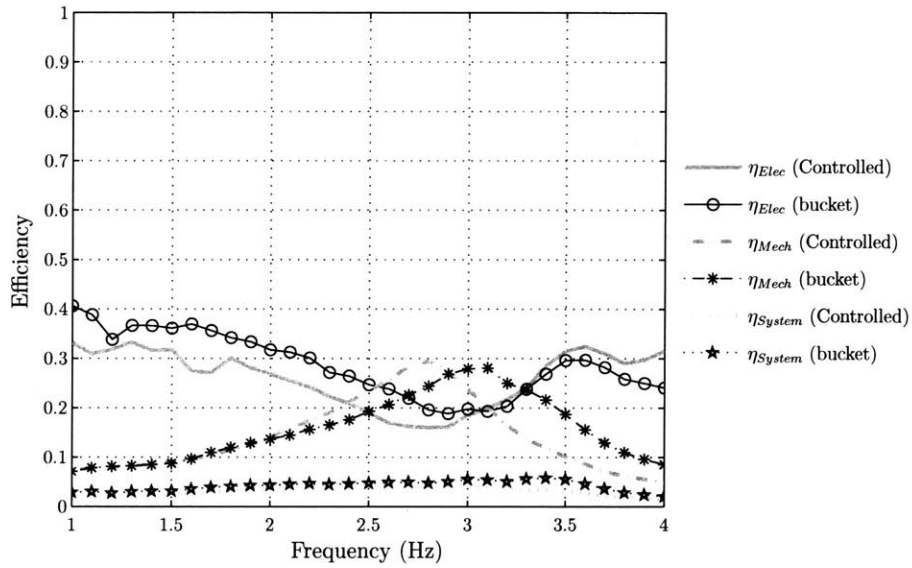


(b) Controlled Efficiency Response

Figure 5-18: Controlled Efficiency Response under Nonlinear Loading with $\tau_{f,E} = 85mNm$. The plot in this case is not as smooth as the linear damping case, an effect of the sudden ground contacts. It does still show that an efficiency peak is achieved at a particular frequency

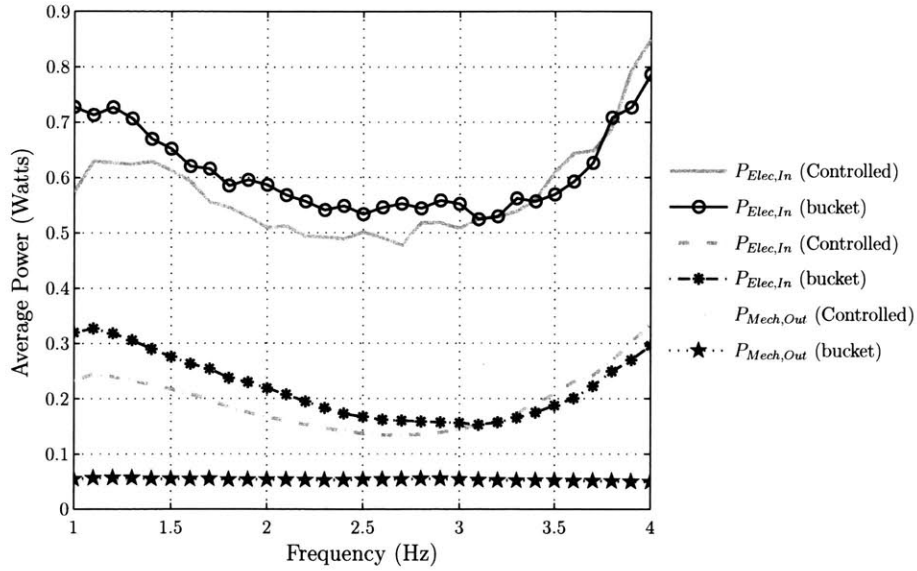


(a) Controlled Power Response

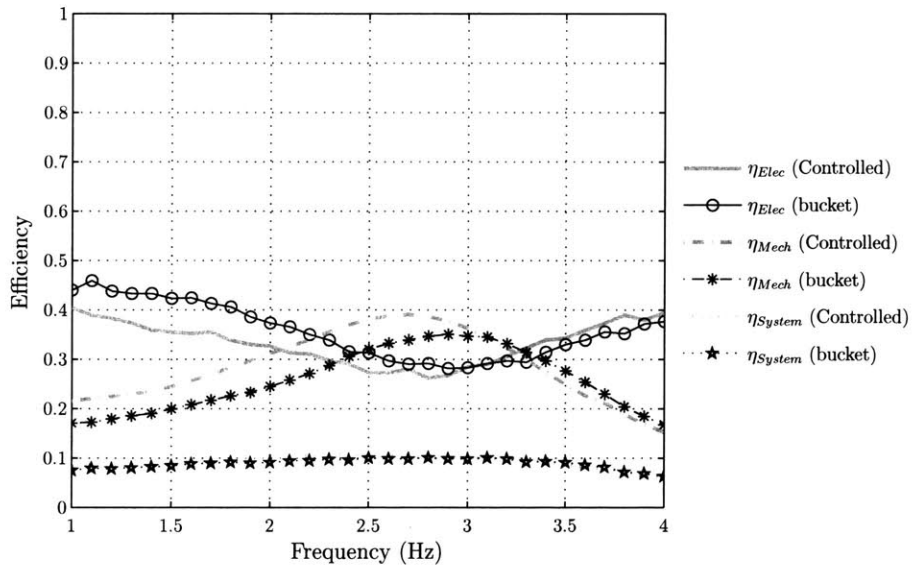


(b) Controlled Efficiency Response

Figure 5-17: Controlled Efficiency Response under Nonlinear Loading with $\tau_{f,E} = 46mNm$. The efficiency peak has shifted higher in frequency due to the nonlinear inertial load. The amount of efficiency obtained, however, is comparable to the controlled system without the nonlinear inertial load; a promising result for application to real world systems.



(a) Controlled Power Response



(b) Controlled Efficiency Response

Figure 5-19: Controlled Efficiency Response under Nonlinear Loading with $\tau_{f,E} = 125mNm$. Just as with low and medium friction loadings, the efficiency peak has shifted higher in frequency. Again the amount of efficiency gained is comparable to the controlled system without the nonlinear inertial load. The system also continues to follow the same trends as the ideal model in that the heavier loading condition yields the greatest overall system efficiency while achieving the smallest gains.

Chapter 6

Conclusions

Series elastic actuators have become well known for their abilities to provide shock tolerance and accurate force control, however, they also have the ability to gain efficiency through the exploitation of their natural modes. Just as animals use the elasticity in their muscles and tendons to operate efficiently, robots can exploit series elastic actuators for efficiency. This thesis explores the potential for efficiency gain provided by series elastic actuators and has shown through model and experiment the conditions under which efficiency can be gained as well as the mechanisms through which power is lost.

Efficiency

The efficiency of the system was documented and it was shown that series elastic actuators have the potential to achieve large efficiency gains up to a factor of 2 under the appropriate conditions. The amount of efficiency that could be gained depended directly on the load damping of the actuator. Under low load damping, the system exhibited large efficiency peaks at an optimal frequency. Even when more heavily damped, the system still showed an improvement in efficiency at an optimal frequency, however, the gains over lower frequencies were much smaller than in the lightly damped case. Of note was that the efficiency of the system at all frequencies was higher when the system was more heavily damped indicating that it is beneficial to operate the system under larger loadings in which the system resonance is suppressed. There are, however, some tasks that are lightly damped, such as human walking gaits where the direction of movement is parallel with the environmental interface. In these tasks it is certainly beneficial to operate series elastic actuators at their resonant frequency.

Models of the system under different operating conditions were used to understand the mechanisms in which power was lost. Initially a linear model of the open loop system showed that system efficiencies could peak as high as 46% when lightly damped and up to 54% under heavier damping.

When this model was compared to the open loop results of the hardware, it was found that stiction caused drastic decreases in efficiency limiting lightly damped efficiencies to 12% and more heavily damped efficiencies to 21.7%. Models of the stiction losses were added to the linear model and verified that the presence of stiction cause both a mechanical loss due to the contact forces and an electrical loss due to the extra current necessary to overcome stiction. The new model including stiction was then compared with the efficiency results of the controlled system and it was found that the addition of control created another large decrease in system efficiency. In the controlled system, lightly damped efficiencies were limited to 4.7% while the more heavily damped system was limited to 11% efficiency. Finally a nonlinear load was used to show that an efficiency peak was still obtained under realistic loading conditions verifying that controlling series elastic actuators to resonance can be beneficial in real world applications.

Although some power loss due to control is essential, the amount sustained in the present system is excessive. The results from the current system indicate that if series elastic actuators are part of the system, it is beneficial to run them at their resonant frequency in order to maximize efficiency. Unfortunately, the excessive power loss experienced in the current system due to control makes a rigid system the better choice if the shock protection and force control properties of series elastic actuators are not needed. Through redesign and improvements in control, however, it is feasible, as is shown by the open loop response, that a series elastic system run at its resonant frequency can be more efficient than its rigid counterpart.

6.1 Suggestions for Improvement

This thesis has shown that under relatively lightly damped loading conditions efficiency is gained by running series elastic actuators at their natural frequency. It also shed light on the major sources of power loss that limited the performance of the actuators. It was found that the power loss came mostly from drawbacks in hardware design and it was suggested that improvements in the hardware could yield vast improvements in system efficiency. The two major areas of improvement suitable for the current hardware are in sensing and mounting.

6.1.1 Sensors

The sensors used in this thesis were AM256 Rotary Magnetic Encoders made by Rotary and Linear Systems. The sensors are prone to noise as is described in Section 3.1.4. The noise exhibited by the encoders comes in three forms. Inherent electronic noise, axial misalignment noise (integral noise) and noise produced by temporary misalignments due to radial vibrations of the spring shaft (mounting noise).

The sensor noise causes large decreases in system efficiency when high controller gains cause

the motor to chatter in response to the noise. Improvements in sensing could potentially decrease the motor chatter, allowing the control system to operate much more efficiently. Replacing the magnetic encoder with a high line count quadrature encoder would increase the resolution of the position sensing and decrease the amount of noise that propagates through the control system. Also, integral noise is a characteristic of the magnetic encoder and is not present in a quadrature encoder.

6.1.2 Mounting and Support

Shortcomings in the mounting of the hardware affected the efficiency of the system in two ways. First, as explained in the last section, mounting noise propagated through the control system and caused motor chatter which resulted in a great deal of power loss. Second, there was a large amount of stiction in the system which in turn caused a large power loss during both open loop and closed loop operation. The load plate is currently supported by just the spring shaft, with the only connection point being the 4mm hex on the end of the shaft. Due to the size and weight of the load plate this puts a large amount of torque on the spring shaft. The spring shaft is supported by two bearings, one just before the connection to the load plate (the load bearing) and one at the other end of the spring shaft placed inside the harmonic drive's input pulley (the input bearing). The input pulley is in turn supported by a bearing between it and the harmonic drive's housing (the pulley bearing). Therefore, the end of the spring shaft away from the load plate connection is supported by a bearing inside another bearing. Having the two bearings for one support creates a "loose" support condition under which radial movement is allowed. Although there is a coupling between the spring shaft and the auxiliary encoder shaft, radial movement on the spring shaft still manages to propagate through the coupling and cause radial movements of the encoder shaft which results in mounting noise.

Mounting noise could be greatly reduced through a couple improvements to the benchtop test-stand. Replacing the shaft coupling with one that is more tolerant to radial movements would decouple radial spring shaft deflections from the load encoder and reduce the mounting noise. This would be essential if the load encoder were changed to a quadrature encoder because misalignments can cause quadrature encoders to miss counts. Although replacing the shaft coupling will improve the sensing it will not solve the problem of load plate movement due to poor mounting, which in itself a source of power loss. Moving the input bearing outside of the input pulley so that it is placed between the spring shaft and the harmonic drive housing will improve the "loose" support condition created by the current combination of the input bearing and the pulley bearing. This will reduce spring shaft radial movement and in turn reduce unwanted load plate movement.

Stiction is the largest source of power loss in the system. Large amounts of stiction are naturally inherent to harmonic drives therefore without a complete redesign, where the harmonic drive is replaced, it may be difficult to reduce the stiction a great deal. Improving the mounting of the system will take stresses off of the harmonic drive which will reduce the level of stiction found in

the current setup. Replacing the bearings in the system with high load ceramic bearings will also reduce the amount of stiction.

6.2 Future Work

There are many areas of study in which the results of this thesis can serve as a starting point. The areas most pertinent to the efficient application of series elastic actuators are suggested here.

6.2.1 Comparison to a Rigid Actuator

In this thesis, the efficiency of a series elastic actuator when run at different frequencies was investigated and it was found that there is an optimal frequency at which the system should be operated to achieve the most efficient performance. It is also suggested that series elastic actuators, with improvements from this work, could have the potential to be more efficient than rigid actuators. Unfortunately, in this thesis the only comparisons that could be made to rigid actuators were in models because the hardware was much too fragile to accommodate a solid shaft. To investigate the claim that series elastic actuators have the potential to outperform rigid actuators an experimental comparison is required. This would lead to better information on the breakdown of power loss in the system and lead to a better understanding of where power can best be saved.

6.2.2 Control

Linear control algorithms were used for the control in this thesis. These control schemes adjust the command signal based on disturbances portrayed in the error signal. It was found that in the current scheme this equated to fairly large adjustments to the desired motor position signal within a cycle of output position. This has been referred to as motor chatter throughout this thesis and has been identified as a large source of power loss in the system. Investigation of alternative forms of control that adjust more fluidly to disturbances and are geared toward steady state operation, such as the methods presented in [Williamson, 1999] and [Buchli et al., 2005], could lead to much more efficient actuation. The ultimate goal would be a control scheme that can achieve efficiencies close to the open loop system.

6.2.3 Exploration of the Multi-Link Case

The work done in this thesis was limited to a single link benchtop teststand. As a final test of the system a nonlinear load was used and the system still demonstrated an optimal frequency where efficiency was maximize. As a result, it is reasonable to believe that extension of the work in this thesis to the multi-link case will also yield efficient operation. As mentioned in Section 3.5, the

multi-link case is a much more complicated nonlinear system than the linear case. Further study on the multi-link case has the potential to yield advances in system modeling, control and efficient actuation. If the ideas in this thesis are to be applied in real world applications, research on multi-link manipulators will be essential.

6.2.4 Application to a Robotic Vehicle

Of course, the ultimate goal of the research in this thesis and all of the future work mentioned is the application of efficient actuation on a real robotic vehicle. There are many vehicles that currently run off of series elastic actuators for their shock protection and force control properties, however, there has been very little done to exploit the efficiency gains created by their resonant modes. Draper Laboratory's HISS vehicle ran a locomotory sidewinding gait with springs in the system and it showed some results that could be linked to efficient actuation. Unfortunately, these results were subject to sensing errors and cannot be considered completely reliable. Although a snake robot is a natural choice as an extension of this work due to its undulatory movements, any biomimetic robot will have gaits that will allow series elastic actuators to be exploited for efficiency. Other good candidates include swimming robots such as fish, flying robots that use a flapping gait or biped/quadruped robots during their walking or running gaits.

Bibliography

- R. M. Alexander. Elastic energy stores in running vertebrates. *American Zoologist*, 24(1):85–94, 1984.
- Chae H. An and John M. Hollerbach. Dynamic stability issues in force control of manipulators. pages 890 – 896, 1987.
- BDI. Boston dynamics. <http://www.bostondynamics.com/index.php>.
- R. Blickhan. The spring-mass model for running and hopping. *Journal of Biomechanics*, 22(11/12): 1217 – 27, 1989. ISSN 0021-9290.
- R. Blickhan and R. J. Full. Similarity in multilegged locomotion: Bouncing like a momopode. *Journal of Comparative Physiology A: Neuroethology, Sensory, Neural, and Behavioral Physiology*, 173 (5): 509–517, 1993.
- Forbes T. Brown. *Engineering System Dynamics*. Marcel Dekker, Inc., 2001.
- Jonas Buchli, Ludovic Righetti, and Auke Jan Ijspeert. A dynamical systems approach to learning: A frequency-adaptive hopper robot. *Lecture Notes in Computer Science (including subseries Lecture Notes in Artificial Intelligence and Lecture Notes in Bioinformatics)*, 3630 NAI:210 – 220, 2005. ISSN 0302-9743.
- C. Canudas De Wit and P. Lischinsky. Adaptive friction compensation with partially known dynamic friction model. *International Journal of Adaptive Control and Signal Processing*, 11(1):65 – 80, 1997. ISSN 0890-6327.
- C. Canudas de Wit, H. Olsson, K.J. Astrom, and P. Lischinsky. A new model for control of systems with friction. *IEEE Transactions on Automatic Control*, 40(3):419 – 25, 1995. ISSN 0018-9286.
- G. A. Cavagna, N. C. Heglund, and C. R. Taylor. Mechanical work in terrestrial locomotion: two basic mechanisms for minimizing energy expenditure. *Am J Physiol Regul Integr Comp Physiol*, 233(5):243-261, 1977. ISSN 0278-3649.

- GA Cavagna, H Thys, and A Zamboni. The sources of external work in level walking and running. *J Physiol (Lond)*, 262(3):639–657, 1976.
- S. Chiaverini and L. Sciavicco. The parallel approach to force/position control of robotic manipulators. *IEEE Transactions on Robotics and Automation*, 9(4):361 – 73, 1993. ISSN 1042-296X.
- S.D. Eppinger and W.P. Seering. Three dynamic problems in robot force control. *IEEE Transactions on Robotics and Automation*, 8(6):751 – 8, 1992. ISSN 1042-296X.
- K. Hirai, M. Hirose, Y. Haikawa, and T. Takenaka. The development of honda humanoid robot. *Proceedings. 1998 IEEE International Conference on Robotics and Automation (Cat. No.98CH36146)*, vol.2:1321 – 6, 1998.
- N. Hogan. Impedance control: an approach to manipulation. i. theory. *Transactions of the ASME. Journal of Dynamic Systems, Measurement and Control*, 107(1):1 – 7, 1985a. ISSN 0022-0434.
- N. Hogan. Impedance control: an approach to manipulation. ii. implementation. *Transactions of the ASME. Journal of Dynamic Systems, Measurement and Control*, 107(1):8 – 16, 1985b. ISSN 0022-0434.
- N. Hogan. Impedance control: an approach to manipulation. iii. applications. *Transactions of the ASME. Journal of Dynamic Systems, Measurement and Control*, 107(1):17 – 24, 1985c. ISSN 0022-0434.
- Kevin W. Hollander, Robert Ilg, Thomas G. Sugar, and Donald Herring. An efficient robotic tendon for gait assistance. *Journal of Biomechanical Engineering*, 128(5):788 – 791, 2006. ISSN 0148-0731.
- H. Kazerooni, P.K. Houpt, and T.B. Sheridan. Robust compliant motion for manipulators. ii. design method. *IEEE Journal of Robotics and Automation*, RA-2(2):93 – 105, 1986. ISSN 0882-4967.
- Benjamin T. Krupp and Jerry E. Pratt. A power autonomous monopodal robot. *Proceedings of SPIE - The International Society for Optical Engineering*, 6201:620112 –, 2006. ISSN 0277-786X.
- LegLab. Mit leg laboratory. <http://www.ai.mit.edu/projects/leglab/>.
- M.T. Mason. Compliance and force control for computer controlled manipulators. *IEEE Transactions on Systems, Man and Cybernetics*, SMC-11(6):418 – 32, 1981. ISSN 0018-9472.
- T.A. McMahon and G.C. Cheng. The mechanics of running: how does stiffness couple with speed? *Journal of Biomechanics*, 23(1):65 – 78, 1990. ISSN 0021-9290.
- D. Paluska and H. Herr. Series elasticity and actuator power output. *Proceedings. 2006 Conference International Robotics and Automation (IEEE Cat. No. 06CH37729D)*, pages 1830 – 3, 2006.

- G.A. Pratt and M.M. Williamson. Series elastic actuators. *Proceedings. 1995 IEEE/RSJ International Conference on Intelligent Robots and Systems. Human Robot Interaction and Cooperative Robots (Cat. No.95CB35836)*, vol.1:399 – 406, 1995.
- Gill A. Pratt. Legged robots at mit: What’s new since raibert. *IEEE Robotics and Automation Magazine*, 7(3):15 – 19, 2000. ISSN 1070-9932.
- M.H. Raibert and J.J. Craig. Hybrid position/force control of manipulators. *Transactions of the ASME. Journal of Dynamic Systems, Measurement and Control*, 103(2):126 – 33, 1981. ISSN 0022-0434.
- RLS. Rotary and linear motion sensors. <http://www.rls.si/default.asp?prod=am256>.
- R.K. Roberts, R.P. Pail, and B.M. Hillberry. The effect of wrist force sensor stiffness on the control of robot manipulators. *1985 IEEE International Conference on Robotics and Automation (Cat. No. 85CH2152-7)*, pages 269 – 74, 1984.
- David W. Robinson. *Design and Analysis of Series Elasticity in Closed-Loop Actuator Force Control*. PhD thesis, Massachusetts Institute of Technology, 2000.
- Rotary and Linear Motion Sensors (RLS). Am256 angular magnetic encoder datasheet. Technical report.
- J.K. Salisbury. Active stiffness control of a manipulator in cartesian coordinates. *Proceedings of the 19th IEEE Conference on Decision & Control Including the Symposium on Adaptive Processes*, pages 95 – 100, 1980.
- U. Scarfogliero, C. Stefanini, and P. Dario. A bioinspired concept for high efficiency locomotion in micro robots: the jumping robot grillo. *Proceedings. 2006 Conference on International Robotics and Automation (IEEE Cat. No. 06CH37729D)*, pages 4037 – 42, 2006.
- D.L. Trumper, S.J. Ludwick, and M.F. Byl. A loop shaping perspective for tuning controllers with adaptive feedforward cancellation. *Precision Engineering*, 29(1):27 – 40, 2005. ISSN 0141-6359.
- Bram Vanderborght, Bjorn Verrelst, Ronald Van Ham, Michael Van Damme, Dirk Lefeber, Bruno Meira Y Duran, and Pieter Beyl. Exploiting natural dynamics to reduce energy consumption by controlling the compliance of soft actuators. *International Journal of Robotics Research*, 25(4): 343 – 358, 2006.
- J.F. Veneman, R. Ekkelenkamp, R. Kruidhof, F.C.T. Van Der Helm, and H. Van Der Kooij. A series elastic- and bowden-cable-based actuation system for use as torque actuator in exoskeleton-type robots. *International Journal of Robotics Research*, 25(3):261 – 281, 2006. ISSN 0278-3649.
- M. M. Williamson. *Robot Arm Control Exploiting Natural Dynamics*. PhD thesis, MIT, 1999.